POLITECNICO DI TORINO

DEPARTMENT OF MECHANICAL AND AEROSPACE ENGINEERING
Master degree in mechanical engineering

Master degree Thesis

High-fidelity modeling of degraded rod-end for flight control actuators - analysis and preliminary PHM study

Tutor:
Prof. Massimo SORLI
Dott. Andrea DE MARTIN

Candidate:
Alberto BACCI

ACADEMIC YEAR 2019-2020

Abstract

In flight control system, rod-ends are used to connect the actuator piston rod to the flight control surface. Rod-ends are spherical joints substantially constituted by a sphere moving inside a housing. Different construction characteristics have been developed in order to ensure lubrication between elements.

Rod-ends represent critical elements for flight control system due to three failure modes: excessive wear between components in relative motion, lubricant degradation, and crack propagation on the eye-shaped part of the rod-end body. Therefore, the goal of this thesis is the realization of a high-fidelity mathematical model of the component, which is able to describe the physical behaviour of the rod-end in order to provide a valid tool for a future CBD/PHM feasibility study.

The system will be modelled as a journal bearing and divided in three part linked to three different work conditions. The first one, called "hydrodynamic lubrication model", which occurs when the journal and the bearing are completely separated by a lubricant meatus. This model is based on the Reynolds equation. The second one, called "contact model", uses the Lankarani and Nikravesh equation to describe the system when certain contact between elements is detected. The third one, called "mixed or partial lubrication model", uses the previous models to describe the system when a lubricant meatus is still present, but its thickness is not enough to avoid some journal and bearing asperity contact. A fundamental parameter called "Tallian lambda" has been used to discriminate one work condition from the others.

The rod-end model will be implemented into an Electro-Hydraulic Servo-Actuator (EHSA) model to ensure numerical stability and correct functioning. The effects of two failure modes have been investigated: that due to an anomalous wear on the accuracy position of the controlled surface, and the other one due to the lubricant degradation on the undesired forces exchanged between the internal elements of the rod-end.

Contents

List of Figures

List of Tables

Chapter 1

Introduction

The word prognostics is originally a Greek word "*progignôskein*" that means to know in advance. In engineering, prognostics can be defined as the process of RULs (*Remining useful life*) estimation of system/subsystem/component that is degrading due to either normal operation (no fault symptoms) or detected fault [31].

Therefore, the engineering discipline called prognostics can be divided in two subsequent steps [32]:

- diagnosis: it represents the methodologies to detect fault or anomaly conditions, pinpoint or isolate which component in a system is faulty and decide on the potential impact of a failing or failed component on the health of the system. These methodologies are grouped under the name of "*Fault Detection and Identification* (FDI)";

- prognosis: it represents the prediction of the future system behaviour, in order to answer the question, "What is the *remaining useful lifetime* (RUL) of a machine or a component once an impending failure condition is detected, isolated, and identified?".

The benefit from prognostics can be flourished if its information is used as the main source to system health management. PHM (*Prognostics and Health Management*) is the emerging engineering discipline that links studies of failure mechanisms to system life cycle management [33].

As long as prognostics deals with the future knowledge of system condition and health, PHM finds application in *Condition-Based Maintenance* (CBM). This predictive

maintenance can replace the old and expensive scheduled or, even worse, after failure maintenance.

The PHM/CBD system introduces the following main benefits:

- achieve high reliability without adding many redundant devices [31];

- total life cycle cost management optimization, i.e. ROI maximization in order to achieve optimum cost-effectiveness versus performance decisions [34];

- minimization of machines downtime and better productivity [35];

- moving from fail and fix strategy to predict and prevent [36].

Since prognostics ensures an increase in safety, many applications are directed towards safety critical parts of vehicles especially in aerospace [31]. Flight control systems and their associated flight control servo-actuators are one of the critical aircraft systems and belong to the top operational disruption contributors. However, this is an engineering area where PHM has found very limited interest so far, especially for Electro-Hydraulic Servo-Actuators (EHSA) [30].

S. Autin, J. Socheleau, A. Dellacasa, A. De Martin, G. Jacazio, and G. Vachtsevanos presented, in their work [30], the results of how an innovative fault diagnosis and failure prognosis framework for EHSAs can successfully be developed. The specific benefits of an efficient health monitoring system for aircraft flight control system are:

- improvement of passenger's safety by avoiding the scenario where the aircraft is no longer controllable;

- improvement of aircraft reliability and dispatch ability by avoiding, for example, on ground immobilization and cancellations;

- reduction of maintenance costs.

An extensive analysis was carried out by the authors to identify the critical, frequent and testable faliure modes and relative components [30]:

- crack of the servo-valve internal feedback spring and hence a reduction of its stiffness;

- demagnetization of servo-valve torque motor and hence a reduction of the torque motor gain;

- distorted jet pipe of the servo-valve and hence a non-symmetrical direction of the flow when the servo-valve current is equal to zero;

- backlash in the actuator rod-end, thus vibration of the controlled surface and accuracy error.

This work focuses the attention on the last component, the Rod-end.

Rod-ends are connection elements composed of a spherical ball which is designed to rotate inside a housing. This spherical ball represents the bearing, while the housing, on which the sphere rotates, is the race. In order to connect the rod-end to another component or system, each side of the sphere is machined to obtain two parallel flat surfaces. Then, the modified sphere is bored through the centre.
Rod-ends can be divided in two main categories [37]:

- two-piece rod-ends: in this configuration the body is formed around the sphere, thus the race is actually part of the body;

- three-piece rod-ends: here the housing is formed around the sphere. Next the housing is forced into the body. This three-piece design ensures better quality and precision and it is referred to as "aircraft" rod-end.

The rod-end body allows the connection with the rod, usually through a threaded coupling. In Figure 1.1 a three-piece rod-end is displayed.

Figure 1.1: Three-piece rod-end [37].

10

The lubrication between the sphere and the housing can also be provided in two different ways:

- grease: where this material provides a lubrication meatus. The main problem of this solution is the leakage of grease through the rod-end sides;

- fabric liner: in this case the inner housing surface has a woven fabric liner bonded to it. The woven fabric liner is mainly made up of matrix of reinforced fibers. A first fiber component (like Nomex) ensures strength and good bonding properties, while a second component (like PTFE) is mainly used to improve friction and wear properties of materials [38]. This solution allows the rod-end to be self-lubricated.

For flight control system, rod-ends are used to connect one side of the actuator to the underlying airframe structure and the other one to the controlled surface, as shown in Figure 1.2.
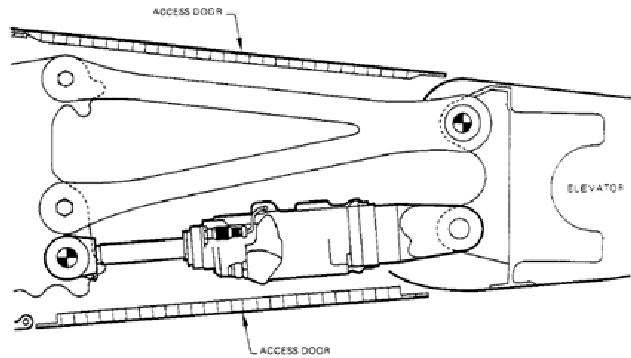
Figure 1.2:   Actuator installation configuration for an A300 elevator [39].

Three failure modes have been identified for rod-ends:

- crack in the eye-shaped part of the body: if for any reason a crack is generated on this weak part, the stresses developed as the actuator operates may cause a growth of the crack till complete rupture of the rod-end body, as shown in Figure 1.3 (up);

- lubricant degradation: it has been assessed that oil or base oil oxidation constitutes the main time dependent failure mode for lubricants [40]. Thus, the lubricant degradation reduces its load capacity allowing an easier metal to metal contact.

11

When the rod-end sphere is in contact with the housing an increase of friction force occurs. This may cause a plastic deformation of the actuator piston rod (as shown in Figure 1.3) since the friction force could generate a normal force and a torque at the end of the rod;

- sphere or housing wear: rod-end spherical bearings are sized such to be subjected to a small backlash increase over the actuator service life. However, failures have occurred in which an anomalous wear of the spherical bearing caused a large backlash increase leading to high airframe vibrations in flight [30].
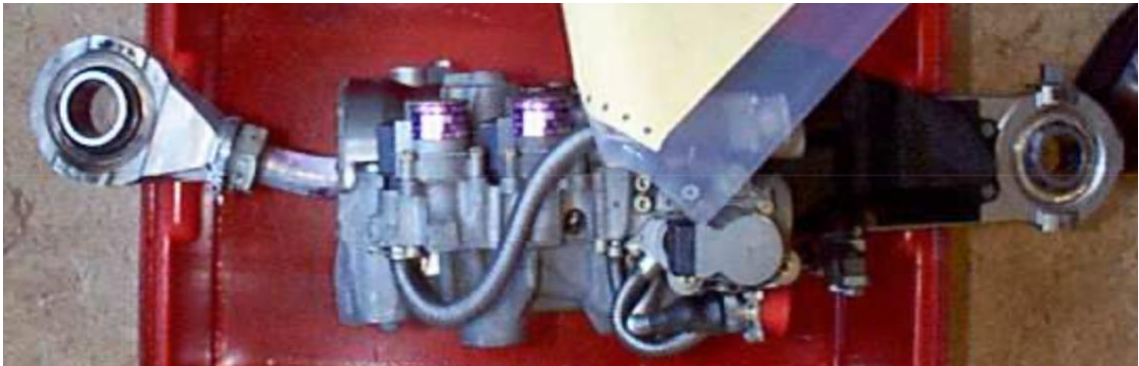
Figure 1.3: Rod-end failure effects [41].

As it is possible to imagine, the occurrence of one of these failures compromises the correct functioning of flight control servo-actuators and their associated flight control surfaces and could lead to catastrophic events.

Therefore, the goal of this thesis is the realization of a high fidelity physical-based model of a rod-end which is able to simulate and confirm the failure modes, that the experimental evidence has shown, in order to be used as a valid tool for **CBD/PHM** future applications. Considering the rod-end construction characteristics and the failure modes previously exposed, it has been decided to model the system as a dynamically loaded journal bearing. A journal bearing consists of a cylindrical shaft rotating into a bush and the space between them contains lubricant. Therefore, the rod-end model is based on two main simplifying assumptions:

- the spherical configuration of the rod-end is reduced to a cylindrical configuration, thus, no misalignment between the shaft and the bush axis is considered;

- no lubricant leakage, thus the proper amount of lubricant is always available.

The rod-end model takes under consideration three different work conditions as function of the shaft-bush relative position. As the clearance is reduced, the system shifts from a hydrodynamic lubrication to a contact model passing through a mixed model which is obtained, as the name may suggest, as a mix of the previous two.
The numerical stability of the model will be tested after its implementation into an **EHSA** complete model of a commercial aircraft in revenue service whose characteristics and performance are well known and documented.
Both rod-end and EHSA complete models have been realized into **MATLAB/Simulink** environment.

Chapter 2

Hydrodynamic lubrication model

During the 19th century Beauchamp Tower, an English engineer, noticed that the lubricant oil in a journal bearing always leaked out of a hole when the load was applied. The hole was originally placed to allow oil to be supplied into the bearing to provide 'lubrication'. Since the leakage of oil was unwanted, first the hole was plugged with a cork and then with a wooden bung, but still some leakage was detected and the bung was slowly pushed out of the hole by the oil. By the observation of this phenomenon Tower realized that the oil was pressurized by some as yet unknown mechanism. Tower then measured the oil pressure and found that it could separate the sliding surfaces by a hydraulic force [1].

Tower's detailed data were available to provide experimental confirmation of hydrodynamic lubrication almost at the exact time when Reynolds needed it. The result of this was a theory of hydrodynamic lubrication published in the Proceedings of the Royal Society by Reynolds in 1886 [2].
Reynolds provided the first analytical proof that a viscous liquid can physically separate two sliding surfaces by hydrodynamic pressure resulting in low friction and theoretically zero wear.
There are two conditions for the occurrence of hydrodynamic lubrication [3]:

- two surfaces must move relatively to each other with sufficient velocity for a load-carrying lubricating film to be generated;

- surfaces must be inclined at some angle to each other, i.e. if the surfaces are parallel a pressure field will not form in the lubricating film to support the required load.

Taking under consideration the configuration where a flat horizontal surface (AB) is moving with a tangential speed with respect to a second inclined surface (CD), we can see in Figure 2.1 that the distance QP represents the motion of any point P, and the slope of the lines will represent the tangential forces in the fluid.

The shape of these curves can be determined using the continuity equation. The quantity carried across any section PQ would be:

$$PQ \cdot \frac{U}{2} \tag{2.1}$$

and, consequently, would be proportional to **PQ**. The quantities carried across all sections must be the same, as the surfaces do not change their relative distances; therefore, there must be a general outflow from any vertical sections PQ equal to:

$$\frac{U}{2} \cdot (PQ - P_1 Q_1) \tag{2.2}$$

This outflow will take place to the right and left of the section of greatest pressure (P_1Q_1).
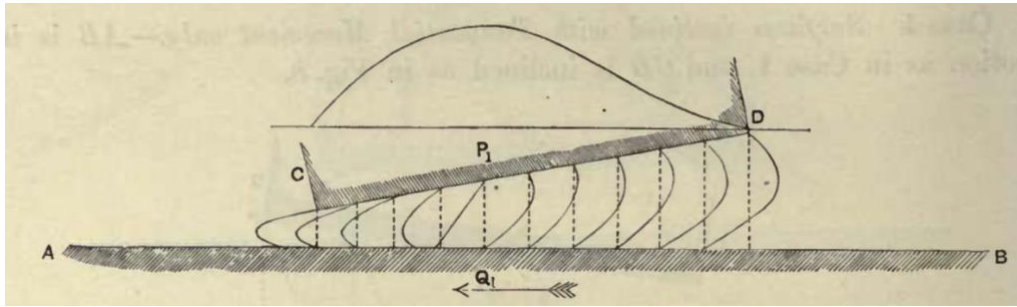
Figure 2.1: Pressure distribution between inclined flat surfaces with tangential movement only [2].

When the moving surface (AB) is cylindrical and revolving about its axis (Figure 2.2) the curves of motion can be found by the same method as in the previous case.
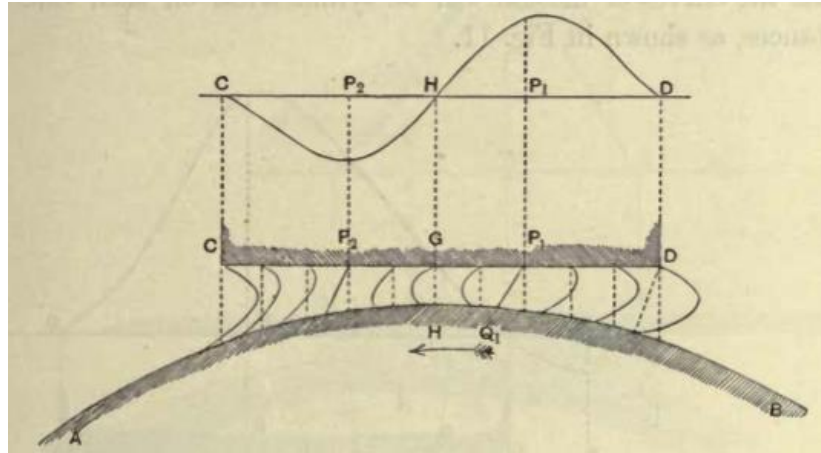
Figure 2.2:   Pressure distribution between a revolving cylindrical surface and a static plane [2].

In the upper part of figures Figure 2.1 and Figure 2.2, the pressure distribution is displayed [2]:

- for the first configuration the pressure of the intervening film of fluid would cause a force tending to separate the surfaces;

- for the second configuration the fluid pressure acts to separate the surfaces on the right, but as the pressure is negative on the left, the surfaces will be drawn together. So that the total effect will be to produce a turning moment on the surface **AB**.

In the following part of this chapter the Reynolds's equation will be determined and integrated to find the pressure distribution inside the rod-end. Then, the integration of this pressure distribution over the bearing area will allow to find the load capacity of the lubricating film.

2.1 Reynolds equation

Hydrodynamic lubrication can be expressed mathematically in the form of an equation which was originally derived by Reynolds [2] and is commonly known throughout the literature as the 'Reynolds equation'.

This equation can be derived from a simplification of the Navier-Stokes momentum and continuity equations. It is, however, more often derived by considering the equilibrium of an element of liquid subjected to viscous shear, by applying the continuity of flow principle [3].

All the simplifying assumptions necessary for the derivation of the Reynolds equation are summarized in Table 2.1 [4].

	Assumption	Comment
1	Body forces are neglected	Always valid, since there are no extra outside fields of forces acting on the fluids.
2	Pressure is constant through the film	Always valid, since the range of hydrodynamic films thickness is small.
3	No slip at the boundaries	Always valid, since the velocity of the oil layer adjacent to the boundary is the same as that of the boundary.
4	Lubricant behaves as a Newtonian fluid	Usually valid with certain exceptions, e.g. polymeric oils.
5	Flow is laminar	Usually valid, except large bearings, e.g. turbines.
6	Fluid inertia is neglected	Valid for low bearing speeds or high loads, where inertia is small compared to the viscous shear. Inertia effects could be included in more exact analyses.
7	Fluid density is constant	Usually valid for fluids when there is not much thermal expansion. Definitely not valid for gases.
8	Viscosity is constant throughout the film	Crude assumption but necessary to simplify the calculations, although it is not true. Viscosity is not constant throughout the generated film.

Table 2.1:   Summary of simplifying assumptions in hydrodynamics [4].

As said before the easiest way to deduce the Reynolds equation is by considering the equilibrium of an infinitesimal element of fluid from the hydrodynamic film. For simplicity, it is assumed that the forces on the element are initially acting in the 'x' direction only (Figure 2.3) [3].
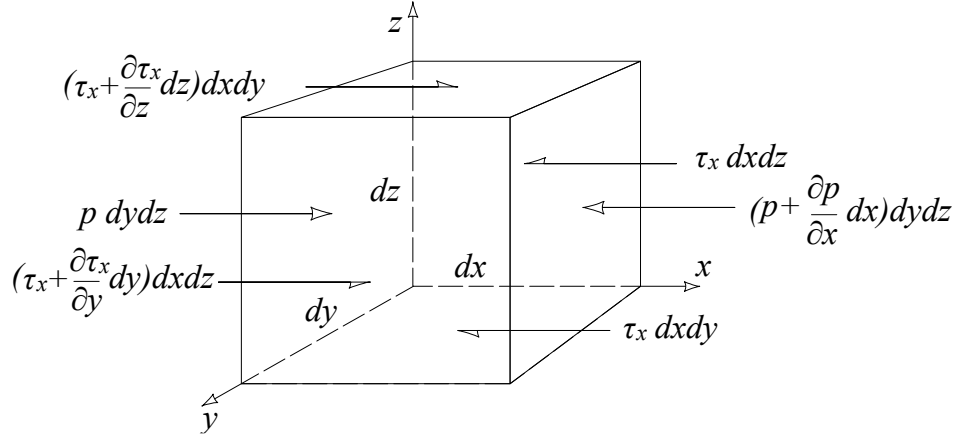
Figure 2.3:   Equilibrium of an element of fluid from the hydrodynamic film [3].

Since the element is in equilibrium, the forces acting on the left side must balance the forces acting on the right side:

$$p\,dy\,dz + \left(\tau_x + \frac{\partial \tau_x}{\partial z}dz\right)dxdy + \left(\tau_x + \frac{\partial \tau_x}{\partial y}dy\right)dxdz =$$
$$= \left(p + \frac{\partial p}{\partial x}dx\right)dydz + \tau_x dydz + \tau_x dxdy \tag{2.3}$$

where:

p is the pressure (Pa);

τ_x is the shear stress acting in the 'x' direction (Pa).

Assuming that the volume is different from zero ($dx\,dy\,dz \neq 0$), both sides of equation (2.3) can be divided by this value, obtaining:

$$\frac{\partial \tau_x}{\partial z} + \frac{\partial \tau_x}{\partial y} = \frac{\partial p}{\partial x} \tag{2.4}$$

Following the same procedure, taking under consideration only the forces acting along the 'y' direction, we can find the second equilibrium condition:

$$\frac{\partial \tau_y}{\partial z} + \frac{\partial \tau_y}{\partial x} = \frac{\partial p}{\partial y} \tag{2.5}$$

In the 'z' direction, since the pressure is constant through the film (Assumption 2), the pressure gradient is equal to zero:

$$\frac{\partial p}{\partial z} = 0 \tag{2.6}$$

Now the assumption of Newtonian lubricant (Assumption 4) has to be used (see Appendix A); the shear stress τ can be expressed in terms of dynamic viscosity and shear rates, as shown in equation (2.7):

$$\begin{cases} \tau_x = \mu \dfrac{\partial u}{\partial z} \\ \tau_y = \mu \dfrac{\partial v}{\partial z} \end{cases} \tag{2.7}$$

where:

    τ_y is the shear stress acting in the 'y' direction (Pa);

    u is the sliding velocity in the 'x' direction (m/s);

    v is the sliding velocity in the 'y' direction (m/s);

    μ is the dynamic viscosity (Pas).

Since the viscosity of the fluid is constant throughout the film (Assumption 8), the substitution of equations (2.7) into (2.4) and (2.5) gives:

$$\begin{cases} \dfrac{\partial^2 u}{\partial z^2} + \dfrac{\partial^2 u}{\partial y \partial z} = \dfrac{1}{\mu} \dfrac{\partial p}{\partial x} \\ \dfrac{\partial^2 v}{\partial z^2} + \dfrac{\partial^2 v}{\partial x \partial z} = \dfrac{1}{\mu} \dfrac{\partial p}{\partial y} \end{cases} \tag{2.8}$$

At this stage another assumption needs to be done; since u and v, to a lesser degree, are the predominant velocities and 'z' is a dimension much smaller than 'x' and 'y', compared with the two velocity gradients $\partial u / \partial z$ and $\partial v / \partial z$ all other velocity gradients are considered negligible [5].

With this assumption the second terms on the left side of equation (2.8) drop out giving the equilibrium conditions for the forces acting in the 'x' and 'y' directions:

$$\begin{cases} \dfrac{\partial^2 u}{\partial z^2} = \dfrac{1}{\mu}\dfrac{\partial p}{\partial x} \\ \dfrac{\partial^2 v}{\partial z^2} = \dfrac{1}{\mu}\dfrac{\partial p}{\partial y} \end{cases} \tag{2.9}$$

Equations (2.9) can now be integrated. Separating the variables,

$$\begin{cases} u = \dfrac{1}{\mu}\dfrac{\partial p}{\partial x}\dfrac{z^2}{2} + C_1\, z + C_2 \\ v = \dfrac{1}{\mu}\dfrac{\partial p}{\partial y}\dfrac{z^2}{2} + C_3\, z + C_4 \end{cases} \tag{2.10}$$

where:

C_1, C_2, C_3 and C_4 are integration constants;

and, considering the following boundary conditions:

$$\begin{cases} u = U_1 & at & z = 0 \\ u = U_2 & at & z = h \\[4pt] v = V_1 & at & z = 0 \\ v = V_2 & at & z = h \end{cases} \tag{2.11}$$

where:

h is the thickness of the lubricant meatus, function of 'x' and 'y' (m);

equations (2.12) give the velocity profile in the fluid film affected by the viscosity μ, the film shape h, surface velocities U_1, U_2, V_1, V_2 and the pressure gradients:

$$\begin{cases} u = \dfrac{1}{2\mu}\dfrac{\partial p}{\partial x}\, z(z - h) + \dfrac{h - z}{h}\, U_1 + \dfrac{z}{h}\, U_2 \\ v = \dfrac{1}{2\mu}\dfrac{\partial p}{\partial y}\, z(z - h) + \dfrac{h - z}{h}\, V_1 + \dfrac{z}{h}\, V_2 \end{cases} \tag{2.12}$$

Now, the continuity equation is introduced (2.13) [5]:

$$\frac{\partial \rho}{\partial t} + \frac{\partial(\rho u)}{\partial x} + \frac{\partial(\rho v)}{\partial y} + \frac{\partial(\rho w)}{\partial z} = 4\pi\rho m \tag{2.13}$$

where

u is the sliding velocity in the 'x' direction (m/s);

v is the sliding velocity in the 'y' direction (m/s);

w is the velocity in the 'z' direction (m/s);

ρ is the density of the fluid (kg/m³);

m is the generation of conserved quantity inside the element (1/s). It represents the presence of sources and sinks.

With the state of lubricant time-independent and with no sources or sinks, the continuity equation can be written as:

$$\frac{\partial(\rho w)}{\partial z} = -\frac{\partial(\rho u)}{\partial x} - \frac{\partial(\rho v)}{\partial y} \tag{2.14}$$

Substituting u and v, (2.12), into the continuity equation (2.14):

$$\frac{\partial(\rho w)}{\partial z} = -\frac{1}{2}\left(\frac{\partial}{\partial x}\left(\frac{\rho}{\mu}\frac{\partial p}{\partial x}(z^2 - hz)\right) + \frac{\partial}{\partial y}\left(\frac{\rho}{\mu}\frac{\partial p}{\partial y}(z^2 - hz)\right)\right) + \\ -\frac{\partial}{\partial x}\rho\left(\frac{h-z}{h}U_1 + \frac{z}{h}U_2\right) - \frac{\partial}{\partial y}\rho\left(\frac{h-z}{h}V_1 + \frac{z}{h}V_2\right) \tag{2.15}$$

By integrating with respect to 'z' with the following boundary conditions,

$$\begin{cases} w = W_1 & at \quad z = 0 \\ w = W_2 & at \quad z = h \end{cases} \tag{2.16}$$

and making use of the next relation (as long as $h = h(x, y)$) [5]:

$$\int_0^{h(\alpha)} \frac{\partial}{\partial \alpha} f(z, \alpha)\,dz = \frac{\partial}{\partial \alpha}\int_0^{h(\alpha)} f(z, \alpha)\,dz - f(h(\alpha), \alpha)\frac{\partial h(\alpha)}{\partial \alpha} \tag{2.17}$$

the generalized Reynolds equation in three dimensions is obtained:

$$
\frac{\partial}{\partial x}\left(\frac{\rho h^3}{\mu}\frac{\partial p}{\partial x}\right) + \frac{\partial}{\partial y}\left(\frac{\rho h^3}{\mu}\frac{\partial p}{\partial y}\right) = 6\left((U_1 - U_2)\frac{\partial(\rho h)}{\partial x} + (V_1 - V_2)\frac{\partial(\rho h)}{\partial y}\right) +
$$
$$
+ 6\rho h\left(\frac{\partial}{\partial x}(U_1 + U_2) + \frac{\partial}{\partial y}(V_1 + V_2)\right) + 12\rho(W_2 - W_1) \tag{2.18}
$$

In equation (2.18):

- on the left-hand side we have the pressure terms;

- the first right-hand term is the contribution to the pressure due to the variation of the film thickness along 'x' and 'y' directions;

- the second term on the right-hand side implies a variation of tangential velocities;

- the third term on the right-hand side is due to the relative velocity of surfaces in a direction normal to the fluid film ('z').

As said $(W_2 - W_1)$ represents the resultant normal velocity regardless of what produces it. In thrust bearings, this velocity can come only from the actual normal movement of the sliding surface. However, in journal bearings, as shown in Figure 2.4, a normal relative velocity can come from two sources [5]:

- from the rotational velocity of the sliding surfaces;

- from any actual motion of journal centre.
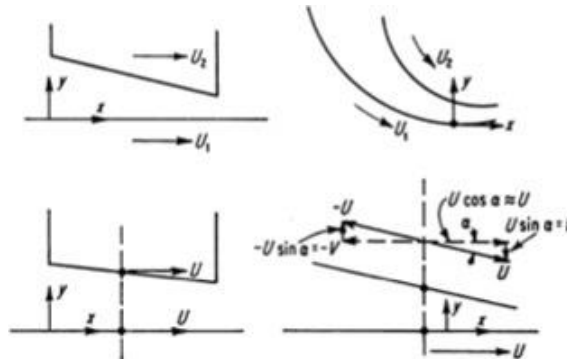
Figure 2.4:   The effect of movement of bearing surfaces [5].

It is convenient to express the last term of equation (2.18) only by the radial velocity that results from the motion of the shaft centre. By referring to Figure 2.4 and expanding the consideration previously made also along the 'y' direction:

$$W_2 - W_1 = U_2 \sin \alpha_x + V_2 \sin \alpha_y + W_0 \cong U_2 \tan \alpha_x + V_2 \tan \alpha_y + W_0 =$$
$$= U_2 \frac{\partial h}{\partial x} + V_2 \frac{\partial h}{\partial y} + W_0 \tag{2.19}$$

where:

α_x is the angle between U_2 and 'x' direction (rad);

α_y is the angle between V_2 and 'y' direction (rad);

W_0 is the motion of journal centre (m/s).

Defining $U = U_1 + U_2$ and $V = V_1 + V_2$, the generalized Reynolds equation can be rewritten in the following manner:

$$\frac{\partial}{\partial x}\left(\frac{\rho h^3}{\mu}\frac{\partial p}{\partial x}\right) + \frac{\partial}{\partial y}\left(\frac{\rho h^3}{\mu}\frac{\partial p}{\partial y}\right) = 6\left(U\frac{\partial(\rho h)}{\partial x} + V\frac{\partial(\rho h)}{\partial y}\right) +$$
$$+ 6\rho h\left(\frac{\partial}{\partial x}U + \frac{\partial}{\partial y}V\right) + 12\rho W_0 \tag{2.20}$$

2.2   Simplification and integration

As said in the introduction chapter, each rod-end in the ESHA system is modelled as a journal bearing.

A list of significant features of real journal bearings is shown in Table 2.2. In the last column of the table is expressed whether or not the specific feature is taken under consideration in this work.

	Feature	Comment	In consideration?
1	Leakage and sinks	In the process the lubricant is continuously squeezed out the ends of the bearing, thus inlet fluid port may be needed.	No. Lubricant leakage is neglected.
2	Striation / Cavitation	The fluid film in journal bearing is rarely complete. For most liquids a phenomenon known as cavitation occurs when the pressure falls below atmospheric pressure. The reason for this is that most liquids contain dissolved air and minute dirt particles. If there is a significant drop in pressure, the operating temperature can be sufficient for the lubricant to evaporate. The lubricant vapour accumulates in the bubbles and their sudden collapse is the cause of most cavitation damage. Wear caused by vaporous cavitation progressively damages the bearing until it ceases to function effectively. The risk of vaporous cavitation occurring increases with elevation of bearing speeds and loads [7].	No. The determination of cavitation boundary is difficult and computationally expensive.
3	Unbalance	Journals could have some residual unbalance. This will affect the dynamic behaviour.	No. The journal has isotropic proprieties.

4	Heat transfer	Not all the energy generated in a bearing is carried away as heat by the lubricant. Part of that energy is dissipated by conduction and radiation via the bearing shell, housing and journal.	No. Heat generation and transfer are not taken under consideration in this work.
5	Elastic deformation	Under heavy loads, both bearing and journal surfaces can deform. This effect will produce a different film shape with drastic changes in performances.	No. Journal and bearing have non-deformable surfaces in the hydrodynamic lubrication model.
6	Thermal expansion	When journal and bearing materials have different coefficient of thermal expansion, under appreciable temperature changes, the clearances will not retain their original shape.	No. Journal and bearing thermal expansion coefficients are equal.
7	Turbulence	High speed, large clearances and low viscosity will cause turbulence with a resulting rise in power loss and a drop in lubricant flow.	No. The Reynolds equation is based on the assumption of laminar flow (Table 2.1).
8	Misalignment	Assembly errors and particular work conditions cloud create axial misalignment.	No. Journal and bearing axis are always parallel.
9	Variable viscosity	The viscosity of the lubricant never remains constant. The viscosity of any fluid varies both with temperature and pressure.	Yes. Vogel-Barus equation allows to take under consideration temperature and pressure dependencies.
10	Surface roughness	When the lubricant film thickness has the same order on magnitude as the surface roughness, hydrodynamic lubrication requirements may not occur.	Yes. A contact and a mixed hydrodynamic-contact models are developed.

Table 2.2: Real journal bearing features (adapted form [5]).

2.2.1 Reynolds equation for dynamic loaded journal bearing

Let's take under consideration a generic journal bearing, as shown in Figure 2.5. A journal bearing consists of a shaft (that's called journal) rotating within a stationary bush (called bearing).
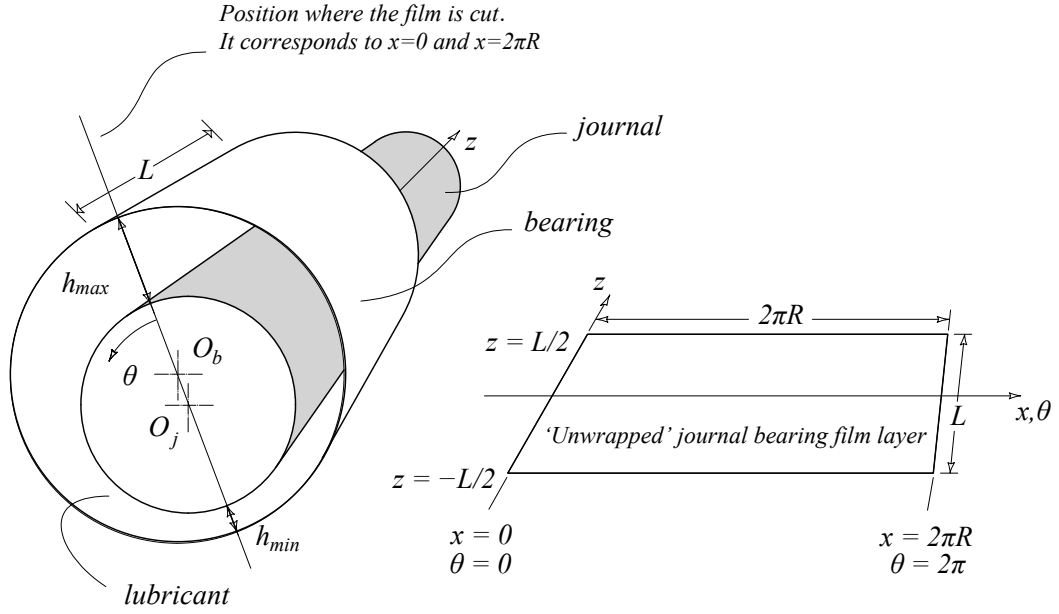
Figure 2.5: Unwrapped journal bearing scheme [3].

As shown in the previous figure, a cartesian reference system, with the following orientation, has been chosen:

- 'x'-axis directed along the circumferential direction;

- 'y'-axis directed along the radial direction;

- 'z'-axis directed along the axial direction.

By choosing the unidirectional velocity approximation, that imposes the relative axial speed, between the journal and the bearing, equal to zero and considering the lubricant as incompressible ($\rho = 0$), it's possible to rewrite the Reynolds equation (2.20) using the new reference system:

$$\frac{\partial}{\partial x}\left(\frac{h^3}{\mu}\frac{\partial p}{\partial x}\right) + \frac{\partial}{\partial z}\left(\frac{h^3}{\mu}\frac{\partial p}{\partial z}\right) = 6U\frac{\partial h}{\partial x} + 6h\frac{\partial U}{\partial x} + 12V_0 \tag{2.21}$$

Usually, the effect of hydrodynamic pressure is looked as the contribution of two different actions: wedge and squeezing. The squeeze action relates the radial journal motion with the generation of load carrying capacity in the lubricant film (effect 1), whilst the wedge action deals with the relation between relative rotational velocity of the journal and bearing and the ability to produce such pressure [8]. Here, the hydrodynamic forces will consist of the contribution made by the progression of shaft centre (effect 2) and that due to the rotation of the journal about its own centre (effect 3).

In equation (2.21) we have the mathematical writing of what just said [5]:

- the first term, $6U \ \partial h/\partial x$, represents the action of the journal, rotating with the tangential velocity U, over a wedge-shaped lubricant film given by $h(x)$ (effect 3). In order for this term to generate positive pressure it must be negative, since the wedge-shaped film implies that $\partial h/\partial x < 0$;

- the second term, $6h \ \partial U/\partial x$, implies a variation of tangential velocity along the journal surface (effect 2) and, in order for this term to contribute to positive pressure $\partial U/\partial x$ must be negative;

- the last term is the expression for the velocity of shaft centre and it's responsible for the squeezing effect (effect 1). Since $V_0 = \partial h/\partial t$, it can be seen that, when V_0 acts in the same direction as the applied load, the lubricant film will decrease $\partial h/\partial t < 0$ and the velocity will contribute to the load capacity.

To be able to integrate this equation, we need to find expressions for the film thickness h and the velocities U and V_0.

Let's start with the geometrical definition of the film thickness. In Figure 2.6 a normal section with respect to the 'z'-axis is shown, where:

O_j and R_j are the centre and the radius (m) of the journal;

O_b and R_b are the centre and the radius (m) of the bearing;

e is the eccentricity (distance $\overline{O_b O_j}$ between the centres of journal and bearing during the operation) (m);

h is the film thickness (m);

θ represents the coordinate in the circumferential direction, being measured from the maximum film thickness and with counter clockwise direction (rad).

It should be noted that the angle 'α' is very small; this allows the evaluation of h and θ along the line that connects O_j and A (generic point on the bearing surface).
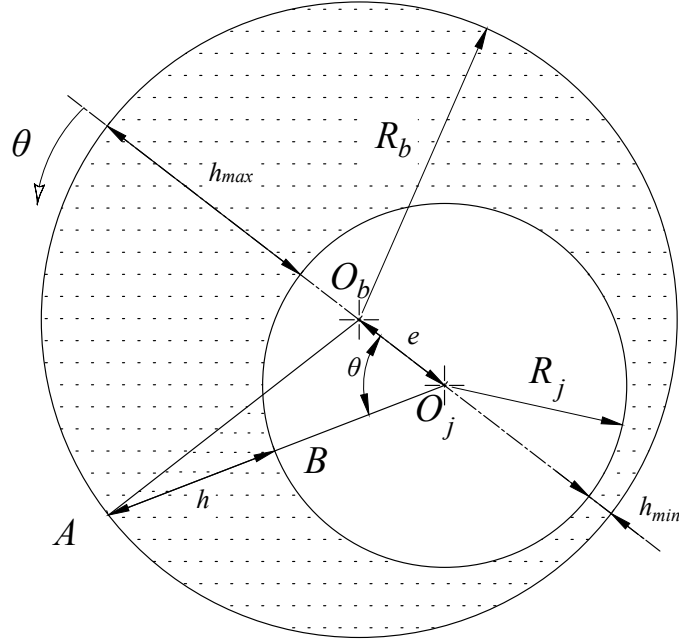
Figure 2.6: Cross section of a journal bearing: basic geometry.
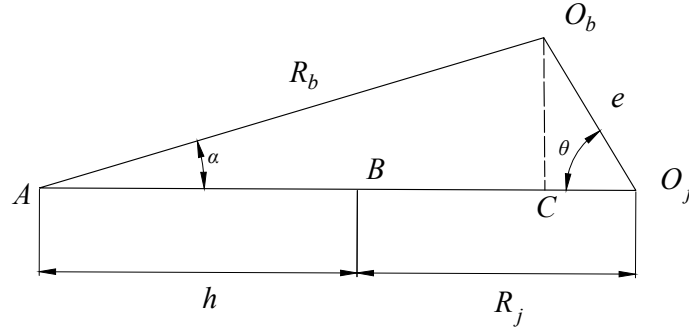
Figure 2.7: Geometry detail for the evaluation of film shape in journal bearings.

Considering the triangle $O_b O_j A$ from Figure 2.6, which is shown in detail in Figure 2.7, it can be written:

$$O_j A = O_j C + CA = O_j B + BA \tag{2.22}$$

28

or

$$O_j A = e\, cos\theta + R_b cos\alpha = R_j + h \tag{2.23}$$

Thus,

$$h = e\, cos\theta + R_b cos\alpha - R_j \tag{2.24}$$

applying the sine rule and remembering that:

$$sin^2\alpha + cos^2\alpha = 1 \tag{2.25}$$

we obtain:

$$\begin{cases} sin\alpha = \dfrac{e}{R_b}\, sin\theta \\[2em] cos\alpha = \sqrt{1 - \left(\dfrac{e}{R_b}\right)^2 sin^2\theta} \end{cases} \tag{2.26}$$

Since $e/R_b \ll 1$, substituting (2.26) into (2.24) yields:

$$h = C + e\, cos\theta += C(1 + \varepsilon\, cos\theta) \tag{2.27}$$

where:

C is the clearance (the difference between the radii of bush and shaft $R_b - R_j$) (m);

$\varepsilon = \dfrac{e}{C}$ is the eccentricity ratio, (-).

Equation (2.27) gives a description of the film shape in journal bearings to within 0.1% accuracy [4].

The relative motion of the journal and the bearing surfaces introduces both tangential, U, and normal, V_0, components of velocity. These velocities can be expressed in terms of the journal bearing components by noting that the journal rotates about its own axis and translates with respect to the bearing centre.

Figure 2.8 shows the velocity components in a cross section of a journal bearing dynamically loaded, where:

F_{ext} is the external load acting on the journal centre; this force may vary both in magnitude and direction (N);

φ is the angle that expresses the direction of the external force (rad). By convention this angle has been referred to the vertical line and it has been assigned as positive if the direction is counter clockwise;

Φ is the angle between the external load line and the line of centres, it's called "attitude angle" (rad). By convention this angle always starts from the load line and ends at the line of centres and it has positive value if the direction is counter clockwise;

e is the eccentricity, it expresses the radial position of the journal centre with respect to the bearing centre (m);

χ is the angle that expresses the angular position of the journal centre with respect to the vertical line (rad); it's given by the sum of φ and Φ;

ω is the angular velocity of the journal with respect to its centre (rad/s). It's positive if it has counter clockwise direction.

Any point P', on the surface of the journal at angular position θ, has tangential and normal velocities relative to P on the surface of the bearing. These velocities are made up by the components of the velocity of journal centre relative to the bearing centre plus the velocity of the surface of the journal about its own centre (Figure 2.8). Thus:

$$\begin{cases} U = \omega R_j \cos\alpha + \dfrac{de}{dt}\sin\theta - e\,\dfrac{d(\varphi + \Phi)}{dt}\cos\theta \\ V_0 = -\omega R_j \sin\alpha + \dfrac{de}{dt}\cos\theta + e\,\dfrac{d(\varphi + \Phi)}{dt}\sin\theta \end{cases} \tag{2.28}$$

or

$$\begin{cases} U = \omega R_j \cos\alpha + C\dfrac{d\varepsilon}{dt}\sin\theta - C\varepsilon\,\dfrac{d(\varphi + \Phi)}{dt}\cos\theta \\ V_0 = -\omega R_j \sin\alpha + C\dfrac{d\varepsilon}{dt}\cos\theta + C\varepsilon\,\dfrac{d(\varphi + \Phi)}{dt}\sin\theta \end{cases} \tag{2.29}$$
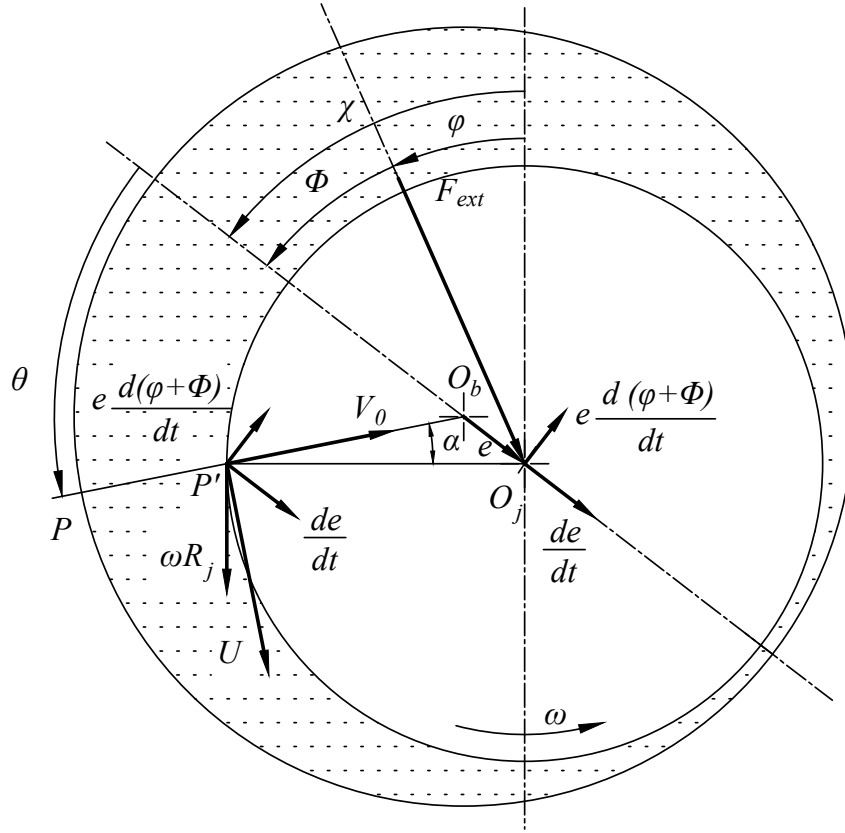
Figure 2.8:   Cross section of a journal bearing: velocity components.

Since the angle α is very small, the tangential velocity component can be rewritten as:

$$\begin{cases} \omega R_j \, cos\alpha \approx \omega R_j \\ \omega R_j \, sin\alpha \approx \omega R_j \, \alpha \end{cases} \tag{2.30}$$

By substituting (2.30) into (2.29):

$$\begin{cases} U = \omega R_j + C \dfrac{d\varepsilon}{dt} \, sin\theta - C\varepsilon \dfrac{d(\varphi + \Phi)}{dt} \, cos\theta \\ V_0 = -\omega R_j \, \alpha + C \dfrac{d\varepsilon}{dt} \, cos\theta + C\varepsilon \dfrac{d(\varphi + \Phi)}{dt} \, sin\theta \end{cases} \tag{2.31}$$

The Reynolds' equation (2.21) should be expressed in term of the journal bearing variables e, φ, Φ and θ.

The x coordinate, in the unwrapped film, is written as

$$x = R_j\,\theta \qquad \text{and, hence,} \qquad \partial x = R_j\,\partial\theta \qquad (2.32)$$

By deriving equations (2.27) and (2.31) we obtain:

$$\begin{cases} \dfrac{dh}{d\theta} = -C\varepsilon\,sin\theta \\ \dfrac{dU}{d\theta} = C\dfrac{d\varepsilon}{dt}\,cos\theta + C\varepsilon\dfrac{d(\varphi + \Phi)}{dt}\,sin\theta \end{cases} \qquad (2.33)$$

Substituting (2.31) and (2.33) into (2.21), Reynolds equation can be rewritten in the following form:

$$\frac{\partial}{\partial x}\left(\frac{h^3}{\mu}\frac{\partial p}{\partial x}\right) + \frac{\partial}{\partial z}\left(\frac{h^3}{\mu}\frac{\partial p}{\partial z}\right) =$$

$$= 6\left(\left(\left(\omega - 2\frac{d\varphi}{dt} - 2\frac{d\Phi}{dt} - 2\frac{C\varepsilon}{R_j}\,cos\theta\left(\frac{d\varphi}{dt} + \frac{d\Phi}{dt}\right) - \frac{C}{R_j}\left(\frac{d\varphi}{dt} + \frac{d\Phi}{dt}\right)\right)\frac{dh}{d\theta}\right.\right.$$

$$\left.\left. + \left(2C\frac{d\varepsilon}{dt}cos\theta + \frac{C^2\varepsilon}{R_j}\frac{d\varepsilon}{dt}(sin^2\theta - cos^2\theta) + \frac{C^2}{R_j}\frac{d\varepsilon}{dt}cos\theta\right)\right)\right) \qquad (2.34)$$

Now considering that $C/R_j \ll 1$ and $e/R_j \ll 1$ the fourth, the fifth, the seventh and the eighth terms on the right-hand side of equation (2.34) are negligible. The previous equation can be rewritten as:

$$\frac{\partial}{\partial x}\left(\frac{h^3}{\mu}\frac{\partial p}{\partial x}\right) + \frac{\partial}{\partial z}\left(\frac{h^3}{\mu}\frac{\partial p}{\partial z}\right) = 6\left(\left(\omega - 2\frac{d\varphi}{dt} - 2\frac{d\Phi}{dt}\right)\frac{dh}{d\theta} + 2C\frac{d\varepsilon}{dt}cos\theta\right) \qquad (2.35)$$

Equation (2.35) is the form of the Reynolds equation which is suitable for the present analysis.

Equation (2.35) enables the calculation of the pressure field in a hydrodynamic loaded journal bearing as a function of the dynamic parameters $\omega, \dot{\varphi}, \dot{\Phi}, \varepsilon$ and $\dot{\varepsilon}$.

Commonly, the load angular rotation $\dot{\varphi}$ and the journal angular velocity ω are prescribed a priori as function of the mechanism configuration and the aerodynamic force acting on the controlled flight surface (Chapter 5), whereas $\dot{\Phi}$, ε and $\dot{\varepsilon}$ should be obtained in connection with the load instantaneous value from the dynamic analysis of the system.

2.2.2 Numerical integration with finite difference method

Reynolds equation given by (2.35) is one non-homogeneous partial differential equation of elliptical type and the exact solution is very difficult to obtain [9].

Equation (2.35) can be solved with a numerical procedure. In this work a numerical integration of Reynolds equation has been developed using the finite difference method. It consists in approximating the differential operator by replacing the derivatives in the equation using differential quotients. The domain is partitioned in space and in time and approximations of the solution are computed at the space nodes at any instant of time. The error between the numerical solution and the exact solution is determined by the error that is committed by going from a differential operator to a difference operator. This error is called the "discretization error" or "truncation error". The term "truncation error" reflects the fact that a finite part of a Taylor series is used in the approximation.

Equation (2.35) can be rewritten as:

$$\frac{\partial}{\partial x}\left(\lambda \frac{\partial p}{\partial x}\right) + \frac{\partial}{\partial z}\left(\lambda \frac{\partial p}{\partial z}\right) = f \tag{2.36}$$

where:

$\lambda = \dfrac{h^3}{\mu}$ is the coefficient of the derivatives (m³/Pas);

$f = 6\left(\left(\omega - 2\dfrac{d\varphi}{dt} - 2\dfrac{d\Phi}{dt}\right)\dfrac{dh}{d\theta} + 2C\dfrac{d\varepsilon}{dt}cos\theta\right)$ is the known term for each point of the discretization at any instant of time (m/s).

By using the finite difference method each derivative is substituting with a central differential quantity as:

$$\frac{\partial u}{\partial x} \cong \frac{u(x + \Delta x) - u(x - \Delta x)}{2\Delta x} \tag{2.37}$$

where:

$u \subseteq I \to \mathbb{R}$ is a generic function defined in I and derivable;

Δx is a generic increment such that $u(x + \Delta x)$ and $u(x - \Delta x)$ are still inside the range I.

The goal is the determination of the pressure distribution, due to the hydrodynamic lubrication, over the journal surface in order to be able to write the equations that describe the dynamic of this element. To do this, the first step is the definition of a finite difference mesh over the journal, as shown in Figure 2.9 and more in detail Figure 2.10:
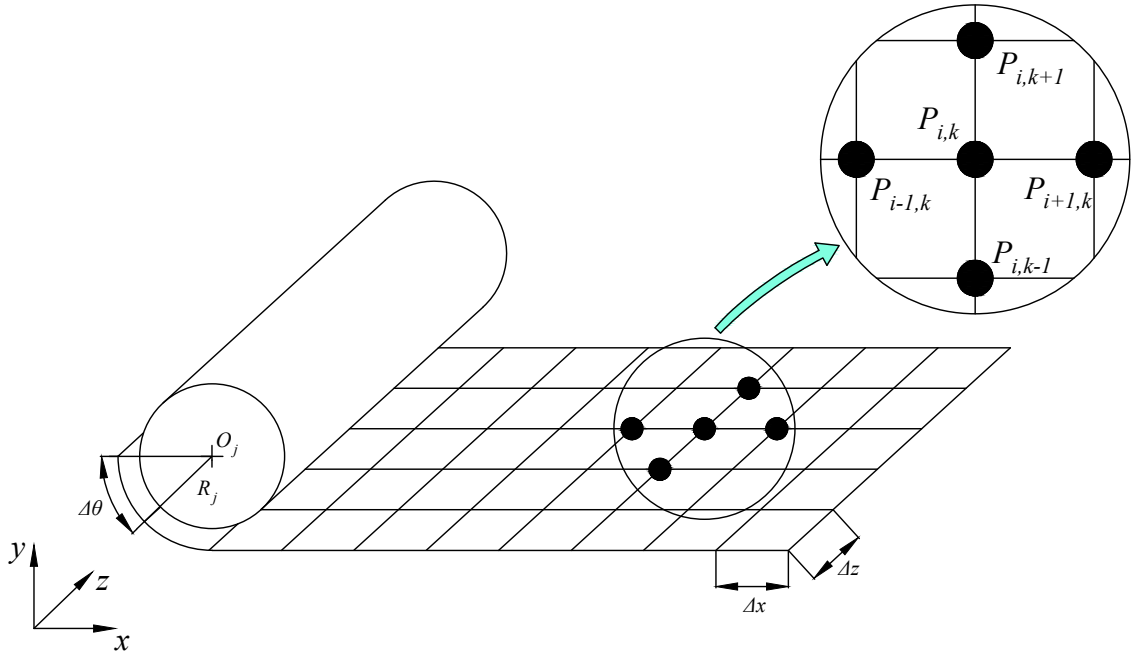
Figure 2.9: Finite difference mesh developed over the journal.

The journal surface is divided in $m + 1$ intervals along the 'x'-axis an in $n + 1$ intervals along the 'z'-axis. The discretization has the following characteristics:

- $m + 2,\ m$ respectively the number of total nodes and the number of internal nodes along the 'x'-axis;

- $n + 2,\ n$ respectively the number of total nodes and the number of internal nodes along the 'z'-axis;

34

- $\Delta x = \frac{2\pi R_j}{m+1}$ is the discretization step along the 'x'-axis;

- $\Delta z = \frac{L}{n+1}$ is the discretization step along the 'z'-axis.
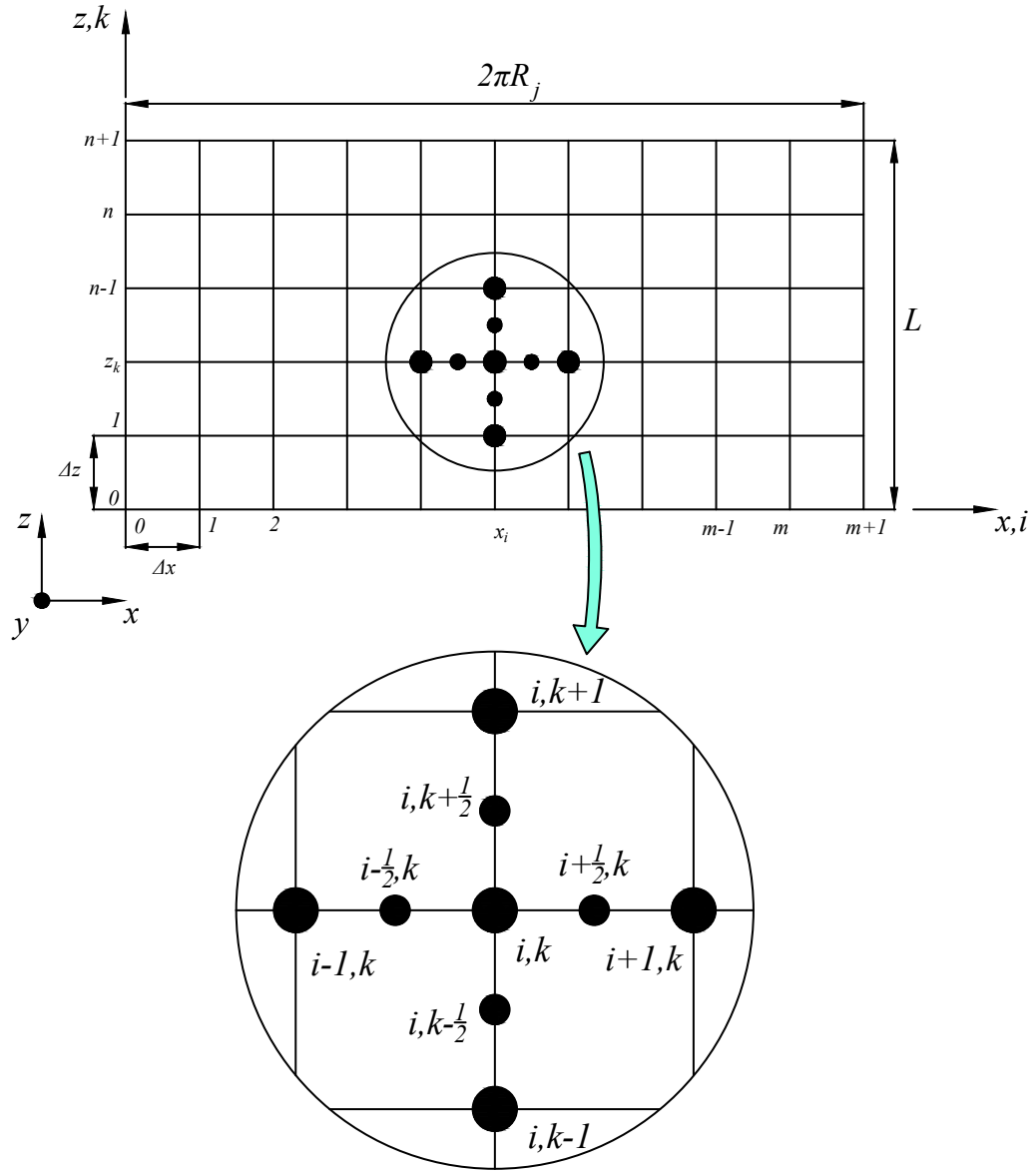
Figure 2.10:   Detail of the discretization over the journal.

The nodes sitting inside the grid are indexed by i and k such that $1 \leq i \leq m$ and $1 \leq k \leq n$, whereas the boundary nodes are characterised by having at least one index equal a 0, $m + 1$ or $n + 1$.

Therefore, a generic node of the discretization is identified by the following set of coordinates:

$$\begin{cases} x_i = i \, \Delta x \\ z_k = k \, \Delta z \end{cases} \tag{2.38}$$

where:

$0 \leq i \leq m + 1$ i: index that represents the generic node associated to the 'x'-axis;

$0 \leq k \leq n + 1$ k: index that represents the generic node associated to the 'z'-axis.

In equation (2.36) the coefficient $\lambda = h^3/\mu$ is not constant over the journal surface due to the dependency of h from x. For that reason, auxiliary subdivision nodes are added to the main discretization (which is represented in Figure 2.10 with bigger circles and indicated with the following nomenclature: $(i, k - 1)$, $(i - 1, k)$ and so on). Both along the 'x' and the 'z' directions, inside each main discretization intervals, a secondary auxiliary node is added (in Figure 2.10 the auxiliary nodes are represented with smaller circles and indicated with the nomenclature: $(i, k - \frac{1}{2})$, $(i - \frac{1}{2}, k)$ and so on).

With this type of discretization, the pressure and known term values will be calculated over the main nodes, meanwhile the coefficients λ over the secondary nodes. For brevity, the symbol (i, k) will stand for the node (x_i, z_k) from now on.

Indicate with $p_{i,k} \simeq p(x_i, z_k)$ an approximation of the pressure p at the node (x_i, z_k); moreover, let $f_{i,k} \simeq f(x_i, z_k)$ and $\lambda_{i,k} \simeq \lambda(x_i, z_k)$. Substituting in equation (2.36) the following equations:

$$\begin{cases} \tau_x = \lambda \, \dfrac{\partial p}{\partial x} \\ \tau_z = \lambda \, \dfrac{\partial p}{\partial z} \end{cases} \tag{2.39}$$

and using the differential quotients described in (2.37), along the 'x' direction we obtain:

$$\frac{\partial \tau_x}{\partial x} \cong \frac{\tau_{i+\frac{1}{2},k} - \tau_{i-\frac{1}{2},k}}{\Delta x} \tag{2.40}$$

where:

$$\begin{cases} \tau_{i+\frac{1}{2},k} = \lambda_{i+\frac{1}{2},k} \dfrac{p_{i+1,k} - p_{i,k}}{\Delta x} \\ \tau_{i-\frac{1}{2},k} = \lambda_{i-\frac{1}{2},k} \dfrac{p_{i,k} - p_{i-1,k}}{\Delta x} \end{cases} \tag{2.41}$$

Thus:

$$\frac{\partial}{\partial x}\left(\lambda \frac{\partial p}{\partial x}\right) \cong \frac{\lambda_{i+\frac{1}{2},k} \dfrac{p_{i+1,k} - p_{i,k}}{\Delta x} - \lambda_{i-\frac{1}{2},k} \dfrac{p_{i,k} - p_{i-1,k}}{\Delta x}}{\Delta x} \tag{2.42}$$

or,

$$\frac{\partial}{\partial x}\left(\lambda \frac{\partial p}{\partial x}\right) \cong \frac{\lambda_{i-\frac{1}{2},k}\, p_{i-1,k} - \left(\lambda_{i-\frac{1}{2},k} + \lambda_{i+\frac{1}{2},k}\right) p_{i,k} + \lambda_{i+\frac{1}{2},k}\, p_{i+1,k}}{\Delta x^2} \tag{2.43}$$

In a similar manner, an equation for the derivatives in the 'z' direction is obtained:

$$\frac{\partial}{\partial z}\left(\lambda \frac{\partial p}{\partial z}\right) \cong \frac{\lambda_{i,k-\frac{1}{2}}\, p_{i,k-1} - \left(\lambda_{i,k-\frac{1}{2}} + \lambda_{i,k+\frac{1}{2}}\right) p_{i,k} + \lambda_{i,k+\frac{1}{2}}\, p_{i,k+1}}{\Delta z^2} \tag{2.44}$$

Substituting equations (2.43) and (2.44) into (2.36), the full discretized Reynolds equation is obtained:

$$\begin{aligned} \frac{\lambda_{i,k-\frac{1}{2}}}{\Delta z^2}\, p_{i,k-1} &+ \frac{\lambda_{i-\frac{1}{2},k}}{\Delta x^2}\, p_{i-1,k} - \left(\frac{\lambda_{i-\frac{1}{2},k} + \lambda_{i+\frac{1}{2},k}}{\Delta x^2} + \frac{\lambda_{i,k-\frac{1}{2}} + \lambda_{i,k+\frac{1}{2}}}{\Delta z^2}\right) p_{i,k} + \\ &+ \frac{\lambda_{i+\frac{1}{2},k}}{\Delta x^2}\, p_{i+1,k} + \frac{\lambda_{i,k+\frac{1}{2}}}{\Delta z^2}\, p_{i,k+1} \cong f_{i,k} \end{aligned} \tag{2.45}$$

Each equation links the values of the discrete pressure at five nearby nodes: the node where the equation is forced (i,k), the ones immediately above $(i,k+1)$, below $(i,k-1)$, to the left $(i-1,k)$, and to the right $(i+1,k)$. These form a so-called computational molecule, typical of the finite difference scheme considered. Borrowing from geography, we may call the molecular nodes around the central one North, South, East and West (Figure 2.9 and Figure 2.10) [10].

At this stage is important to understand which nodes of the discretization are unknown pressure quantities and which ones are already known. In this work, Dirichlet condition are used over the surface boundaries, as better explained in the following subchapter.
In this case, therefore, the number of unknown nodes will be $n \cdot m$ and they are identified with the indexes i and k such as:

$$1 \leq i \leq m$$
$$1 \leq k \leq n$$

As said, the number of unknown quantities is $n \cdot m$, consequently the exact same number of equations will be needed. In terms of matrix, therefore, the coefficients matrix will have $n \cdot m$ rows and columns for a total amount of $(n \cdot m)^2$ items.

In order to rewrite the algebraic system obtained in (2.45) into a matrix notation, we need first to replace the indices i and k with only one, say q, to number inner nodes. For this we use the lexicographic ordering (lex ordering for short), whereby the m nodes on the first row from the bottom of the grid ($n = 1$) are ordered first, then those on the second row ($n = 2$), and so on; within each row the indexing goes from left to right [10]. This kind of ordering reminds the movement of the old typewriters.
The lexicographic ordering is shown in Figure 2.11:
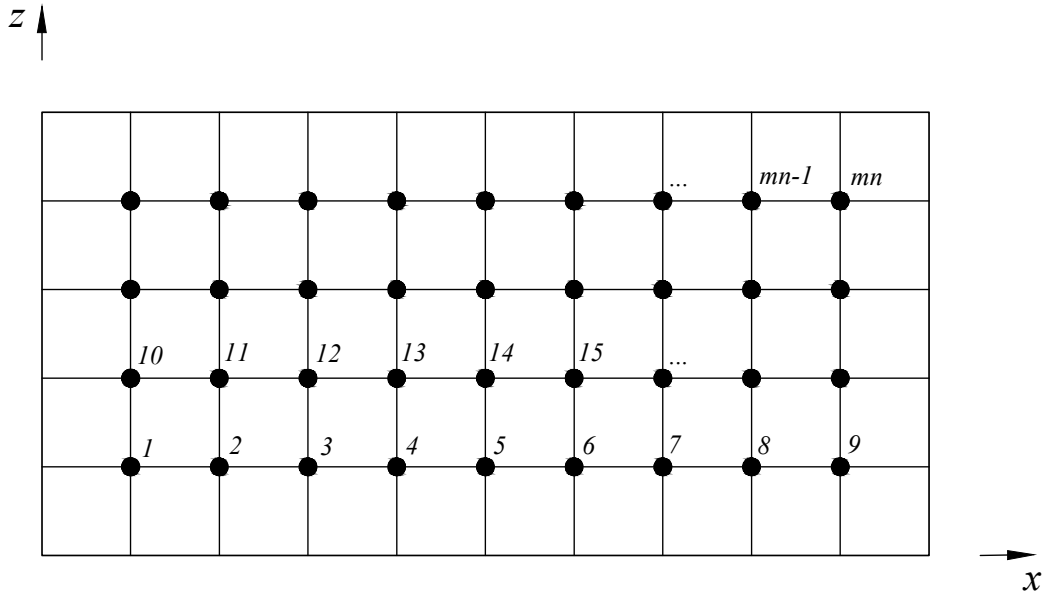
Figure 2.11:   Lexicographic ordering.

It is easy to see that:

$$q = (k - 1)\, m + i \qquad\qquad (2.46)$$

where:

$1 \leq q \leq m \cdot n$ $\qquad\qquad$ q: single index used for the matrix notation.

The right picture in Figure 2.12 shows the one-index numbering for the computational molecule of a strong inner node.
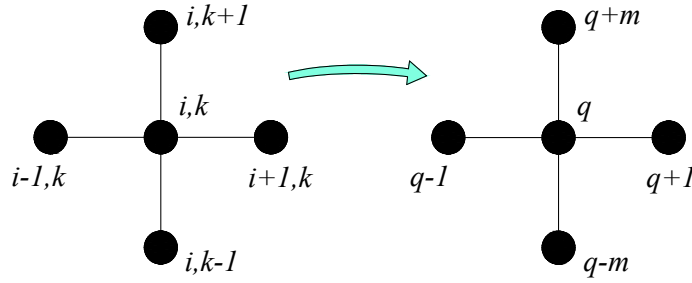
Figure 2.12:   Transition from a two indices notation to a single index one.

By setting $p_{i,k} = p_q$ and $f_{i,k} = f_q$ equation (2.45) becomes:

$$a_{q-m}\, p_{q-m} + a_{q-1}\, p_{q-1} - a_q\, p_q + a_{q+1}\, p_{q+1} + a_{q+m}\, p_{q+m} = f_q \qquad\qquad (2.47)$$

where:

$$
\begin{cases}
a_{q-m} = \dfrac{\lambda_{i,k-\frac{1}{2}}}{\Delta z^2} \\[3mm]
a_{q-1} = \dfrac{\lambda_{i-\frac{1}{2},k}}{\Delta x^2} \\[3mm]
a_q = \left(\dfrac{\lambda_{i-\frac{1}{2},k} + \lambda_{i+\frac{1}{2},k}}{\Delta x^2} + \dfrac{\lambda_{i,k-\frac{1}{2}} + \lambda_{i,k+\frac{1}{2}}}{\Delta z^2} \right) \\[3mm]
a_{q+1} = \dfrac{\lambda_{i+\frac{1}{2},k}}{\Delta x^2} \\[3mm]
a_{q+m} = \dfrac{\lambda_{i,k+\frac{1}{2}}}{\Delta z^2}
\end{cases}
\qquad (2.48)
$$

For each node q of the discretization, an equation like (2.47) can be written. By varying q from 1 to $m \cdot n$, five vectors, $\boldsymbol{a_{q-m}}$, $\boldsymbol{a_{q-1}}$, $\boldsymbol{a_q}$, $\boldsymbol{a_{q+1}}$ and $\boldsymbol{a_{q+m}}$, are obtained; the components of these vectors can be calculated using (2.48). As we will see in the next subchapter, these vectors have few elements equal to zero due to the boundary conditions. These vectors allow the creation of the matrix notation: $\boldsymbol{A}\,\boldsymbol{p} \;=\; \boldsymbol{f}$, where $\boldsymbol{A}$ is the matrix of coefficients and $\boldsymbol{f}$ is the vector of known terms.

$$
\begin{bmatrix}
* & *_{+1} & & & *_{+m} & & & & & & & \\
*_{-1} & * & *_{+1} & & & *_{+m} & & & & & & \\
 & *_{-1} & * & *_{+1} & & & *_{+m} & & & & & \\
 & & *_{-1} & * & *_{+1} & & & *_{+m} & & & & \\
*_{-m} & & & *_{-1} & * & *_{+1} & & & *_{+m} & & & \\
 & a_{q-m} & \cdots & \cdots & a_{q-1} & -a_q & a_{q+1} & \cdots & \cdots & a_{q+m} & & \\
 & & *_{-m} & & & *_{-1} & * & *_{+1} & & & *_{+m} & \\
 & & & *_{-m} & & & *_{-1} & * & *_{+1} & & & \\
 & & & & *_{-m} & & & *_{-1} & * & *_{+1} & & \\
 & & & & & *_{-m} & & & *_{-1} & * & *_{+1} & \\
 & & & & & & *_{-m} & & & *_{-1} & *
\end{bmatrix}
\begin{bmatrix}
p_{q-m} \\ \vdots \\ \vdots \\ p_{q-1} \\ p_q \\ p_{q+1} \\ \vdots \\ \vdots \\ p_{q+m}
\end{bmatrix}
=
\begin{bmatrix}
f_q
\end{bmatrix}
$$

$$(2.49)$$

Equation (2.49) shows how equation (2.47) allows the creation of the matrix system which can be easily resolved by a calculation program as MATLAB.

The coefficients matrix A in (2.49) presents asterisk elements marked with different subscript:

- $*$ represents the elements of the main diagonal, which are given by the vector $\boldsymbol{a_q}$ components;

- $*_{+1}$ represents the elements of the first super-diagonal, which are given by the vector $\boldsymbol{a_{q+1}}$ components;

- $*_{-1}$ represents the elements of the first sub-diagonal, which are given by the vector $\boldsymbol{a_{q-1}}$ components;

- $*_{+m}$ represents the elements of the m_{th} super-diagonal, which are given by the vector $\boldsymbol{a_{q+m}}$ components;

- $*_{-m}$ represents the elements of the m_{th} sub-diagonal, which are given by the vector $\boldsymbol{a_{q-m}}$ components.

General matrix diagonals can be specified by an index called t measured relatively to the main diagonal, thus:

$t = 0$ for the main diagonal;

$t = \pm 1$ for the first super-diagonal and the first sub-diagonal;

$t = \pm m$ for the m_{th} super-diagonal and m_{th} sub-diagonal.

The resulting matrix A is pentadiagonal, meaning that it has five diagonals, such that each of them have at least one element different from zero. Actually, as it will be discussed in the next subchapter, the number of elements equal to zero is much smaller than the number of elements different from zero.

2.2.3 Boundary conditions and weak internal nodes

For hydrodynamic lubrication, three sets of boundary conditions known as the Full-Sommerfeld, Half-Sommerfeld and Reynolds are widely quoted throughout the literature.

- Full-Sommerfeld boundary condition

The Full-Sommerfeld boundary condition [11] assumes that the pressure is equal to zero at the edges of the of the journal unwrapped surface:

$$p = 0 \qquad \text{at} \qquad \theta = 0 \text{ and } \theta = 2\pi \qquad\qquad (2.50)$$

This boundary condition is unlikely to apply to real fluids because it leads to a large negative pressure in the diverging region which is the mirror image of the pressure distribution in the converging region. Large negative pressures are physically unrealistic. Furthermore, because of these opposing negative and positive pressures, the predicted load capacity is zero. On the other hand, it has been shown that the hydrodynamic lubrication film is very efficient under such geometries and is capable of supporting a load. Hence some other boundary condition should be applied [3].

- Half-Sommerfeld or Gümbel boundary condition

To get closer to reality the previous boundary condition has been adapted to avoid negative pressures and to allow the generation of hydrodynamic forces. The Half-Sommerfeld or Gümbel boundary condition states:

$$
\begin{aligned}
p = 0 \qquad &\text{at} \qquad \theta = 0 \ \text{and} \ \theta = \pi \\
p = 0 \qquad &\text{at} \qquad \pi < \theta < 2\pi
\end{aligned}
\tag{2.51}
$$

This boundary condition is very easy to apply from an engineering point of view, but, however, its physical basis is erroneous since discontinuity of flow at the boundary between the zero and non-zero pressure regions is implied.

The flow rates per unit length, Q_x, can be found from integrating the lubricant velocity profile over the film thickness:

$$
Q_x = \int_0^h u \, dz
\tag{2.52}
$$

substituting u from equation (2.12), yields:

$$
Q_x = \frac{h^3}{12\mu} \frac{\partial p}{\partial x} + \frac{h}{2} U
\tag{2.53}
$$

As shown in Figure 2.14, between 0 and π there is a value of θ such that $\partial p / \partial x = 0$ (pressure maximum point). By applying the continuity between this angular position, where the film thickness is called $\overline{h}$, and $\theta = \pi$, equation (2.53) yields:

$$
\frac{\overline{h}}{2} U \neq \frac{h_{min}}{2} U
\tag{2.54}
$$

because $\overline{h}$ is for sure bigger than h_{min}.

Summarizing, both conditions analysed so far are not physically realistic, since one leads to predictions of large negative pressures and the other to a discontinuity of flow.

- Reynolds boundary condition

The solution to this problem comes again from Reynolds, who stated that there is no negative pressure zone and, that, at the boundary between zero and non-zero pressure the pressure variation is also zero.

$$p = 0 \qquad \text{at} \qquad \theta = 0$$
$$p = \frac{\partial p}{\partial x} = 0 \qquad \text{at} \qquad \theta = \theta_{cav} \tag{2.55}$$

where:

θ_{cav} represents the angular position where the cavitation phenomenon begins.

In fact, in the diverging region ($\theta > \pi$) the lubricating film starts to divide into streamers of lubricant and air spaces (Figure 2.13). As the film thickness continues to increase, the proportion of space occupied by lubricant streamers is correspondingly reduced. The balance between streamer volume and volume of air space is determined by the condition that the lubricant flow remains constant within the zero-pressure region [3].
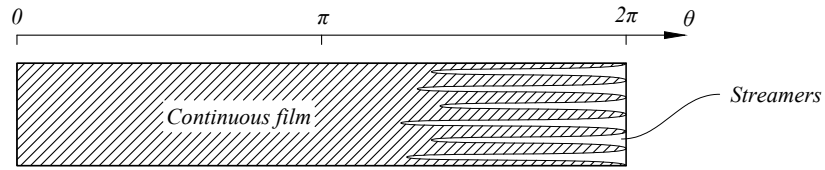

Figure 2.13: Cavitation effect [3].
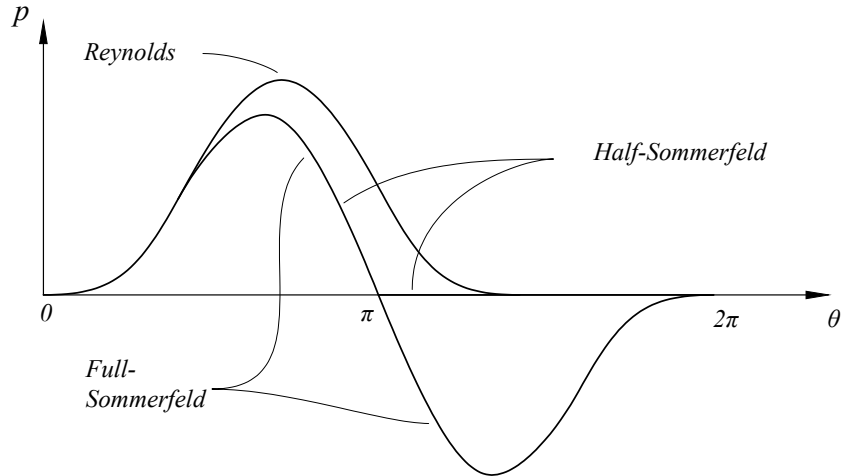
Figure 2.14: Comparation among Full-Sommerfeld, Half-Sommerfeld and Reynolds boundary conditions [12].

The three boundary conditions just explained set a pressure value over the boundaries which are parallel with the 'z'-axis. In order to resolve the Reynolds equation on the journal surface, boundary conditions are also required for the two 'x'-axis parallel boundaries (see Figure 2.15).

In conclusion, the boundary conditions that must be applied during computation have been chosen considering the following assumptions:

- Reynolds condition must be applied at the cavitation boundary, that is, at:

$$\theta = \theta_{cav} = \pi + \alpha(z) \tag{2.56}$$

Two facts should be noted about the location of the cavitation boundary; the first one is that it is a function of z, which means that this boundary does not lie along a line of constant θ, and second, $\alpha(z)$ is not known a priori and should be calculated as the solution of the pressure field [13]. Furthermore, the resolution of the pressure field using this condition requires an iterative procedure. For this reason and for the fact that the dependency of θ_{cav} from z is incompatible with the fixed discretisation step used in this work, it has been chosen not to use Reynolds condition;

- each edge of the journal, along the 'x' direction, can be assumed in contact with the external environment.

A shown in Figure 2.15, the boundary conditions applied are:

$$
\begin{aligned}
p = p_{atm} = 0 &\qquad \text{at} \qquad z = 0 \text{ and } z = L \\
p = 0 &\qquad \text{at} \qquad x = 0 \text{ and } x = 2\pi R_j
\end{aligned} \tag{2.57}
$$
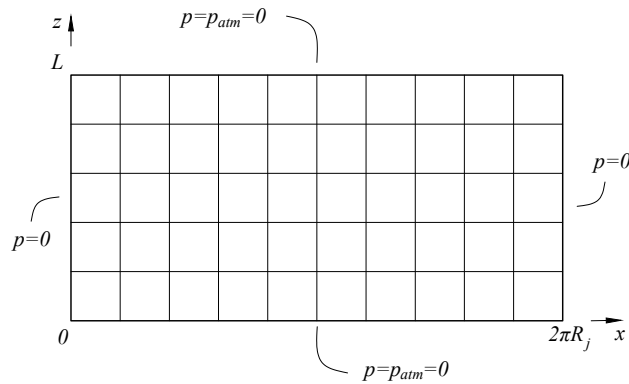
Figure 2.15: Boundary condition over the journal surface.

44

Equation (2.51) shows that Full-Sommerfeld boundary condition is used for the determination of the pressure distribution; however, for those internal nodes which present negative pressure once the Reynolds equation is solved, a null pressure value is forced. By doing so, Half-Sommerfeld condition is applied.

It's important to notice that the way the angular coordinate θ, and consequently the coordinate x, have been chosen, combined with the boundary condition used, leads to an error in the pressure distribution which occurs under certain operative conditions of the journal.

Let's take under consideration the journal bearing configuration shown in Figure 2.16 (left), where the journal radial velocity is negative, i.e. when the vector goes from O_j to O_b.
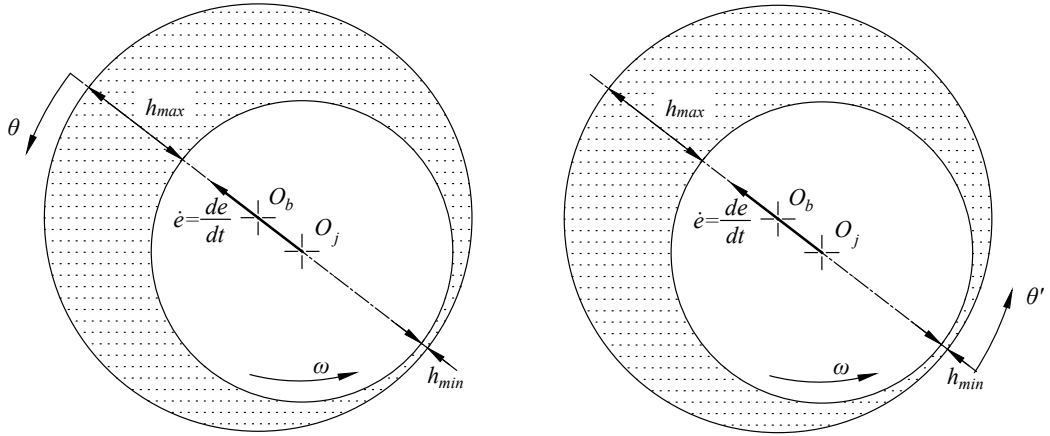
Figure 2.16: Journal bearing configuration when $\dot{e} < 0$.

Recalling that the hydrodynamic pressure is due to the wedge and the squeezing effects and that the coordinate θ (or x) is defined starting from the centre line in correspondence of the maximum film thickness, when $\dot{e}$ is negative, the movement of the journal would generate a positive pressure field, due to the squeeze action, around $\theta = 0$. Since the boundary condition previously defined force $p = 0$ at this point, the squeeze effect on the pressure distribution, in such work condition, is heavily altered as shown in Figure 2.19 (up).

The solution to this problem simply consists of changing the way the angular coordinate is defined. Since the Full-Sommerfeld boundary condition requires $p = 0$ both at $\theta = 0$ and $\theta = 2\pi$, it's possible to rotate θ by 180° and make it start in correspondence of the minimum film thickness (Figure 2.16 right). The new angular coordinate it's called θ'.

By doing so the correct pressure distribution is preserved (Figure 2.19 down).

45

The new definition of the angular coordinate leads to the variation of few parameters needed by the Reynolds equation.
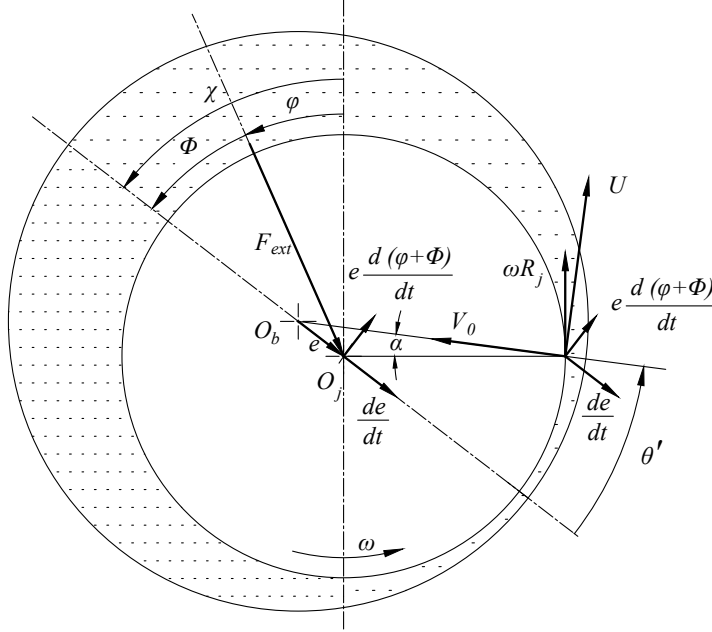
Figure 2.17:   Cross section of a journal bearing: velocity components in the new reference system.

By analysing Figure 2.17, with the same procedure explained earlier, we can say that:

$$h = C - e \, cos\theta' = C(1 - \varepsilon \, cos\theta') \qquad (2.58)$$

and

$$\begin{cases} U = \omega R_j - C\dfrac{d\varepsilon}{dt} \, sin\theta' + C\varepsilon \dfrac{d(\varphi + \Phi)}{dt} \, cos\theta' \\[4mm] V_0 = +\omega R_j \, \alpha - C\dfrac{d\varepsilon}{dt} \, cos\theta' - C\varepsilon \dfrac{d(\varphi + \Phi)}{dt} \, sin\theta' \end{cases} \qquad (2.59)$$

By substituting equations (2.58) and (2.59) into (2.21), Reynolds equation becomes:

$$\frac{\partial}{\partial x}\left(\frac{h^3}{\mu}\frac{\partial p}{\partial x}\right) + \frac{\partial}{\partial z}\left(\frac{h^3}{\mu}\frac{\partial p}{\partial z}\right) = 6\left(\left(\omega - 2\frac{d\varphi}{dt} - 2\frac{d\Phi}{dt}\right)\frac{dh}{d\theta'} - 2C\frac{d\varepsilon}{dt}cos\theta'\right) \qquad (2.60)$$

Comparing (2.35) with (2.60), the only two things that change are how the film thickness is function of θ' and the minus sign that characterizes the last term in the previous equation. Thus, the discretization with finite difference of (2.60) is made with the exact same treatment we saw earlier for equation (2.35). The only care to be taken is the adjustment of the know term f in the matrix notation $A\,p\,=\,f$.

To standardize the results, when the pressure distribution has been found, it's better to go back to a condition where the angular coordinate starts from the maximum film thickness (Figure 2.16 left). Once the Reynolds equation is solved and each node of the discretization is associated to a pressure value, a simple readjustment of the pressure matrix is needed, as shown in Figure 2.18:
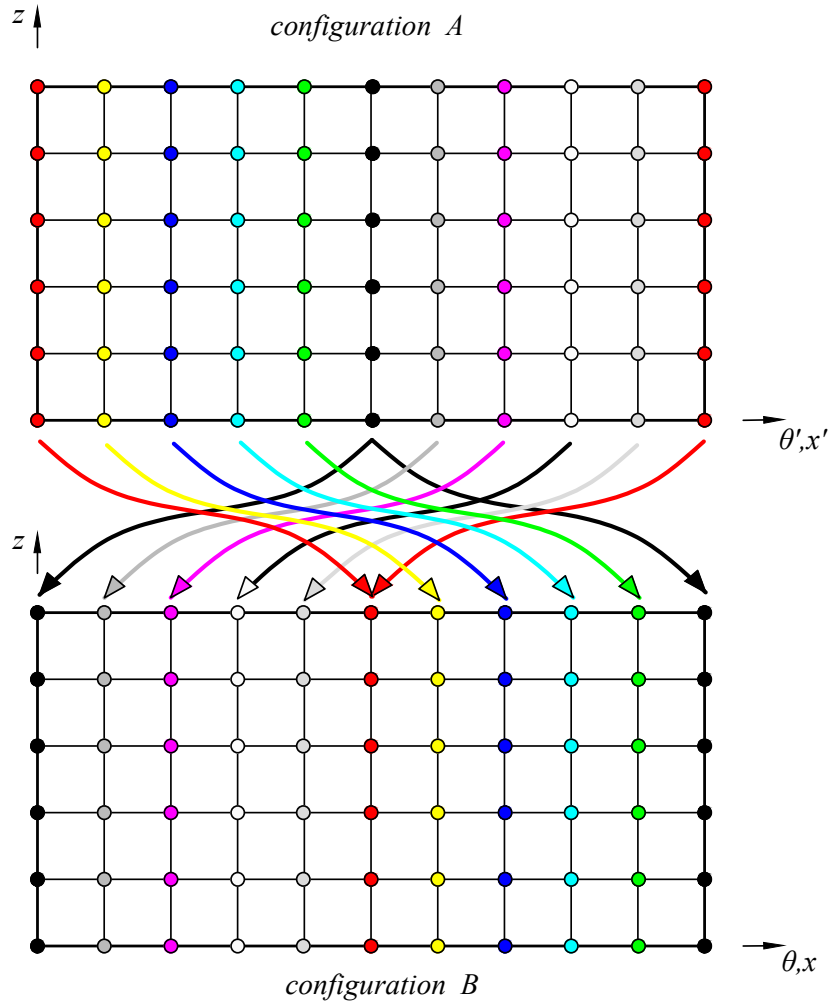

Figure 2.18:   Pressure matrix readjustment.

47

The matrix readjustment is executed by moving the pressure values by columns along the 'x'-axis; in the 'z' direction, no variations have to be done.

In Figure 2.18, the coloured dots represent the pressure values over the nodes of the journal grid. The figure is divided in:

- *configuration A*, where the angular coordinate is θ'; it's the result of the Reynolds equation (2.60) integration;

- *configuration B*, where the angular coordinate is θ; it's the outcome of the matrix readjustment.

Since the angular phase shift between θ' and θ is 180°:

$$\theta' = \theta + \pi \qquad \text{and, hence,} \qquad x' = x + \pi R_j \tag{2.61}$$

the first column (red dots) of the pressure distribution in the *configuration A* must be translated, without any variation, in the central column of the grid in the *configuration B*; the second column (yellow dots) in *configuration A* is moved over the first column on the right side with respect to the central one in *configuration B*. By proceeding in this way, the next columns (blue, cyan and green dots) are easily moved. When we reach the central column in *configuration A* (black dots), it means that θ' has reached the angular value where the angular coordinate θ is equal to zero. Thus, this column needs to be moved over the first column in *configuration B*. Again, using the same method, the dark grey, magenta, white and light grey dots columns can be readjusted.

Since the journal grid in Figure 2.18 is the planar representation of the cylindrical surface of the journal:

- the vertical boundaries, in *configuration A*, are actually overlapping in the wrapped configuration. For this reason, the pressure dots present the same red colour and, that's why, the first and the last columns in *configuration A* converge in the central position in *configuration B;*

- the central column in *configuration A* is doubled to create the first and the last column in *configuration B.*

In Figure 2.19 is shown the pressure distribution obtained with the integration of Reynolds equation for a journal bearing with the geometric and dynamic data exposed in Table 2.3.

48
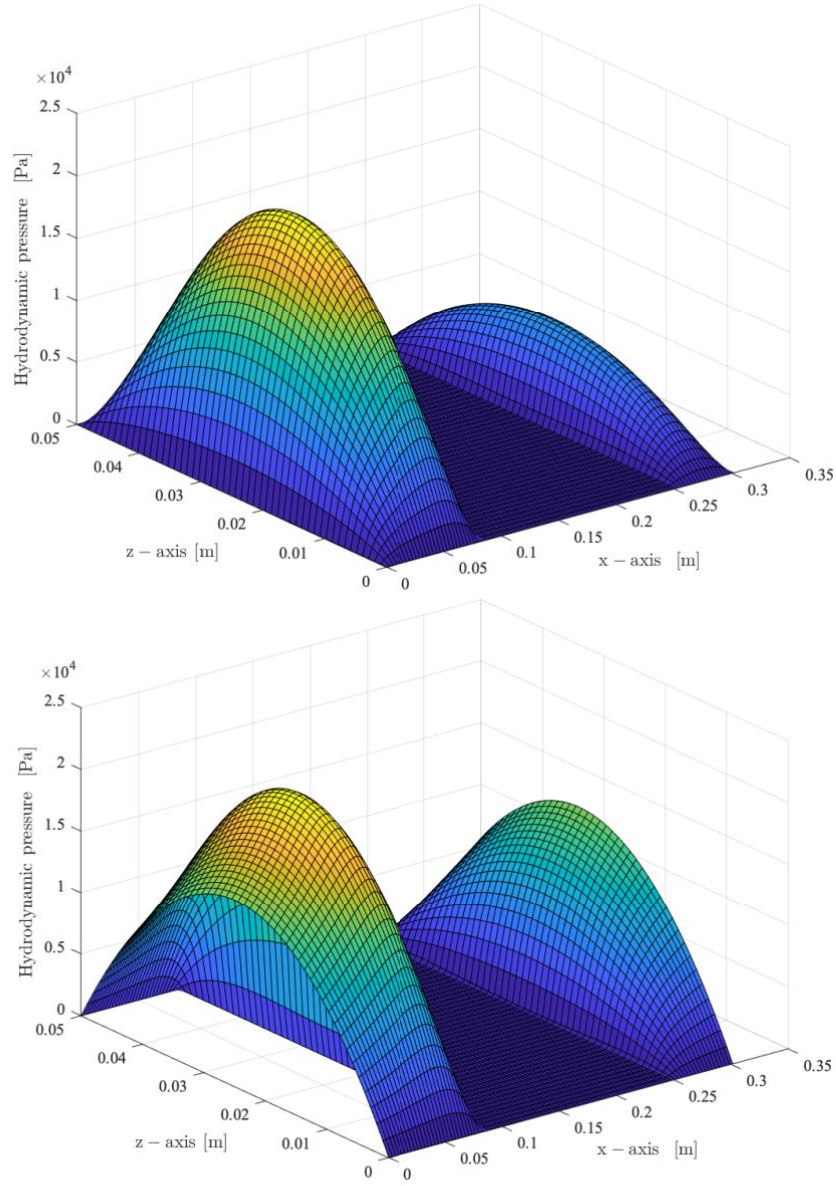
Figure 2.19: Up: pressure distribution using angular coordinate θ. Down: pressure distribution using angular coordinate θ' and matrix readjustment.

By comparing the two images, we can see how the squeezing effect due to the negative journal radial velocity affects the pressure distribution around $\theta = 0$.

Indeed, for $x = 0$, the maximum pressure value, which is obtained for both cases at $L/2$ along the 'z'-axis, is 0 Pa if the previous procedure is not applied (Figure 2.19 up), whilst is equal to $1.51 \cdot 10^4$ Pa if the auxiliary angular coordinate θ' and matrix readjustment are used (Figure 2.19 down).

Data	Symbol, unit of measurement	Value
Journal bearing length	L, [m]	0.05
Bearing radius	R_b, [m]	0.05
Journal radius	R_j, [m]	0.048
Journal angular speed	ω, [rad/s]	50
Eccentricity, journal radial position	e, [m]	0.0015
Journal radial velocity	$\dot{e}$, [m/s]	-0.1
Journal angular velocity	$\dot{\chi} = \dot{\varphi} + \dot{\Phi}$, [rad/s]	0
Viscosity	μ, [Pas]	1.74

Table 2.3: Journal bearing geometric and dynamic data for the determination of pressure distribution with $\dot{e} < 0$.

The implementation of Dirichlet boundary condition in the finite difference method does not only affect the pressure value for the nodes of the discretization that actually belong to the boundary of the surface, but it also has an impact on those internal nodes which are located in the proximity of the boundaries.

This can be explained with a couple of examples. Let's take under consideration the internal node defined by $i = 1$ and $k = 1$, using the two indices numbering, or $q = 1$, using the single index numbering; by referring to Figure 2.10, this node lies in the bottom left corner of the discretization. The computational molecule related to this node is shown is Figure 2.20.
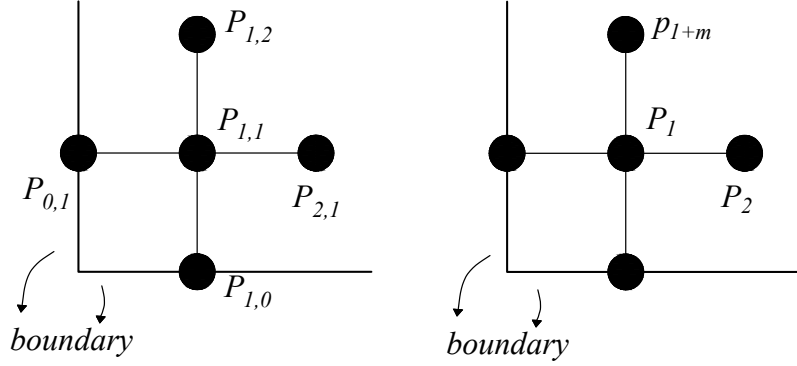
Figure 2.20: Computational molecule for bottom left corner internal node; two indices numbering (on the left), single index numbering (on the right).

Equation (2.45) for the node in consideration becomes:

$$\frac{\lambda_{1,\frac{1}{2}}}{\Delta z^2}\, p_{1,0} + \frac{\lambda_{\frac{1}{2},1}}{\Delta x^2}\, p_{0,1} - \left(\frac{\lambda_{\frac{1}{2},1} + \lambda_{\frac{3}{2},1}}{\Delta x^2} + \frac{\lambda_{1,\frac{1}{2}} + \lambda_{1,\frac{3}{2}}}{\Delta z^2}\right) p_{1,1} +$$
$$+ \frac{\lambda_{\frac{3}{2},1}}{\Delta x^2}\, p_{2,1} + \frac{\lambda_{1,\frac{3}{2}}}{\Delta z^2}\, p_{1,2} \cong f_{1,1} \tag{2.62}$$

Since the boundary condition imposes zero pressure for the nodes which lie on the boundary, $p_{1,0}$ (south node pressure) and $p_{0,1}$ (west node pressure) are equal to zero. Thus,

$$-\left(\frac{\lambda_{\frac{1}{2},1} + \lambda_{\frac{3}{2},1}}{\Delta x^2} + \frac{\lambda_{1,\frac{1}{2}} + \lambda_{1,\frac{3}{2}}}{\Delta z^2}\right) p_{1,1} + \frac{\lambda_{\frac{3}{2},1}}{\Delta x^2}\, p_{2,1} + \frac{\lambda_{1,\frac{3}{2}}}{\Delta z^2}\, p_{1,2} \cong f_{1,1} \tag{2.63}$$

or, using the single index equation (2.47):

$$-a_1\, p_1 + a_2\, p_2 + a_{1+m}\, p_{1+m} = f_1 \tag{2.64}$$

Comparing equation (2.47) with (2.64) we can see how the first and the second terms disappear.

The same procedure applied for the internal node with indices $i = 2$ and $k = 1$ (or $q = 2$), leads to a computational molecule where the south node has a pressure equal to zero ($p_{2,0} = 0$). Therefore, equation (2.47) becomes:

$$a_1 \, p_1 - a_2 \, p_2 + a_3 \, p_3 + a_{2+m} \, p_{2+m} = f_2 \qquad (2.65)$$

For this node, the comparison between equation (2.47) and (2.65) shows that only the first term disappears.

Those two examples allow us to distinguish between strong and weak inner nodes:

- strong inner nodes are characterised by the fact that their computational molecule is entirely made of inner nodes. The indices i, k of strong inner nodes thus satisfy:

$$\begin{cases} 2 \leq i \leq m - 1 \\ 2 \leq k \leq n - 1 \end{cases} \qquad (2.66)$$

- on the other hand, the molecule of weak inner nodes includes one or two boundary nodes; this happens when i is equal to 1 or m, and/or k is equal to 1 or n.

Equation (2.47), relative to a strong inner node, has exactly 5 pressure unknowns, whereas the equation of a weak inner node contains a lesser number of unknowns (3 or 4).

In Table 2.4 weak inner nodes are taken under investigation and grouped according to the elements of equation (2.47) that disappear. In the first column of the table is specified which node or group of nodes is considered; to better understand their location, a schematic representation of the grid is shown in the second column. In the third column, equation (2.47) is written for such node/nodes by removing the elements that disappear due to their location, which are specified in column four. Lastly, in column five the number of pressure unknowns associated to the computational molecule of the node are indicated.
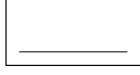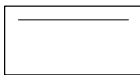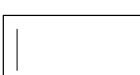
Node/nodes numbering	Schematic representation	Equation (2.47)	Missing elements	N. unk.
$i = 1$ and $k = 1$ or $q = 1$		$-a_1\, p_1 + a_2\, p_2 + a_{1+m}\, p_{1+m} = f_1$	first and second	3
$2 \leq i \leq m - 1$ and $k = 1$ or $2 \leq q \leq m - 1$		$a_{q-1}\, p_{q-1} - a_q\, p_q + a_{q+1}\, p_{q+1} +$ $+ a_{q+m}\, p_{q+m} = f_q$	first	4
$i = m$ and $k = 1$ or $q = m$		$a_{m-1}\, p_{m-1} - a_m\, p_m + a_{2m}\, p_{2m} =$ $= f_m$	first and fourth	3
$i = m$ and $2 \leq k \leq n - 1$ or $q = (k-1)m + m$		$a_{q-m}\, p_{q-m} + a_{q-1}\, p_{q-1} - a_q\, p_q +$ $+ a_{q+m}\, p_{q+m} = f_q$	fourth	4
$i = m$ and $k = n$ or $q = (n-1)m + m$		$a_{q-m}\, p_{q-m} + a_{q-1}\, p_{q-1} - a_q\, p_q =$ f_q	fourth and fifth	3
$2 \leq i \leq m - 1$ and $k = n$ or $q = (n-1)m + i$		$a_{q-m}\, p_{q-m} + a_{q-1}\, p_{q-1} - a_q\, p_q +$ $+ a_{q+1}\, p_{q+1} = f_q$	fifth	4
$i = 1$ and $k = n$ or $q = (n-1)m + 1$		$a_{q-m}\, p_{q-m} - a_q\, p_q + a_{q+1}\, p_{q+1} =$ $= f_q$	second and fifth	3
$i = 1$ and $2 \leq k \leq n - 1$ or $q = (k-1)m + 1$		$a_{q-m}\, p_{q-m} - a_q\, p_q + a_{q+1}\, p_{q+1} +$ $+ a_{q+m}\, p_{q+m} = f_q$	second	4

Table 2.4: Analysis of weak inner nodes.

Table 2.4 allows to make final considerations about vectors $\boldsymbol{a_{q-m}}, \boldsymbol{a_{q-1}}, \boldsymbol{a_q}, \boldsymbol{a_{q+1}}$ and $\boldsymbol{a_{q+m}}$, presented in the previous subchapter. Those vectors, whose components are obtainable using equation (2.48), create the coefficients matrix A by arranging them on certain diagonals, as visible in equation (2.49).

As summarized in Table 2.4, the presence of weak inner nodes causes the disappear of certain components in vectors $\boldsymbol{a_{q-m}}$, $\boldsymbol{a_{q-1}}$, $\boldsymbol{a_q}$, $\boldsymbol{a_{q+1}}$ and $\boldsymbol{a_{q+m}}$ leading to a matrix of coefficients A that for $m = 7$ and $n = 4$ has the structure shown in Figure 2.21.
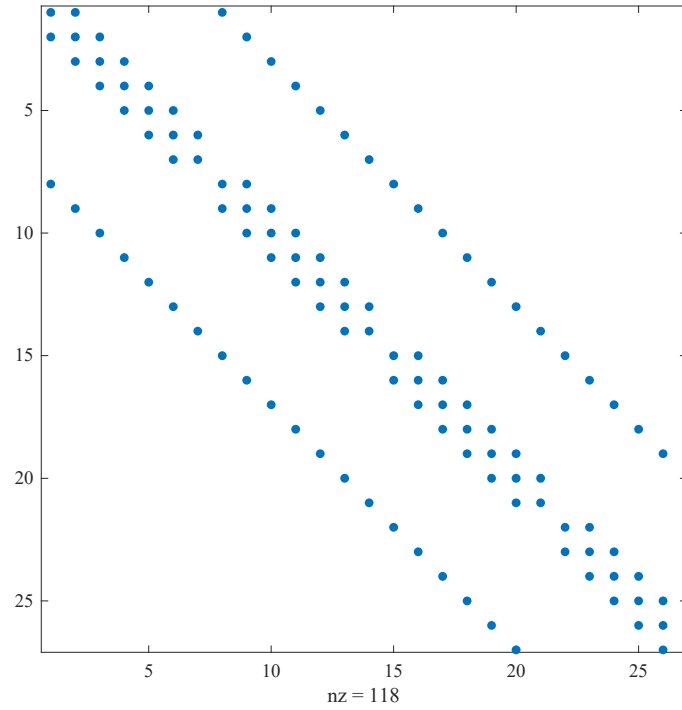
Figure 2.21:   Structure of the matrix A when $m = 7$ and $n = 4$. Thick dots denote the position of non-zero entries.

The Reynolds equation has been integrated following the procedure explained in this chapter by writing a code in MATLAB which is visible Appendix B. Since the goal is the determination of the pressure distribution at each time step, the Reynolds equation needs to be implemented into Simulink environment. To do so, the MATLAB code has been written into a user-defined Matlab function block in Simulink called "Reynold equation solver" (see Figure 2.27).

2.3 Lubricant viscosity

Experimental evidence has shown that viscosity varies, other than with temperature, also with pressure [3]. With increasing temperature, the viscosity of oils falls quite rapidly meanwhile lubricant viscosity increases with pressure.

There are several viscosity-temperature equations available in literature: Reynolds, Slotte, Walther, Vogel, etc [14]; the most accurate is the Vogel equation:

$$\mu = a \, e^{b/(T-c)} \tag{2.67}$$

where:

a, b, c are oil characteristic parameters; (Pas), (K), (K) respectively;
T is the absolute temperature **(K)**;
μ is the dynamic viscosity at temperature T (Pas).

The best correlation between viscosity and pressure is given by the Barus equation [15]:

$$\mu = \mu_0 \, e^{\alpha \, p} \tag{2.68}$$

where:

μ_0 is the atmospheric viscosity (Pas);
α is the pressure-viscosity coefficient (m²/N);
p is pressure of concern (Pa);
μ is the dynamic viscosity at pressure p (Pas).

The lubricant, that divides the journal from the bearing into the rod-end, is subjected both to temperature changes, due to the external climate circumstances, and to pressure variations, due to the dynamic work conditions. Thus, combining (2.67) and (2.68), the Vogel-Barus model is obtained:

$$\mu = a \, e^{b/(T-c)} \, e^{\alpha \, p} \tag{2.69}$$

In equation (2.69) the pressure-independent viscosity term μ_0 is only function of temperature according to the Vogel equation.

The use of Vogel-Barus equation is possible only knowing the value of the three constants a, b, c, the pressure viscosity coefficient α and the pressure of the lubricant:

- the relation between the pressure and the viscosity creates a computational problem due to the fact that the Reynolds equation needs as input the lubricant viscosity, which is function of temperature and pressure, but the pressure is given by the resolution of the Reynolds equation itself; we are dealing with an algebraic loop. Algebraic loops occur when an input port with direct feedthrough is driven by the output of the same block. Simulink provides algebraic loop solvers that attempt to resolve the situation iteratively. Since the solution of algebraic loop extends the simulation time considerably, it's been decided to break the loop using a memory block, which holds and delays its input by one integration time step. By doing so, at each time step, Reynolds equation is solved using the viscosity obtained through (2.69), where the pressure p is calculated by an arithmetic mean of the previous time step pressure distribution, as express in (2.70):

$$p = \frac{p_{max_{t-1}} + p_{min_{t-1}}}{2} \tag{2.70}$$

where:

$p_{max_{t-1}}$ is the maximum value of the pressure distribution at the previous time step (Pa);

$p_{min_{t-1}}$ is the minimum value of the pressure distribution at the previous time step (Pa).

This solution implies errors respect to the iterative method because the pressure distribution at the previous time step could be different from the one active at the present time step especially when the journal is in an off-balance dynamic condition; however, the need to perform long flight simulation makes this solution preferable;

- there are various formulae available to calculate the pressure-viscosity coefficient. One of the early ones was derived by Wooster [15]:

$$\alpha = (0.6 + 0.965 \, log_{10}\mu_0) \, 10^{-8} \tag{2.71}$$

where:

$\mu_0 = a \, e^{b/(T-c)}$ is the atmospheric viscosity (Pas);

- the characteristic parameters a, b, c can be determined using three viscosity measurements at different temperatures for a specific oil. In aviation, the outside air temperature refers to the temperature of air around an aircraft, and for a cruising altitude of 12'000 m it can reach -54°C [16]. Since the actuator hydraulic fluid works between 40°C and 70°C in regime conditions, the servo-actuator chambers will tend to be at higher temperature than outside. Thus, the minimum temperature considered for the rod-end lubricant has been set at -40°C. The lubricant considered in this work is SAE 0W/30, where the suffix W stands for winter. The oils of this category are able to maintain low viscosity for cold temperatures, as visible in Figure 2.22.
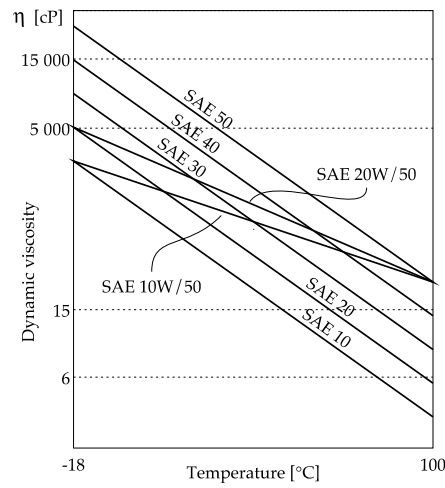

Figure 2.22:   Viscosity-temperature graph for some monograde and multigrade oils [3].

The three viscosity values needed for the calculation of the characteristic parameters are available on the data sheet of the lubricant manufacturers (Table 2.5):

SAE 0W/30	
Temperature (°C)	Dynamic viscosity (Pas)
-40	6.5
0	0.47
100	0.009

Table 2.5:   Dynamic viscosity at different temperature for SAE 0W/30.

Stachowiak and Batchelor developed, in their work [3], several MATLAB codes to help the reader to find solutions of tribological problems. Among them, the program "Viscosity" provides the solution to the Vogel equation and calculates the viscosity at any given temperature. This code has been elaborated and adapted to this work to obtain the Vogel characteristic parameters for SAE 0W/30 oil:

$$\begin{cases} a = 4.212 \cdot 10^{-7} \ Pas \\ b = 3.510 \cdot 10^{3} \qquad K \\ c = 21.10 \qquad\qquad K \end{cases} \qquad (2.72)$$

The viscosity-temperature dependency is shown in Figure 2.23:
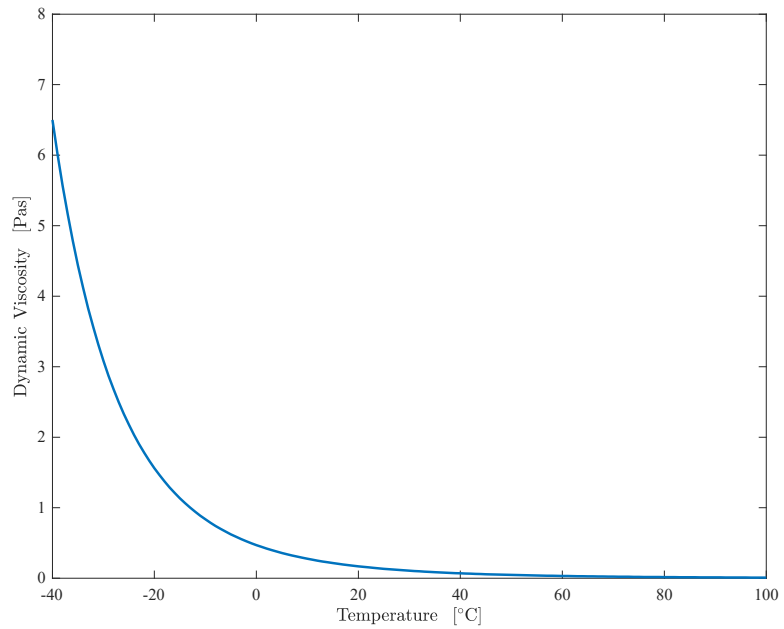
Figure 2.23: Dynamic viscosity vs. temperature for SAE 0W/30 oil.

For more information about the Vogel equation code refer to [3].

2.4   Hydrodynamic forces

The integration of the pressure distribution around the journal allows the determination of hydrodynamic force and, thus, the total load that the journal bearing will support under hydrodynamic conditions.

The hydrodynamic force is usually calculated from two components, one acting along the line of journal and bearing centres (F_r) and a second component perpendicular to the first (F_t), as shown in Figure 2.24:
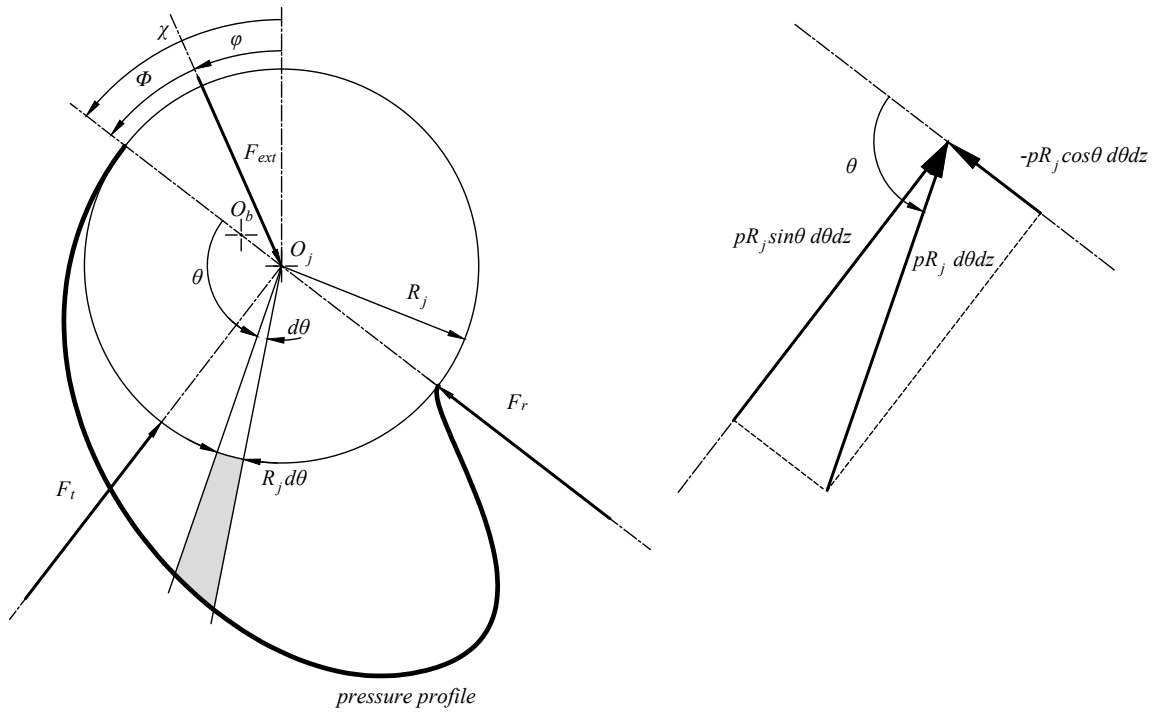

Figure 2.24:   Hydrodynamic load components and pressure field acting on the journal.

To analyse and derive expressions for the load components F_r and F_t, consider a small element of area $R_j d\theta dz$, where the 'z'-axis is normal to the plane of representation of Figure 2.24 (the reference system used is specified in Figure 2.5).

The pressure acting on the infinitesimal element is highlighted in grey in the previous figure. The force exerted by the hydrodynamic pressure on the element is $pR_j d\theta dz$ and this force is divided into two components as visible on the right side of Figure 2.24:

- $-pR_j cos\theta \ d\theta dz$ acting along the line of shaft and bush centres;

- $pR_j sin\theta \ d\theta dz$ acting in the direction normal to the line of centres.

The integration of these two components, over the entire journal surface, leads to the hydrodynamic forces:

$$\begin{cases} F_r = \int_0^{2\pi} \int_0^L -pR_j cos\theta \ dzd\theta \\ F_t = \int_0^{2\pi} \int_0^L pR_j sin\theta \ dzd\theta \end{cases} \tag{2.73}$$

or, remembering that $x = R_j \ \theta$,

$$\begin{cases} F_r = \int_0^{2\pi R_j} \int_0^L -pR_j cos\theta \ dzdx \\ F_t = \int_0^{2\pi R_j} \int_0^L pR_j sin\theta \ dzdx \end{cases} \tag{2.74}$$

The pressure p is not known as a mathematical expression whose primitive function is obtainable, thus a numerical integration is needed to solve equations (2.74).
The most common numerical integration methods are interpolatory, and they can be derived from this strategy [17]:

1. interpolate the function that has to be integrated by a polynomial of low degree (which is easy to integrate);

2. approximate the starting integral with the exact integral of the polynomial.

The degree of the interpolating polynomial defines the numerical integration method used:

- polynomial of degree 0: midpoint or rectangular rule;

- polynomial of degree 1: trapezoidal rule;

- polynomial of degree 2: Simpson's rule.

Since the pressure profile is unknown between adjacent nodes of the discretization, the best and easiest way to link the pressures between two nearby nodes is with a straight line (polynomial of degree 1). Therefore, the trapezoidal rule has been used to solve equations (2.74).

The general form of the trapezoidal rule is:

$$\int_a^b f(x)dx \approx (b-a)\left(\frac{f(a)+f(b)}{2}\right) \tag{2.75}$$

Considering the computational molecule for a node with generic indices i,j (Figure 2.10), the following graphs can be obtained:
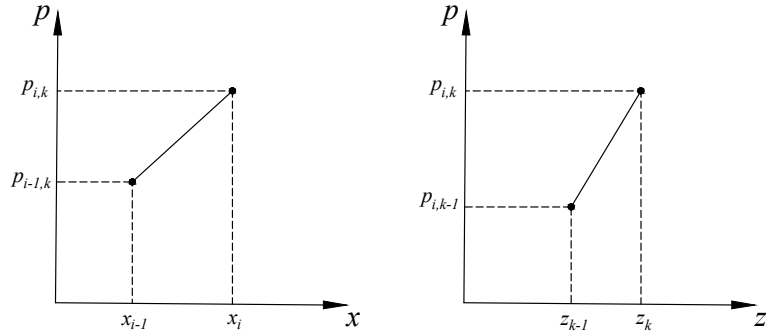

Figure 2.25: Pressure profile between two nearby nodes for trapezoidal rule integration.

Both equations (2.74) can be written in a more general form as:

$$F = \int_0^{2\pi R_j}\left(\int_0^L g(x,z)\,dz\right)dx \tag{2.76}$$

where:

$g(x,z) = -pR_j cos\theta$ for the component F_r;

$g(x,z) = pR_j sin\theta$ for the component F_t.

Equation (2.76) is a double integral along 'x' and 'z' directions. The inner integral is approximated by a one-dimensional quadrature rule where x is held fixed. The values obtained are then used to approximate the outer integral, also by a one-dimensional rule (2.75).

$$G(x) = \int_0^L g(x,z)dz = \frac{\Delta z}{2} \sum_{k=1}^{n+1} \big(g(x,z_{k-1}) + g(x,z_k)\big) \qquad (2.77)$$

and thus:

$$F = \int_0^{2\pi R_j} G(x)dx = \frac{\Delta x}{2} \sum_{i=1}^{m+1} \big(G(x_{i-1}) + G(x)\big) \qquad (2.78)$$

Substituting (2.77) into (2.78), the definitive equation for the double numerical integration with the trapezoidal rule is obtained:

$$F = \frac{\Delta x}{2} \frac{\Delta z}{2} \sum_{i=1}^{m+1} \left(\sum_{k=1}^{n+1} \big(+g(x_{i-1},z_{k-1}) + g(x_{i-1},z_k) + g(x_i,z_{k-1}) + g(x_i,z_k)\big) \right) \qquad (2.79)$$

By substituting correctly $g(x,z)$, as reported in (2.76), equation (2.79) allows the calculation of the hydrodynamic components. The total hydrodynamic force is the resultant of F_r and F_t:

$$F_{hydro} = \sqrt{F_r^2 + F_t^2} \qquad (2.80)$$

The direction of this force respect to the line of centres can be determined directly from the hydrodynamic components:

$$\Phi_{hydro} = atan\left(\frac{F_t}{F_r}\right) \qquad (2.81)$$

Φ_{hydro} represents the attitude angle with respect to F_{hydro}, and it's been called in this way in relation with Φ which is the angle between the external force and the line of centres (Figure 2.8). Obviously Φ and Φ_{hydro} are equal when the journal is equilibrium conditions as well as F_{ext} and F_{hydro}.

There is another force that occurs when the journal is moving inside the lubricant, we are taking about the friction force. The friction force can be calculated by integrating the shear stress 'τ' over the bearing area. Using equation (2.7):

$$F_{frict} = \int_0^{2\pi R_j} \int_0^L \tau \, dzdx = \int_0^{2\pi R_j} \int_0^L \mu \frac{du}{dy} \, dzdx \qquad (2.82)$$

Deriving equation (2.12), where the bearing is stationary, whereas the journal is moving, equation (2.82) can be rewritten as:

$$F_{frict} = \int_0^{2\pi R_j} \int_0^L \left(\left(y - \frac{h}{2} \right) \frac{dp}{dx} + \frac{\mu U}{h} \right) dzdx \qquad (2.83)$$

Equation (2.83) is integrated with the exact same numerical procedure previously exposed. It should be noted that the pressure derivative, in (2.83), has been approximated with a backward difference quotient, and y has been set equal to h since we are interested in the calculation of the friction force at the journal surface.

2.5   Journal dynamic

The motion of the journal with respect to the bearing centre can be obtained by analysing the free body diagram shown in Figure 2.26:
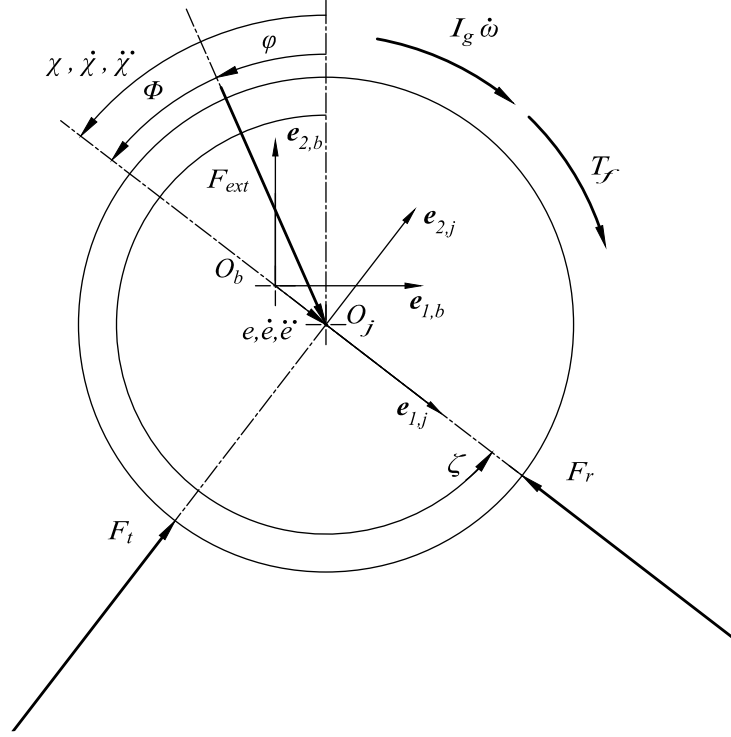

Figure 2.26:   Journal free body diagram in hydrodynamic conditions.

In Figure 2.26, $T_f = F_{frict} R_j$ represents the torque generated by the friction force due to the movement of the journal into the lubricant. The inertia force $m\ddot{e}$ has not been included because the direction of the journal acceleration is unknown a priori. Two reference systems are fixed in order to express the balance of forces:

- the first one, characterized by unit vectors $e_{1,b}$ and $e_{2,b}$, has its origin coincident with O_b;

- the second one, characterized by unit vectors $e_{1,j}$ and $e_{2,j}$, has its origin coincident with O_j.

64

To describe the journal motion is important to express the journal reference system respect to the bearing reference system, thus the relative rotation matrix is:

$$\begin{bmatrix} -\sin\zeta & \cos\zeta \\ -\cos\zeta & -\sin\zeta \end{bmatrix} \tag{2.84}$$

where:

$\zeta = \chi + \pi = \varphi + \Phi + \pi$ is the angle between $\boldsymbol{e}_{1,b}$ and $\boldsymbol{e}_{1,j}$ (rad).

Therefore, the multiplication between (2.84) and the column vector $[\boldsymbol{e}_{1,b} \ \ \boldsymbol{e}_{2,b}]$ leads to:

$$\begin{cases} \boldsymbol{e}_{1,j} = -\sin\zeta \, \boldsymbol{e}_{1,b} + \cos\zeta \, \boldsymbol{e}_{2,b} \\ \boldsymbol{e}_{2,j} = -\cos\zeta \, \boldsymbol{e}_{1,b} - \sin\zeta \, \boldsymbol{e}_{2,b} \end{cases} \tag{2.85}$$

and, for derivation:

$$\begin{cases} \dot{\boldsymbol{e}}_{1,j} = -\dot\zeta \cos\zeta \, \boldsymbol{e}_{1,b} - \dot\zeta \sin\zeta \, \boldsymbol{e}_{2,b} = \dot\zeta \, \boldsymbol{e}_{2,j} \\ \dot{\boldsymbol{e}}_{2,j} = +\dot\zeta \sin\zeta \, \boldsymbol{e}_{1,b} - \dot\zeta \cos\zeta \, \boldsymbol{e}_{2,b} = -\dot\zeta \boldsymbol{e}_{1,j} \end{cases} \tag{2.86}$$

Equations (2.85) and (2.86) allow the determination of radial position of the journal (eccentricity) $\boldsymbol{e}$, and its derivatives:

$$\begin{cases} \boldsymbol{e} = e \, \boldsymbol{e}_{1,j} \\ \dot{\boldsymbol{e}} = \dot{e} \, \boldsymbol{e}_{1,j} + e\dot\zeta \, \boldsymbol{e}_{2,j} \\ \ddot{\boldsymbol{e}} = \left(\ddot{e} - e\dot\zeta^2\right) \boldsymbol{e}_{1,j} + \left(e\ddot\zeta + 2\dot{e}\dot\zeta\right) \boldsymbol{e}_{2,j} \end{cases} \tag{2.87}$$

where the second and third terms of the last equation of (2.87) compose the drag acceleration, while the first term is the Coriolis acceleration and the fourth term is the relative acceleration of the journal with respect to the bearing. The last equation of (2.87) gives the components of the journal acceleration along $\boldsymbol{e}_{1,j}$ and $\boldsymbol{e}_{2,j}$.

Now, the second Newton's law allows the writing of the motion equations:

$$\begin{cases} m_j \ddot{e} - m_j e \dot\chi^2 = F_{ext} \cos(\chi - \varphi) - F_r \\ m_j \ddot\chi + 2m_j \dot{e}\dot\chi = -F_{ext} \sin(\chi - \varphi) + F_t \end{cases} \tag{2.88}$$

where,

m_j is the journal mass (Kg).

Equations (2.88) are second-order differential equations in e and χ, and they have been implemented in MATLAB/Simulink for a numerical solution. Thus, the calculation of both radial ($e, \dot{e}, \ddot{e}$) and angular ($\chi, \dot{\chi}, \ddot{\chi}$) dynamic quantities at each time step is performed. The quantities calculated at the instant of time t will be used by the "Reynolds equation solver block" for the determination of the pressure distribution at instant of time $t + 1$ (Figure 2.27)
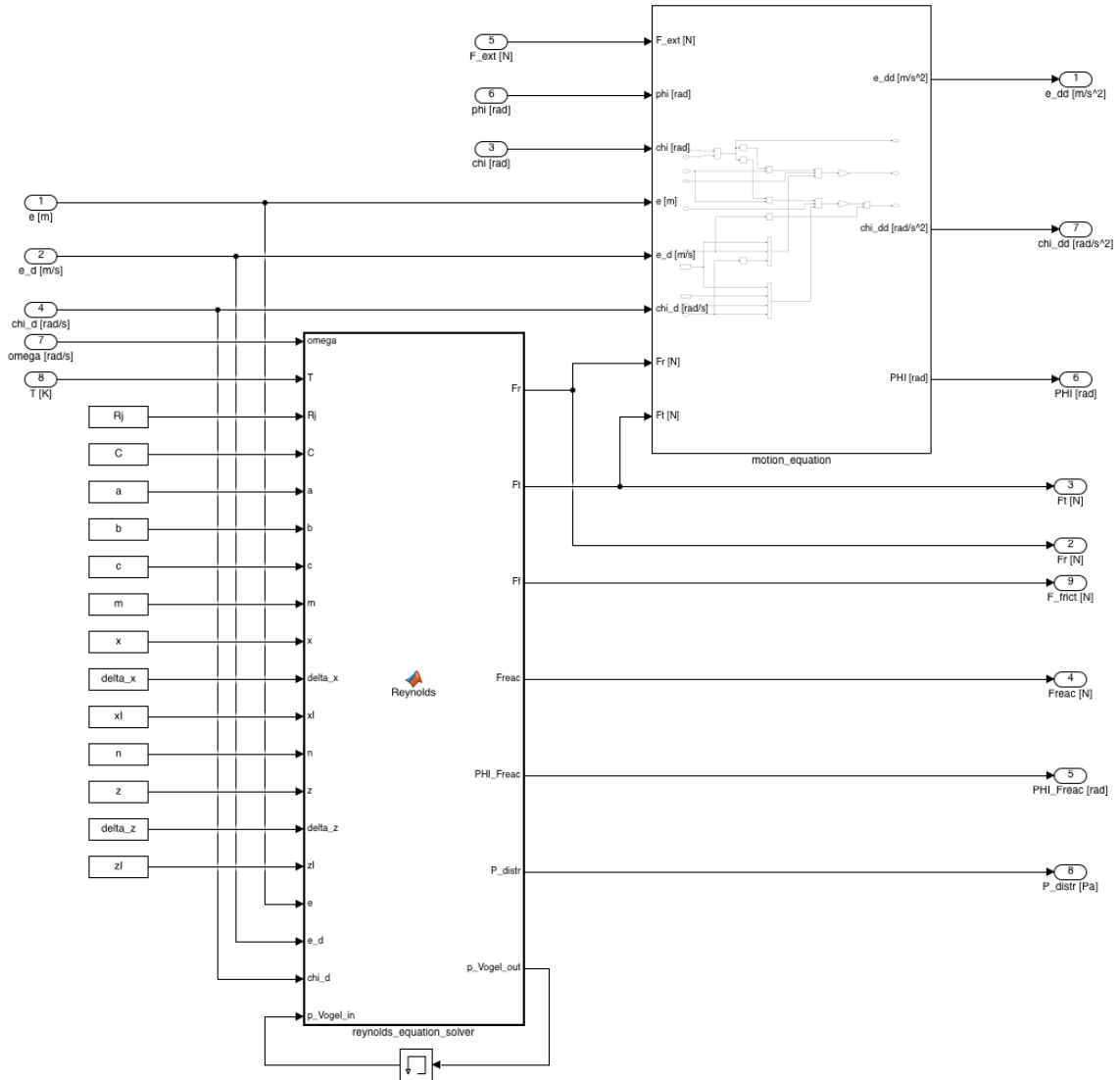

Figure 2.27:   Simulink implementation of the hydrodynamic lubrication model.

66

Chapter 3

Contact model

Hydrodynamic lubrication is responsible for maintaining the journal surface separated from the bearing surface thanks to the pressure field generated. This effect is reduced when one or more of the following aspects occur:

- the sliding velocity is reduced;

- the external force is increased;

- the lubricant viscosity is reduced. This may occur both due to the lubricant degradation and an increase of temperature.

These three effects are visible on the trajectory of the journal, as shown in Figure 3.1.The upper figure shows the trajectory of the journal where $\omega = 50\ rad/\text{s}$, $F_{ext} = 250\ N$ and $T = 20\ °C$. The three bottom figures separately show the effect of the half reduction of the velocity ($\omega = 25\ rad/\text{s}$), the doubling of the force ($F_{ext} = 500\ N$) and the increase of temperature till $T = 60\ °C$


Journal trajectory
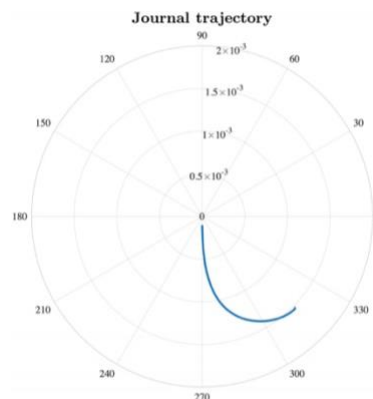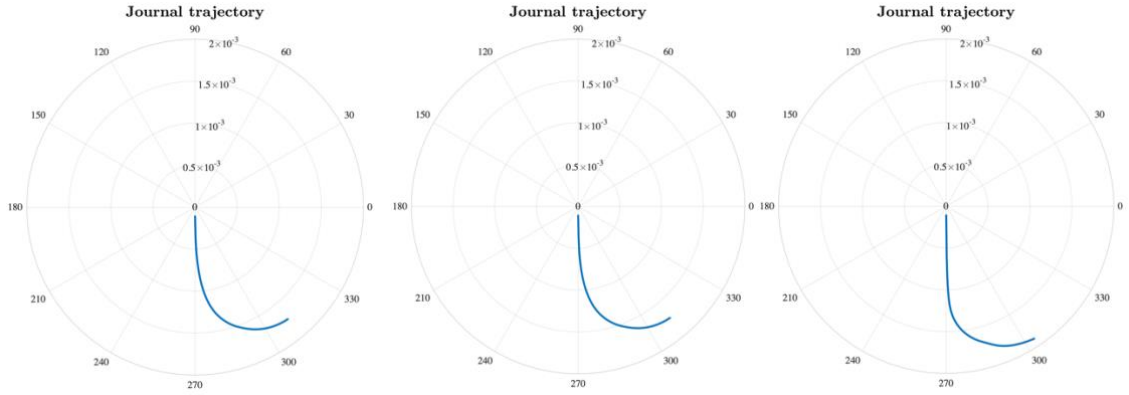
Figure 3.1:   Effect of sliding velocity reduction (bottom left side); effect of external force increment (middle); effect of temperature increment (bottom right side).

For the four work conditions the simulation time is fixed at 0.5 seconds, and, as we can see, the journal tends to get further away from the bearing centre when one of the previous effects takes place, meaning that the hydrodynamic sustenance is gradually reduced.

Eventually though, the film thickness will have diminished to such a level that the small high points or asperities on each surface will come into contact. Contact between asperities causes wear and elevated friction. This condition, where the hydrodynamic film still supports the load but cannot prevent some contact between the opposing surfaces, is known as "partial hydrodynamic lubrication". When the film thickness is reduced still further, the hydrodynamic lubrication fails completely and solid contact occurs [3].
In this chapter the contact between the journal and the bearing is analysed in order to obtain the motion equation and the pressure distribution.

3.1 Journal dynamic

The same procedure used for the determination of the journal motion equations in the hydrodynamic condition can be applied when the contact between surface occurs.
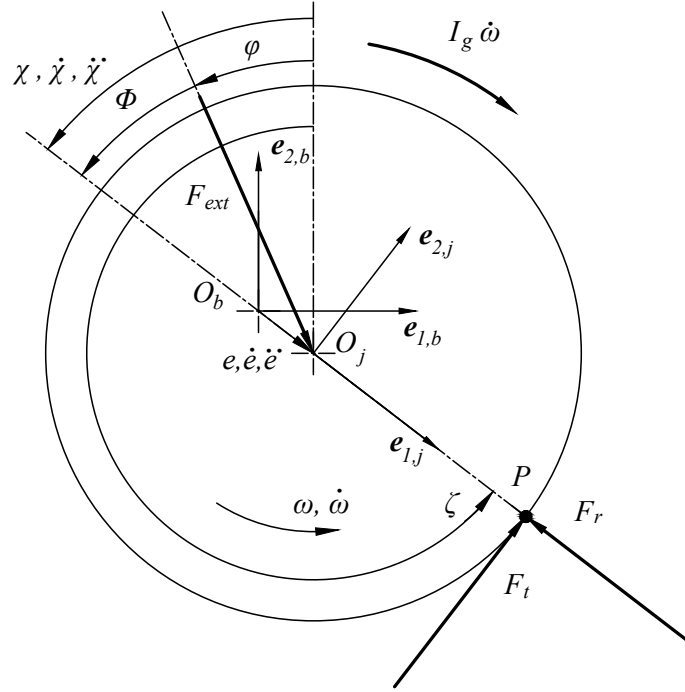

Figure 3.2: Journal free body diagram in contract condition.

Since equations (2.87) are still valid, the forces balance can be obtained using the free body diagram shown in Figure 3.2:

$$\begin{cases} m_j \ddot{e} - m_j e \dot{\chi}^2 = F_{ext} \cos(\chi - \varphi) - F_r \\ m_j \ddot{\chi} + 2 m_j \dot{e} \dot{\chi} = -F_{ext} \sin(\chi - \varphi) + F_t \end{cases} \tag{3.1}$$

which is exactly the same as (2.88). In this case F_r and F_t are not hydrodynamic forces, but the radial and the tangential friction forces due to the body pressing, acting at the point of contact P.

It's important, for a better interpretation of future results, to point out that, both in hydrodynamic and contact conditions, F_r is positive if the force is discordant respect to $e_{1,j}$, while F_t is positive if the force is concordant respect to $e_{2,j}$.

3.1.1 Radial force

The radial force F_r is applied in the direction perpendicular to the plane of contact and different models have been developed to explain the changes of this force on the contacting surface [18].

The best-known nonlinear force model for the contact between two spheres of isotropic materials was firstly developed by Hertz [19]. However, this law is restricted to frictionless surfaces and perfectly elastic solids; two hypothesis that are not verified in this application. Moreover, Hertz force model does not take into account the energy dissipation during the contact process, it cannot model the whole contact process accurately [20].

Lankarani and Nikravesh [21] utilized the general trend of the Hertzian contact law incorporated with a hysteresis damping factor to propose a continuous contact force model for the contact-impact analysis of multibody systems:

$$F_r = K\delta_p{}^n + D\dot{\delta}_p \qquad (3.2)$$

where:

K	is the generalized stiffness parameter (N/m);
D	is the hysteresis damping coefficient (Ns/m);
δ_p	is the relative penetration depth (m), it will be defined in the following chapter;
$\dot{\delta}_p$	is the relative impact velocity (m/s);
n	exponential equal to 1.5 for metallic materials (-).

In this work the contact occurs between two cylindrical shaped bodies. An experimentally validated contact force model, valid for cylindrical contact, is the Johnson model [22]. Unfortunately, due to its logarithmic form, its range of application is not general. Furthermore, the solution of Johnson equation requires a numerical iterative technique that may become computationally expensive.

The most serious problem with the Lankarani and Nikravesh contact model is that it is not a good representation of cylindrical contact, leading to contact forces much lower than those predicted by the Johnson model, which is experimentally validated [23]. On the other hand, equation (3.2) has no mathematical limitation and it does not require the use of any iterative procedure.

Pereira, Ramalho and Ambrosio [23] developed an enhanced cylindrical contact force model using the Johnson model as a reference, due to its accurate representation of cylindrical contact force, and the Lankarani and Nikravesh model as a template, due to its low computation expense.

The best correlation between the Johnson contact model and the new enhanced model is obtained in the form:

$$F_r = \frac{(aC + b)LE^*}{C} \delta_p^{\ n} \left(1 + \frac{3(1 - c_e^{\ 2})}{4} \frac{\dot{\delta}_p}{\dot{\delta}_p^{\ (-)}}\right) \tag{3.3}$$

where:

$a = 0.965$ for internal contact (-);

$b = 0.0965$ for internal contact (m);

$E^* = \frac{E_b}{1-\nu_b^{\ 2}} + \frac{E_j}{1-\nu_j^{\ 2}}$ where E and ν are, respectively, the Poisson's ratio and Young's modulus of the journal and the bearing (Pa);

$c_e = 0.9$ is the restitution coefficient (-);

$\dot{\delta}_p^{\ (-)}$ is the relative initial normal impact velocity (m/s).

For the exponential n, it was not possible to find a simple number to obtain a good fit for the complete range of clearances [23]:

$$n = Y \ C^{-0.005} \tag{3.4}$$

where:

$$Y = \begin{cases} 1.51\big(ln(1000 \ C)\big)^{-0.151} & if \ C \in [0.005, 0.34954[\ mm \\ 0.0151 \ C + 1.151 & if \ C \in [0.34954, 10.0[\ mm \end{cases}$$

It's important to notice that equation (3.3) is valid only for the case where the energy dissipation is relatively small when compared to the maximum absorbed elastic energy, that is, the restitution coefficient is required to be near the unity [20]. Moreover, equation (3.3), was derived by Pereira, Ramalho and Ambrosio considering the geometrical and material properties of cylindrical bodies summarized in the following table:

Property	Range of variation
Clearance	$50 \ \mu m \leq C \leq 10 \ mm$
Young's modulus	$0.1 \leq E \leq 0.5$
Poisson's ratio	$20.7 \ GPa \leq \nu \leq 10000 \ GPa$

Table 3.1:   Ranges of validity for equation (3.3).

3.1.2 Tangential friction force

The friction phenomenon is generated when two contacting bodies slide or tend to slide from each other. The presence of friction manifests itself in the form of tangential forces generated on the contact surface and acting in a direction opposite to that of the relative motion between the two contacting bodies. Friction is a quite complex phenomenon which involves, for example, surface roughness, relative velocity, squeezing forces and it may lead to different friction regimes such as sliding and sticking [24].

In a journal bearing there are three different work conditions, linked to the sliding velocity v_t between the contacting surfaces and the journal angular velocity ω, that lead to three different types of friction force. The relative sliding velocity is given by the sum of two contributions: the journal angular velocity around its own centre and the relative angular velocity of the journal around the bearing centre:

$$v_t = \omega R_j + \left(e + R_j\right) \dot{\chi} \tag{3.5}$$

Depending on the values of v_t and ω, each condition is explained one at the time:

- $v_t \neq 0$

  In this case there is a relative velocity between the journal and the bearing, thus the system is working in dynamic friction condition. The most fundamental and simplest friction force model for sliding friction is the Coulomb's law. This model relates tangential and normal components of reaction force at the contact point by the friction coefficient [25]. The definition of the Coulomb's friction law poses numerical difficulties where the relative tangential velocity is in the vicinity of zero. The problem arises during the integration process of (3.1) because the friction force changes instantaneously from $+F_t$ to $-F_t$ for small positive and negative values of the relative velocity, which is perceived by the integration algorithm as a high frequency content in the dynamic response that leads to successive decreases in the integration time step and undesired oscillations (Figure 3.3) [26].
  A continuous friction force-velocity model, compatible with the requirement for a stable integration, was presented by Ambrósio [27]:

$$\boldsymbol{F}_t = -f_d c_d F_r \, \frac{\boldsymbol{v}_t}{|\boldsymbol{v}_t|} \tag{3.6}$$

where:

f_d is the dynamic friction coefficient (-);

F_r is the radial normal contact force (N);

$\boldsymbol{v}_t$ is the sliding velocity (m/s);

$c_d = \begin{cases} 0 & if \quad |\boldsymbol{v}_t| \leq v_0 \\ \frac{|\boldsymbol{v}_t| - v_0}{v_1 - v_0} & if \quad v_0 < |\boldsymbol{v}_t| < v_1 \\ 1 & if \quad |\boldsymbol{v}_t| \geq v_1 \end{cases}$ is the restitution coefficient (-), where v_0 and v_1 are given tolerances for the relative tangential velocity (m/s), as shown in Figure 3.3.
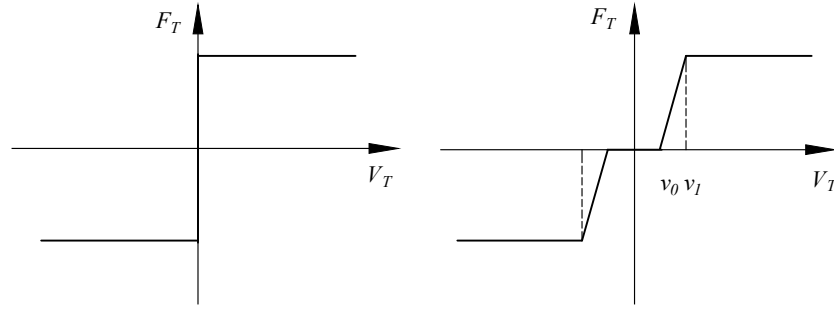
Figure 3.3:   Standard Coulomb's friction law (left) and modified Coulomb's friction law (right).

Considering that ω and $\dot{\chi}$ are defined positive if their direction is counter clockwise (Figure 2.8 and Figure 3.2), v_t is positive if concordant with $\boldsymbol{e}_{2,j}$ and negative otherwise. In relation with the sign convention defined in Figure 2.26 and Figure 3.2 for F_r and F_t, we can say that:

$$\begin{cases} F_t = -f_d c_d F_r & if \quad v_t > 0 \\ F_t = f_d c_d F_r & if \quad v_t < 0 \end{cases} \tag{3.7}$$

- $v_t = 0$ and $\omega = 0$

When, in a generic instant of time t, the journal does not rotate around its centre and the relative speed is zero, adherence between the journal and the bearing is obtained. The intention, here, is to understand if at the instant of time $t + 1$ the

73

system will still work under static friction condition. From a physical point of view, static friction force acts in the opposite direction respect to that force which tends to generate a relative sliding between the surfaces in contact. This force, called active force, is the projection of the external load along the direction defined by $\boldsymbol{e}_{2,j}$:

$$\boldsymbol{F}_{active} = F_{ext} \, sin\Phi \, (-\boldsymbol{e}_{2,j}) \tag{3.8}$$

The previous equation says that if $F_{ext} \, sin\Phi$ is positive then F_t is concordant with $\boldsymbol{e}_{2,j}$ ($F_t > 0$), otherwise it's discordant with $\boldsymbol{e}_{2,j}$ ($F_t < 0$).
Since the sliding speed is zero, the Coulomb's model can be used to obtain the limit value for the static friction:

$$F_{t,lim} = -f_a F_r \tag{3.9}$$

where:

f_a	is the static friction coefficient (-);
F_r	is the radial normal contact force (N).

If the adherence between surfaces is maintained, the journal angular acceleration and speed with respect to the bearing centre ($\ddot{\chi}, \dot{\chi}$) would be zero. Thus, the force equilibrium, along $\boldsymbol{e}_{2,j}$ direction, of the journal free body diagram (Figure 3.2) is:

$$F_t = F_{ext} \, sin\Phi \tag{3.10}$$

Now, the comparison between F_t and $F_{t,lim}$ needs to be done:

$$|F_t| \leq |F_{t,lim}| \tag{3.11}$$

If the result of (3.11) is true, it means that the static condition is maintained, thus $\ddot{\chi}, \dot{\chi}$ are actually zero, so the motion equations that have to be integrated at the instant of time $t+1$ become:

$$\begin{cases} m\ddot{e} = F_{ext} \cos(\chi - \varphi) - F_r \\ F_t = F_{ext} \, sin\Phi \end{cases} \tag{3.12}$$

Otherwise, if (3.11) is false, the external force acting on the journal is too high and the system goes back to a dynamic friction condition (motion equations are (3.1)) where F_t is given by (3.7);

- $v_t = 0$ and $\omega \neq 0$

Under this speed values, equation (3.5) leads to:

$$\dot{\chi} = -\frac{\omega R_j}{\left(e + R_j\right)} \tag{3.13}$$

and the journal rolls without sliding on the bearing surface. Since there is no sliding in pure rolling condition, static friction force occurs at the contact point. By analogy with the previous case, it's necessary to check if the journal maintain this work condition even in the next instant of time.

The rotational equilibrium equation of the free body diagram (Figure 3.2) leads to:

$$F_t = \frac{I_g \, \dot{\omega}}{R_j} \tag{3.14}$$

where:

$I_g = \frac{mR_j^2}{2}$ journal moment of inertia relative to its axis (Kg m²);

$\dot{\omega}$ journal angular acceleration with respect to its centre (rad/s²).

The limit value for the static friction force is calculated in the same way as before (3.9), and, again, we procced with the comparison between F_t and $F_{t,lim}$:

$$|F_t| \leq |F_{t,lim}| \tag{3.15}$$

If (3.15) is true, the static friction condition is verified and the journal keeps its pure rotation motion over the bearing, otherwise, as it happened in the previous case, the external force acting on the journal is too high and the system goes back to a dynamic friction condition. Notice that in both pure rotation and dynamic conditions the motion equation are always the same (3.1); what changes is the F_t value, which is given by (3.14) in pure rotation condition and by (3.7) in dynamic condition.

The journal motion equations are time-dependent differential equations and they are solved numerically by Simulink at each instant of time accordingly with the time step chosen. Now, the probability that the instants of time on which the equations are solved correspond with the instants of time where v_t is equal to zero is very unlikely. Therefore, the detection of zero sliding velocity is entrusted to zero-crossing blocks, that give a Boolean true value as output if the input crosses a defined value (in our case zero). In Figure 3.4 is shown how the three work conditions previously explained have been implemented in Simulink.
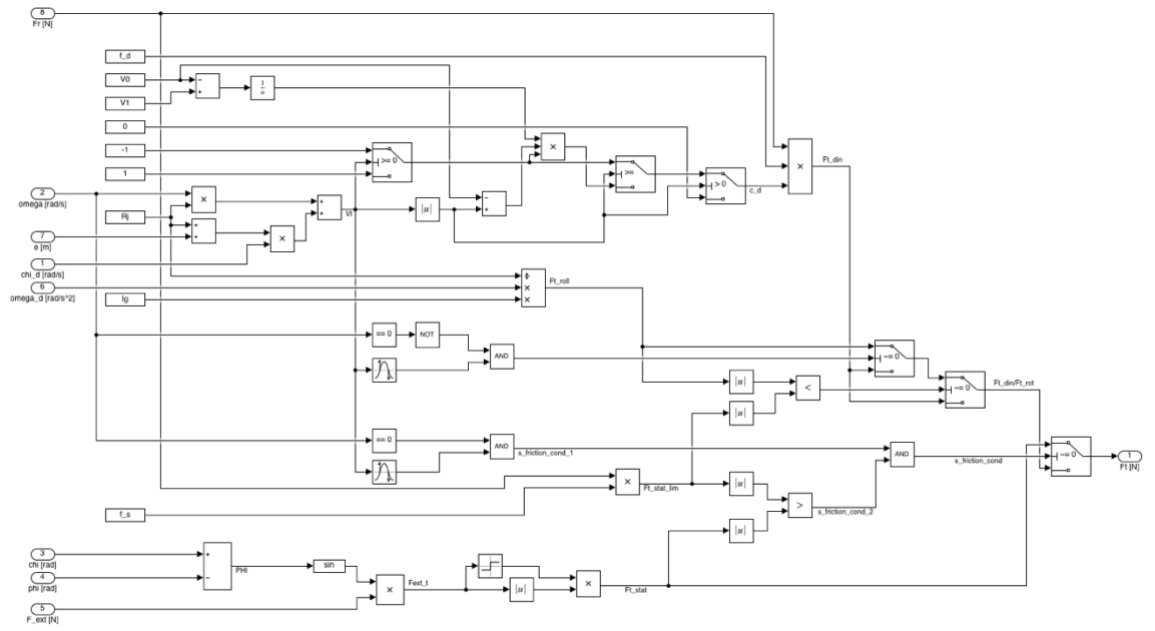
Figure 3.4: Simulink implementation of tangential friction force.

3.2   Pressure distribution

Even for the contact model, the pressure distribution over the journal surface needs to be calculated. The equation used for this purpose are the equations developed by Hertz in his contact theory. For the contact between two cylinders with parallel axes, the contact zone is a rectangle with length equal to L and width equal to $2h_{wid}$, where:

$$h_{wid} = \sqrt{\frac{F_r}{\pi L} \frac{1}{E^* \Sigma \rho}} \qquad (3.16)$$

where:

F_r is the contact normal force (3.3) (N);

$\Sigma \rho = \frac{1}{R_j} - \frac{1}{R_b}$ is the sum of curvatures (1/m).

The pressure distribution is given by:

$$p = 2 \frac{F_r}{\pi L h_{wid}} \sqrt{1 - \left(\frac{x'}{h_{wid}}\right)^2} \qquad (3.17)$$

where:

x' is the axis whose origin is located where the contact occurs.

The same space discretization used for the integration of Reynolds equation is used here to calculate the pressure distribution in contact condition. As we can see in Figure 3.5, the relation between the x -axis and the x'-axis is: $x' = x - \pi R_j$.
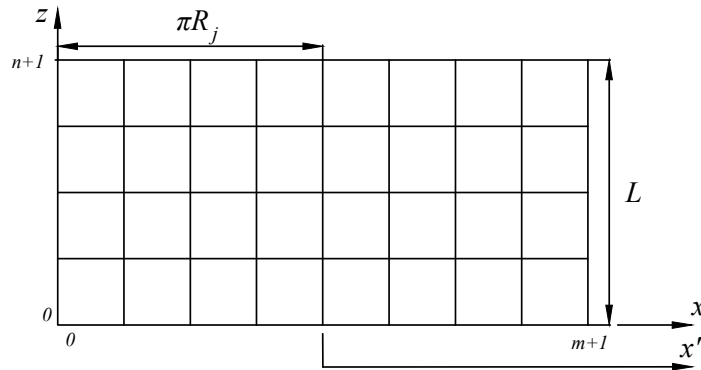

Figure 3.5:   Space discretization and relation between the coordinate x and x'.

The MATLAB function developed for the contact pressure distribution is available in Appendix B.

Chapter 4

Mixed model

If the lubricating film separating the surfaces is such to allow some contact between the asperities, then this type of lubrication is considered in the literature as "mixed" or "partial lubrication". The contact load is shared between the contacting asperities and the film when mixed or partial lubrication prevails [3].

In the mixed model, hydrodynamic and contact models have been fused considering a parameter proposed by Tallian [28] that express the local film variation as a function of local surface roughness:

$$\lambda_T = \frac{h_{min}}{\sqrt{\sigma_j{}^2 + \sigma_b{}^2}} \tag{4.1}$$

where:

$h_{min} = C - e$ is the minimum film thickness (m);

σ_j is the RMS surface roughness of the journal (m);

σ_j is the RMS surface roughness of the bearing (m);

λ_T Tallian lambda (-).

Using the Tallian lambda, it's possible to discriminate the condition under which the system is working, as summarized in Table 4.1.

Tallian parameter range	Description	Model used
$\lambda_T < 1$	Surface smearing or deformation accompanied by wear can occur. Certain contact between surfaces.	Contact model (Chapter 3)
$1 \leq \lambda_T < 1.5$	Surface distress is possible. The term "surface distress" means that surface glazing and spalling will occur. The original surface roughness has been suppressed by extreme plastic deformation of the asperities.	Mixed model (Chapter 4)
$1.5 \leq \lambda_T < 3$	Some glazing of the surface may occur; however, this glazing will not impair bearing operation or result in pitting.	
$3 \leq \lambda_T \leq 4$	Minimal wear can be expected with no glazing.	
$\lambda_T > 4$	Full separation of the surfaces by a lubricant film.	Hydrodynamic lubrication model (Chapter 2)

Table 4.1: System work conditions as function of λ_T (adapted from [3]).

The journal movement, in partial lubrication condition, is described by the same motion equations obtained in hydrodynamic and contact models (equations (2.88) and (3.1)).

To be able to resolve the motion equations the forces F_r and F_t are needed. To guarantee the continuity between models, these forces are calculated using the radial and tangential forces coming from the hydrodynamic and contact models weighted as a function of the Tallian lambda. Therefore, when λ_T increases from 1 to 4 the radial and tangential forces coming from the contact model are progressively reduced from 100% to 0%, meanwhile the radial and tangential forces coming from the hydrodynamic model are progressively increased from 0% to 100%. Then, the weighted forces are added to each other to compose the mixed radial and tangential forces. The reverse thing happens when λ_T goes from 4 to 1.

The same procedure has been used for the determination of the friction force and the pressure distribution.

The scale parameters used the progressive variation of the forces are:

$$\begin{cases} \dfrac{\lambda_T - 1}{4 - 1} \\[3mm] 1 - \dfrac{\lambda_T - 1}{4 - 1} \end{cases} \tag{4.2}$$

where the first equation is used for the forces coming from the hydrodynamic model, while, the second one, for those coming from the contact model.

In Figure 4.1, the Simulink implementation of the mixed model is displayed:
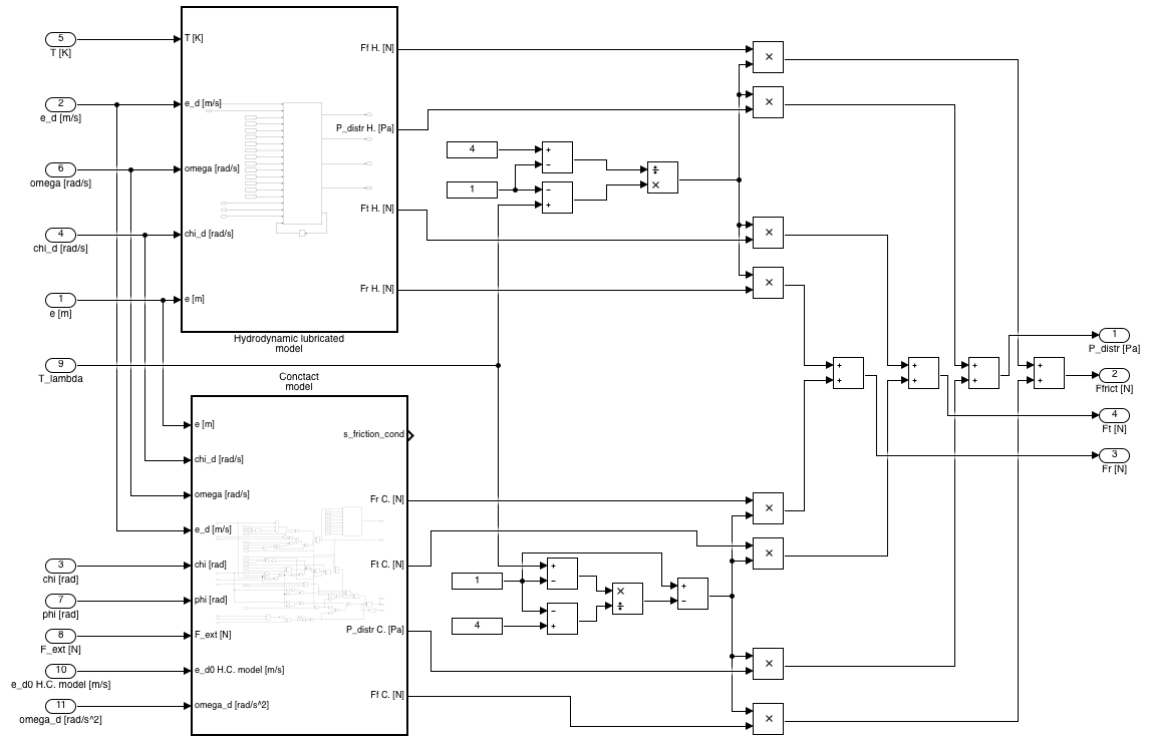

Figure 4.1:   Simulink implementation of the mixed model.

The Tallian parameter allows the definition of the penetration depth δ_p, that was left in suspense in the previous chapter (equation (3.3)). Since the contact between the journal and the bearing surfaces starts when λ_T reaches 4, equation (4.1) allows the calculation of the eccentricity to which corresponds indentation equal to zero:

$$e_{\delta_p=0} = C - 4\sqrt{\sigma_j{}^2 + \sigma_b{}^2} \tag{4.3}$$

Thus, the penetration depth is:

$$\delta_p = e - e_{\delta_p=0} = e - \left(C - 4\sqrt{\sigma_j{}^2 + \sigma_b{}^2}\right) \tag{4.4}$$

Notice that (4.4) makes sense only for the mixed and contact models, i.e. for $e \geq e_{\delta_p=0}$ or $\lambda_T \leq 4$.

Chapter 5

Mechanism configuration

The hydrodynamic lubrication and contact models require as input the relative angular speed between the journal and bearing surfaces (ω) and the direction of the external force (φ). These parameters can be obtained analysing the mechanism that provides the connection between the actuator and the primary flight control surface.

Since this mechanism varies from aircraft to aircraft and depends on the surface that needs to be controlled, a simple configuration, composed by three links, has been chosen:
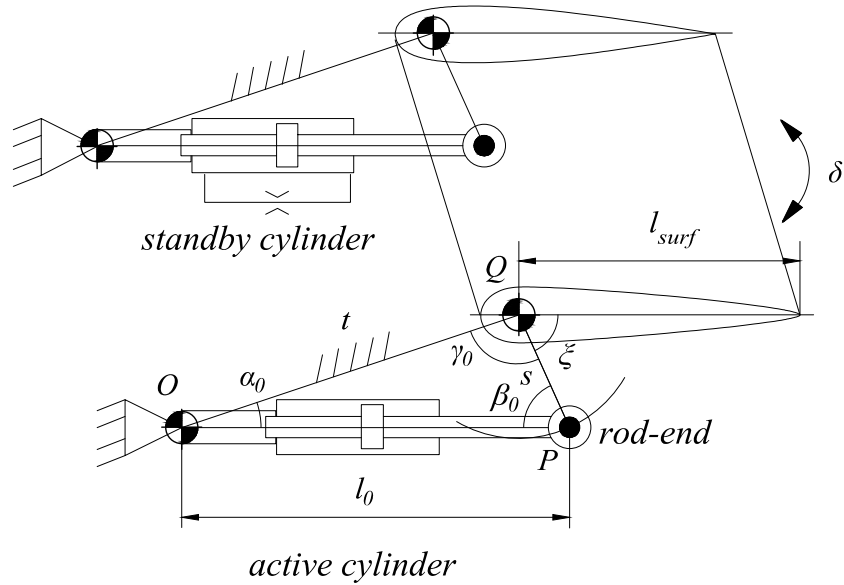
Figure 5.1: Geometric arrangement of redundant actuators [29].

The mechanism is realized by the link of length 'l' on which is mounted the actuator system, a frame of length 't' and inclination 'η' respect to the horizontal line and a third link called "surface link" which is characterized by a L shape (with an angle 'ξ'), one side of length 's' and the other side of length 'l_{surf}'. Thus, the link with the actuator can rotate around the frame in 'O', while the surface link in 'Q'.

The rod-end allows the connection between the piston rod and the surface link in 'P'. To be more specific, the piston rod is fixed with the bearing of the rod-end, whereas the crank is connected with the journal, as visible in Figure 5.1.

By using as input η, t, s, l and the linear speed and acceleration of the piston $\dot{l}, \ddot{l}$, it is possible to calculate angular positions (α, β, γ), speeds $(\dot{\alpha}, \dot{\beta}, \dot{\gamma})$ and accelerations $(\ddot{\alpha}, \ddot{\beta}, \ddot{\gamma})$ of one link with respect to each other. At first, these kinematic quantities are calculated in ideal conditions, i.e. considering that the rod-end journal is coaxial with the bearing (eccentricity equal to zero). Next, the effect of the rod-end presence will be considered on the mechanism, in particular to assess the error generated on the link of length 's' which will be used in the next chapter to solve the surface dynamic.

5.1 Ideal conditions

Taking under consideration the mechanism scheme, in a generic configuration, represented in Figure 5.2, through the relative motion equations, the position, speed and acceleration of the point 'P' can be obtained.
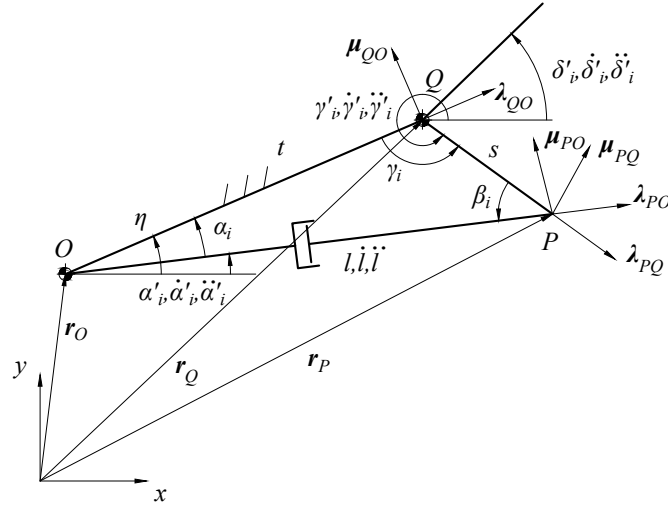

Figure 5.2: Generic mechanism configuration under ideal conditions.

In Figure 5.2, the kinematic quantities characterized by the apex " ' ", describe the position, speed and acceleration of each link with respect the horizontal line, while the subscript 'i' specifies that the variables are evaluated under ideal conditions. Once again, the arrow of each quantity describes the direction chosen as positive.

Four reference systems are used:

- the first one, with axis 'x' and 'y' placed in a generic position;

- the second one characterized by a unit vector λ_{PQ}, parallel to the side of the surface link of length 's', and a second unit vector μ_{PQ}, perpendicular to the first. It is fixed in 'P';

- the third one, similar to the previous one but related to the actuator link. The unit vectors are λ_{PO} and μ_{PO};

- the fourth one, similar to the previous, but related to the frame link. The unit vectors are λ_{QO} and μ_{QO}.

84

Now the relative motion equations are used. By expressing the motion of the point P with respect the point 'O':

$$\begin{cases} \boldsymbol{r}_P = \boldsymbol{r}_O + l\,\boldsymbol{\lambda}_{PO} \\ \boldsymbol{v}_P = \boldsymbol{v}_O + l\dot{\alpha}'_i\,\boldsymbol{\mu}_{PO} + \dot{l}\,\boldsymbol{\lambda}_{PO} \\ \boldsymbol{a}_P = \boldsymbol{a}_O + l\ddot{\alpha}'_i\,\boldsymbol{\mu}_{PO} + l\dot{\alpha}'^2_i(-\boldsymbol{\lambda}_{PO}) + 2\dot{l}\dot{\alpha}'_i\,\boldsymbol{\mu}_{PO} + \ddot{l}\,\boldsymbol{\lambda}_{PO} \end{cases} \tag{5.1}$$

where $\boldsymbol{v}_O$ and $\boldsymbol{a}_O$ are zero.

But the motion of 'P' can also be evaluated with respect to 'Q':

$$\begin{cases} \boldsymbol{r}_P = \boldsymbol{r}_Q + s\,\boldsymbol{\lambda}_{PQ} \\ \boldsymbol{v}_P = \boldsymbol{v}_Q + s\dot{\gamma}'_i\,\boldsymbol{\mu}_{PQ} \\ \boldsymbol{a}_P = \boldsymbol{a}_Q + s\ddot{\gamma}'_i\,\boldsymbol{\mu}_{PQ} + s\dot{\gamma}'^2_i(-\boldsymbol{\lambda}_{PQ}) \end{cases} \tag{5.2}$$

where $\boldsymbol{v}_Q$ and $\boldsymbol{a}_Q$ are zero.

The relative motion equations of 'Q' with respect to 'O' are reduce to:

$$\boldsymbol{r}_Q = \boldsymbol{r}_O + t\,\boldsymbol{\lambda}_{QO} \tag{5.3}$$

From Figure 5.2 the relations between the kinematic quantities with and without the apex " ' " are obtained:

$$\begin{cases} \gamma_i = \gamma'_i - \eta - \pi \\ \alpha_i = \eta - \alpha'_i \\ \beta_i = 2\pi - \gamma'_i + \alpha'_i \end{cases} \Longrightarrow \begin{cases} \dot{\gamma}_i = \dot{\gamma}'_i \\ \dot{\alpha}_i = -\dot{\alpha}'_i \\ \dot{\beta}_i = \dot{\alpha}'_i - \dot{\gamma}'_i \end{cases} \Longrightarrow \begin{cases} \ddot{\gamma}_i = \ddot{\gamma}'_i \\ \ddot{\alpha}_i = -\ddot{\alpha}'_i \\ \ddot{\beta}_i = \ddot{\alpha}'_i - \ddot{\gamma}'_i \end{cases} \tag{5.4}$$

In conclusion the relation between the reference systems fixed in 'P' is:

$$\begin{cases} \boldsymbol{\lambda}_{PQ} = \cos(\gamma'_i - \alpha'_i)\,\boldsymbol{\lambda}_{PO} + \sin(\gamma'_i - \alpha'_i)\boldsymbol{\mu}_{PO} = \cos\beta_i\,\boldsymbol{\lambda}_{PO} - \sin\beta_i\,\boldsymbol{\mu}_{PO} \\ \boldsymbol{\mu}_{PQ} = -\sin(\gamma'_i - \alpha'_i)\,\boldsymbol{\lambda}_{PO} + \cos(\gamma'_i - \alpha'_i)\,\boldsymbol{\mu}_{PO} = \sin\beta_i\,\boldsymbol{\lambda}_{PO} + \cos\beta_i\,\boldsymbol{\mu}_{PO} \end{cases}$$

$$\begin{cases} \boldsymbol{\lambda}_{QO} = \cos(\eta - \alpha'_i)\,\boldsymbol{\lambda}_{PO} + sin(\eta - \alpha'_i)\,\boldsymbol{\mu}_{PO} = \cos\alpha_i\,\boldsymbol{\lambda}_{PO} + \sin\alpha_i\,\boldsymbol{\mu}_{PO} \\ \boldsymbol{\mu}_{QO} = -sin(\eta - \alpha'_i)\,\boldsymbol{\lambda}_{PO} + \cos(\eta - \alpha'_i)\,\boldsymbol{\mu}_{PO} = -\sin\alpha_i\,\boldsymbol{\lambda}_{PO} + \cos\alpha_i\,\boldsymbol{\mu}_{PO} \end{cases} \tag{5.5}$$

The unknown kinematic quantities can be obtained noticing that position, speed and acceleration of 'P', evaluated with respect to 'O' and 'Q', must be equal. Thus, equations (5.1) and (5.2) can be equalled one by one.

5.1.1 Angular positions

By equalling the first equations of (5.1) and (5.2), and using (5.5):

$$l\,\boldsymbol{\lambda}_{PO} = (t\,cos\alpha_i + s\,cos\beta_i)\,\boldsymbol{\lambda}_{PO} + (t\,sin\alpha_i - s\,sin\beta_i)\,\boldsymbol{\mu}_{PO} \qquad (5.6)$$

Thus, the angle between the actuator rod and the surface link is obtained:

$$\beta_i = acos\left(\frac{l - t\,cos\alpha_i}{s}\right) \qquad (5.7)$$

The angles γ_i and α_i are evaluated using the law of cosines:

$$\begin{cases} \gamma_i = acos\left(\dfrac{t^2 + s^2 - l^2}{2st}\right) \\[2ex] \alpha_i = acos\left(\dfrac{l^2 + t - s^2}{2lt}\right) \end{cases} \qquad (5.8)$$

5.1.2 Angular velocities

By equalling the second equations of (5.1) and (5.2), and using (5.5):

$$l\dot{\alpha}'_i\,\boldsymbol{\mu}_{PO} + \dot{l}\,\boldsymbol{\lambda}_{PO} = s\dot{\gamma}'sin\beta_i\,\boldsymbol{\lambda}_{PO} + s\dot{\gamma}'cos\beta_i\,\boldsymbol{\mu}_{PO} \qquad (5.9)$$

Considering again (5.4), the angular velocities are obtained:

$$\begin{cases} \dot{\gamma}_i = \dot{\gamma}'_i = \dfrac{\dot{l}}{s\,sin\beta_i} \\[2ex] \dot{\alpha}_i = -\dot{\alpha}'_i = -\dfrac{\dot{l}}{l\,tan\beta_i} \\[2ex] \dot{\beta}_i = \dot{\alpha}'_i - \dot{\gamma}'_i = \dfrac{\dot{l}}{l\,tan\beta_i} - \dfrac{\dot{l}}{s\,sin\beta_i} \end{cases} \qquad (5.10)$$

5.1.3 Angular accelerations

By equalling the third equations of (5.1) and (5.2), and using (5.5):

$$
\begin{aligned}
(l\ddot{\alpha}'_i + 2\dot{l}\dot{\alpha}'_i)\,\boldsymbol{\mu}_{PO} + \left(\ddot{l} - l\dot{\alpha}'^{\,2}_i\right)\boldsymbol{\lambda}_{PO} = \\
= (s\ddot{\gamma}'_i \sin\beta_i - s\dot{\gamma}'^{\,2}_i \cos\beta_i)\,\boldsymbol{\lambda}_{PO} + (s\ddot{\gamma}'_i \cos\beta_i + s\dot{\gamma}'^{\,2}_i \sin\beta_i)\,\boldsymbol{\mu}_{PO}
\end{aligned}
\tag{5.11}
$$

Considering again (5.4), the angular accelerations are obtained:

$$
\begin{cases}
\ddot{\gamma}_i = \ddot{\gamma}'_i = \dfrac{\ddot{l} + l\dot{\alpha}_i^2 + s\dot{\gamma}_i^2\cos\beta_i}{s\,\sin\beta_i} \\[3mm]
\ddot{\alpha}_i = -\ddot{\alpha}'_i = -\dfrac{2\dot{l}\dot{\alpha}_i + s\ddot{\gamma}_i\cos\beta_i + s\dot{\gamma}_i^2\sin\beta_i}{l} \\[3mm]
\ddot{\beta}_i = \ddot{\alpha}'_i - \ddot{\gamma}'_i = -\dfrac{2\dot{l}\dot{\alpha}_i + s\ddot{\gamma}_i\cos\beta_i + s\dot{\gamma}_i^2\sin\beta_i}{l} - \dfrac{\ddot{l} + l\dot{\alpha}_i^2 + s\dot{\gamma}_i^2\cos\beta_i}{s\,\sin\beta_i}
\end{cases}
\tag{5.12}
$$

5.2   Real conditions

As already said, the rod-end model described previously is able to give at any instant of time the relative position (e, χ), speed $(\dot{e}, \dot{\chi})$, and acceleration $(\ddot{e}, \ddot{\chi})$, of the journal centre with respect to the bearing centre. Thus, the presence of the rod-end modifies the ideal configuration exposed in the previous subchapter introducing errors on the kinematic quantities of the elements of the mechanism. The rod-end effects are called errors because they generate a variation of position of the link of length '*s*' and, thus, of the controlled surface position, and its derivatives, respect a condition where the connection is realized with an ideal joint.
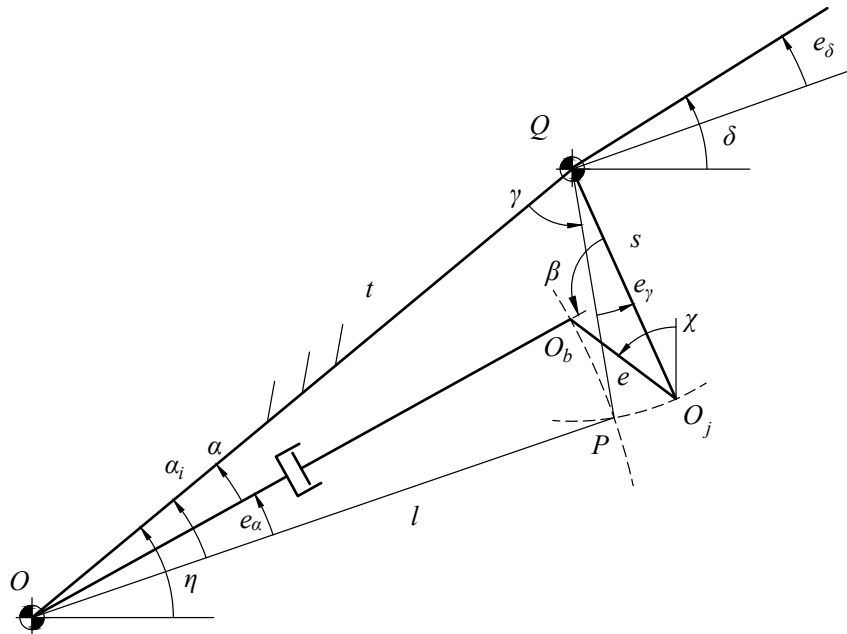
Figure 5.3:   Generic mechanism configuration in real conditions (thick lines) compared with the relative configuration in ideal conditions (thin lines).

In Figure 5.3, the effect of the rod-end is shown, where, in order to maintain the scheme easy to read, only the position quantities are displayed and the eccentricity value has been considerably enlarged respect the other dimension of the system.
For a given set of values coming from the rod-end model (e, χ) and a fixed position of the actuator (l), the links of the mechanism will be arranged in a certain position as function of their degrees of freedom:

- the actuator link will rotate around the frame in 'O' generating the error e_α;

- the surface link will rotate around the frame in 'Q' generating the error e_γ for the side of length 's';

- the frame, as such, will maintain its position.

Thus, as shown in Figure 5.3, the mechanism, under real condition, can be modelled as a articulated quadrilateral where the connecting rod is given by the connection between the journal and the bearing centres.

The goal of this subchapter is the calculation of the real kinematic quantities of the links of the mechanism for given values of e, χ, l and the associated derivatives. This can be done considering the loop closure equations for the articulated quadrilateral and the small-angle approximation.

5.2.1 Angular positions

By projecting the links of the mechanism along the parallel and perpendicular directions of the frame, the loop closure equations are obtained:

$$\begin{cases} l\,\cos(\alpha_i + e_\alpha) + e\,\sin(\chi - \eta) + s\,\cos(\gamma_i + e_\gamma) = t \\ l\,\sin(\alpha_i + e_\alpha) + e\,\cos(\chi - \eta) = s\,\sin(\gamma_i + e_\gamma) \end{cases} \tag{5.13}$$

where the unknown quantities are $\alpha = \alpha_i + e_\alpha$ and $\gamma = \gamma_i + e_\gamma$.

Since the eccentricity e is very small, the small-angle approximation can be used for e_α and e_γ:

$$\begin{cases} \sin\theta \cong \tan\theta \cong \theta \\ \cos\theta \cong 1 \end{cases} \tag{5.14}$$

The system of equations (5.13) can be solved using the substitution method:

$$\begin{cases} e_\gamma = \dfrac{l\,(\cos\alpha_i + \tan\alpha_i\,\sin\alpha_i) + s\,(\cos\gamma_i - \tan\alpha_i\,\sin\gamma_i)}{s\,(\tan\alpha_i\,\cos\gamma_i - \sin\gamma_i)} + \\ \qquad\qquad + \dfrac{e\,(\tan\alpha_i\,\cos(\chi - \eta) + \sin(\chi - \eta)) - t}{s\,(\tan\alpha_i\,\cos\gamma_i - \sin\gamma_i)} \\[2mm] e_\alpha = \dfrac{1}{\cos\alpha_i}\left(\dfrac{s\,(\sin\gamma_i + \cos\gamma_i\,e_\gamma) - e\,\cos(\chi - \eta)}{l} - \sin\alpha_i\right) \end{cases} \tag{5.15}$$

Thus, the unknown angular positions are obtained:

$$\begin{cases} \alpha = \alpha_i + e_\alpha \\ \gamma = \gamma_i + e_\gamma \end{cases} \tag{5.16}$$

The error on the angle β can be evaluated with simple considerations about triangles. The sum of the internal angles of a triangle is equal to π rad:

$$\begin{cases} \alpha_i + \gamma_i + \beta_i = \pi \\ \alpha + \gamma + \beta = \pi \end{cases} \tag{5.17}$$

thus, substituting (5.16) into (5.17):

$$e_\beta = -(e_\alpha + e_\gamma) \tag{5.18}$$

The angle between the actuator and surface links is:

$$\beta = \beta_i + e_\beta \tag{5.19}$$

5.2.2 Angular velocities

The real angular velocities can be obtained by deriving the loop closure equations (5.13):

$$\begin{cases} \dot{l}\,cos\alpha - l\,sin\alpha\,(\dot{\alpha}_i + \dot{e_\alpha}) + \dot{e}\,sin(\chi - \eta) + e\,cos(\chi - \eta)\,\dot{\chi} + \\ \qquad\qquad\qquad\qquad\qquad\qquad -s\,sin\gamma\,(\dot{\gamma}_i + \dot{e_\gamma}) = 0 \\ \dot{l}\,sin\alpha + l\,cos\alpha\,(\dot{\alpha}_i + \dot{e_\alpha}) + \dot{e}\,cos(\chi - \eta) - e\,sin(\chi - \eta)\,\dot{\chi} = \\ \qquad\qquad\qquad\qquad\qquad\qquad = s\,cos\gamma\,(\dot{\gamma}_i + \dot{e_\gamma}) \end{cases} \tag{5.20}$$

Again, using the substitution method:

$$\begin{cases} \dot{e_\gamma} = -\dot{\gamma}_i + \dfrac{l\,(tan\alpha\,sin\alpha + cos\alpha) + \dot{e}\,\big(tan\alpha\,cos(\chi - \eta) + sin(\chi - \eta)\big)}{s\,(tan\alpha\,cos\gamma + sin\gamma)} + \\ \qquad\qquad\qquad\qquad + \dfrac{e\dot{\chi}\,\big(cos(\chi - \eta) - tan\alpha\,sin(\chi - \eta)\big)}{s\,(tan\alpha\,cos\gamma + sin\gamma)} \\ \dot{e_\alpha} = -\dot{\alpha}_i + \dfrac{1}{l\,cos\alpha}\Big(s\,cos\gamma\,(\dot{\gamma}_i + \dot{e_\gamma}) - \dot{e}\,cos(\chi - \eta)\Big) + \\ \qquad\qquad\qquad\qquad + \dfrac{1}{l\,cos\alpha}\big(e\,sin(\chi - \eta)\,\dot{\chi} - \dot{l}\,sin\alpha\big) \end{cases} \tag{5.21}$$

By deriving equations (5.16) and (5.18), we obtain:

$$\begin{cases} \dot{\alpha} = \dot{\alpha}_i + \dot{e_\alpha} \\ \dot{\gamma} = \dot{\gamma}_i + \dot{e_\gamma} \\ \dot{\beta} = \dot{\beta}_i + \dot{e_\beta} \end{cases} \tag{5.22}$$

5.2.3 Angular accelerations

By deriving once again the loop closure equations (5.20) and using the substitutional method:

$$\begin{cases} \ddot{e_\gamma} = -\ddot{\gamma}_i + \dfrac{(\ddot{l} - l\dot{\alpha}^2)(\tan\alpha\ \sin\alpha + \cos\alpha) + 2l\dot{\alpha}\ (\tan\alpha\ \cos\alpha - \sin\alpha)}{s\ (\tan\alpha\ \cos\gamma + \sin\gamma)} + \\ \qquad + \dfrac{s\dot{\gamma}^2(\tan\alpha\ \sin\gamma - \cos\gamma) + (\ddot{e} - e\dot{\chi}^2)\left(\tan\alpha\ \cos(\chi - \eta) + \sin(\chi - \eta)\right)}{s\ (\tan\alpha\ \cos\gamma + \sin\gamma)} + \\ \qquad\qquad + \dfrac{(2\dot{e}\dot{\chi} + e\ddot{\chi})\left(\cos(\chi - \eta) - \tan\alpha\ \sin(\chi - \eta)\right)}{s\ (\tan\alpha\ \cos\gamma + \sin\gamma)} \\[2ex] \ddot{e_\alpha} = -\ddot{\alpha}_i + \dfrac{1}{l\ \cos\alpha}\left(s\ \cos\gamma\ (\ddot{\gamma}_i + \ddot{e}_\gamma) - s\dot{\gamma}^2\ \sin\gamma - (\ddot{l} - l\dot{\alpha}^2)\sin\alpha - 2l\dot{\alpha}\ \cos\alpha\right) \\ \qquad\qquad + \dfrac{1}{l\ \cos\alpha}\left((2\dot{e}\dot{\chi} + e\ddot{\chi})\ \sin(\chi - \eta) - (\ddot{e} - e\dot{\chi}^2)\ \cos(\chi - \eta)\right) \end{cases} \tag{5.23}$$

By deriving equations (5.22) we obtain:

$$\begin{cases} \ddot{\alpha} = \ddot{\alpha}_i + \ddot{e}_\alpha \\ \ddot{\gamma} = \ddot{\gamma}_i + \ddot{e}_\gamma \\ \ddot{\beta} = \ddot{\beta}_i + \ddot{e}_\beta \end{cases} \tag{5.24}$$

The above equations represent the complete analysis of the mechanism; the relative velocity between the journal and the bearing is $\dot{\beta}$ and it is given by (5.22), meanwhile the direction of the external force action on the journal can be obtained noticing that it is always perpendicular to the link of length '*s*' thus:

$$\varphi = \gamma + \eta \tag{5.25}$$

where γ is given by (5.16) using (5.8) and (5.15).

The study of the dynamic behaviour of the surface is described in the following chapter.

5.3 Piston rod actions

Regardless the work condition of the system (hydrodynamic, mixed or contact), the forces acting on the journal are:

- the radial force F_r, which is positive if the force vector is discordant respect to $\boldsymbol{e}_{1,j}$;

- the tangential force F_t and the friction force F_{frict}, which are positive if the force vector is concordant respect to $\boldsymbol{e}_{2,j}$. It is recalled that for the contact model the tangential force is due to the friction phenomenon thus, F_t and F_{frict} coincide. For the hydrodynamic model, instead, the tangential force is the result of the Reynolds equation and it contributes to the journal sustenance, meanwhile the friction force is the braking effect generated by the lubricant due to the rotation of the journal.

Using the action-reaction law and moving correctly the forces on the bearing centre by adding the transportation moments, the actions at the end of the piston rod can be obtained. The three reference systems involved in the calculation are shown in Figure 5.4, together with the bearing and the piston rod:
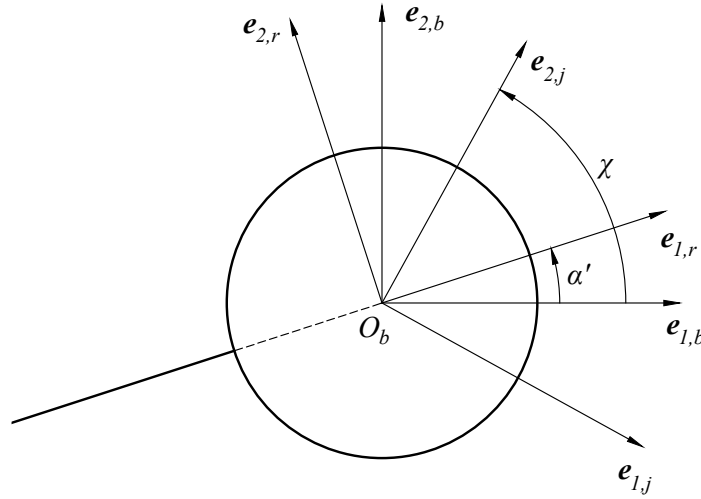
Figure 5.4: Reference systems reported on the bearing centre.

where $\boldsymbol{e}_{1,r}$ and $\boldsymbol{e}_{2,r}$ are the unit vectors of the reference system fixed in the bearing centre and with parallel and perpendicular axis with respect to the piston rod.

By projecting the journal reference system on the piston rod:

$$\begin{cases} \boldsymbol{e}_{1,j} = \cos{(\chi - \alpha')}\,\boldsymbol{e}_{1,r} + \sin{(\chi - \alpha')}\,\boldsymbol{e}_{1,r} \\ \boldsymbol{e}_{2,j} = \sin{(\chi - \alpha')}\,\boldsymbol{e}_{1,r} - \cos{(\chi - \alpha')}\,\boldsymbol{e}_{1,r} \end{cases} \qquad (5.26)$$

Thus, the axial and normal forces acting on the piston rod are:

$$\begin{cases} F_{a,r} = -F_t \cos{(\chi - \alpha')} + F_r \sin{(\chi - \alpha')} \\ F_{n,r} = -F_t \sin{(\chi - \alpha')} - F_r \cos{(\chi - \alpha')} \end{cases} \qquad (5.27)$$

where:

$F_{a,r}$ is the rod axial force (N); if positive, it tends to let the piston rod out of the sleeve;

$F_{n,r}$ is the rod normal force (N); if positive, it generates a tension of the piston rod inferior fibres.

Since the radial and tangential forces aren't applied at the bearing centre (see Figure 2.26 and Figure 3.2), different transportation moments are needed as function of the work condition:

$$M_{tras} = \begin{cases} -F_t\,e & \textit{for hydrodynamic condition} \\ -F_t\left(e + R_j\right) & \textit{for contact condition} \\ -F_{t,h}\,e - F_{t,c}\left(e + R_j\right) & \textit{for mixed condition} \end{cases} \qquad (5.28)$$

where $F_{t,h}$ and $F_{t,c}$ are the contributions to the tangential force respectively given by the hydrodynamic and contact models, when the system is working under mixed condition. The last action on the piston rod is given by the friction torque due to the movement of the journal into the lubricant:

$$T_{frict} = F_{frict}\,R_j \qquad \textit{for hydrodynamic and mixed conditions} \qquad (5.29)$$

As expressed by (5.29), the friction effect given by the lubricant under contact condition has been neglected because it is smaller than the friction generated by the contact between metals.

Both M_{tras} and T_{frict}, are positive if they generate a tension of the piston rod inferior fibres.

Chapter 6

Implementation and results

The numerical verification of the rod-end model has been performed after its implementation into a Electro-Hydraulic Servo-Actuator (EHSA) model developed by Politecnico di Torino and provided to me by my university tutor.

The EHSA considered in this work is a typical electrohydraulic primary flight control actuator and its reference architecture is shown in Figure 6.1.
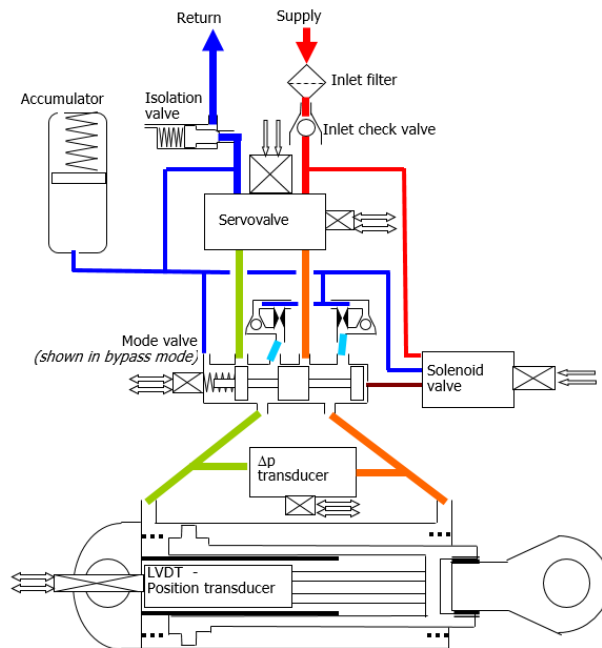

Figure 6.1:   EHSA reference architecture [30].

It is composed of the hydraulic and the control parts. The first consists of one electrohydraulic servo-valve and a linear hydraulic actuator. The servo-valve is of the jet pipe type and it is made up of two stages with the first stage receiving the current command as the input and using the torque motor in order to move the jet projector thus creating a pressure differential between the two sides of the second stage spool, which controls the flow to the hydraulic actuator. The control structure uses a linear position transducer as the feedback sensor for closed loop position control [30].

The position of a primary flight surface is generally controlled by more than one Electro-Hydraulic Servo-Actuator, thus two equal EHSAs, mounted in parallel, have been considered during the modelling. At the beginning of each flight, one EHSA is activated, while the other one is kept in standby mode, and it is activated in case of failure of the first one.

The double active-standby system was developed considering a mono-dimensional interconnection between the actuators and the controlled surface; therefore it is necessary to adapt the bi-dimensional results obtained in the previous chapters in order to ensure a good implementation of the rod-end, still maintaining the same configuration of the complete model.

The rod-end implementation into a mono-dimensional configuration is shown in Figure 6.2.
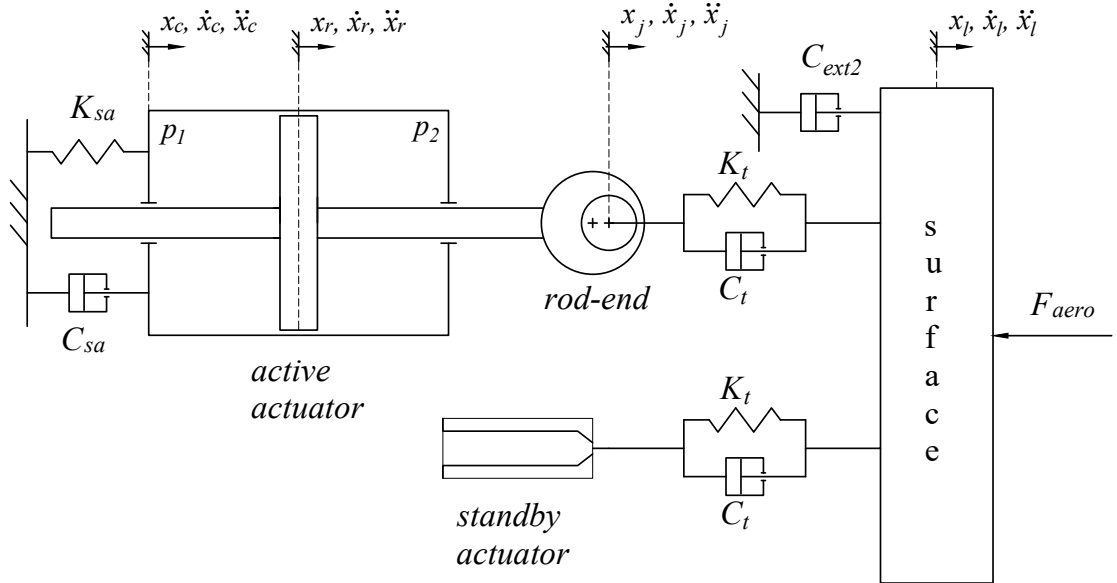
Figure 6.2: Connection between the EHSAs and the flight control surface.

The rod-end model has been implemented only on the active actuator line for two main reasons: the first one is because the active actuator balances almost by itself the aerodynamic load and the second one is to reduce the time needed by the simulator to execute the simulation.

The free body diagrams of the surface, piston and sleeve for the active actuator lead to following equilibrium equations.

For the piston:

$$m_r \ddot{x}_r + F_{frict\ p,s} = (p_1 - p_2)A_r + F_{a,r} \tag{6.1}$$

for the sleeve:

$$m_c \ddot{x}_c + C_{sa}\dot{x}_c + K_{sa}x_c + (p_1 - p_2)A_c = F_{frict\ p,s} \tag{6.2}$$

for the surface:

$$m_l \ddot{x}_l + C_t(\dot{x}_l - \dot{x}_j) + C_t(\dot{x}_l - \dot{x}_{r,s}) + C_{ext,2}\dot{x}_l + K_t(x_l - x_j) + \\ + K_t(x_l - x_{r,s}) + F_{areo} = 0 \tag{6.3}$$

where:

m_r, m_c, m_l	are, respectively, the piston rod, the sleeve and the surface masses (Kg);
A_r, A_c	are, respectively, the active piston areas of the piston and the sleeve (m²);
$F_{frict\ p,s}$	is the friction force generated between the piston and the sleeve (N);
K_{sa}, C_{sa}	are, respectively, the structural stiffness (N/m) and damping (Ns/m) coefficients;
K_t, C_t	are, respectively, the attachment surface stiffness (N/m) and damping (Ns/m) coefficients;
$C_{ext,2}$	is the damping coefficient associated to the driving mechanism of the surface (Ns/m);
F_{areo}	is the aerodynamic load (N).

Equations (6.1), (6.2) and (6.3) describe the linear actuator dynamic considering the following state variables relevant to the position:

- position of the flight control surface, x_l (m);

- position of the rod-end journal of the active actuator reported on the mono-dimensional configuration, x_j (m);

- positions of the actuator rods, x_r and $x_{r,s}$ (m);

- positions of the cylinders, x_c and $x_{c,s}$ (m).

For the standby actuator (whose parameters are characterized by the subscript $,s$) similar equations to (6.1) and (6.2) can be written.

Now, the correlation among $x_r, \dot{x}_r, \ddot{x}_r$ and $x_j, \dot{x}_j, \ddot{x}_j$ needs to be defined. This can be obtained analysing again the real bi-dimensional configuration of the mechanism, shown in Figure 5.3. In this configuration K_t and C_t represent the stiffness and damping coefficients between the link of length 's' and the controlled surface, due to the materials compliance. Thus, the equilibrium equation (6.3) describes the surface dynamic with respect to the link of length 's'.

As already said, the point 'P' represents the position of the journal and bearing centres under ideal conditions, whereas the point 'O' is the position of the journal centre in a generic real condition, which are respectively related to x_r and x_j in the mono-dimensional configuration.

The rod-end journal is connected to the link of length 's', thus the position, speed and acceleration of this link respect to its ideal conditions are expressed by $e_\gamma, \dot{e}_\gamma, \ddot{e}_\gamma$. Therefore, reporting these errors in the mono-dimensional case, the correlation between x_r and x_j is obtained:

$$x_j = x_r + s e_\gamma \tag{6.4}$$

By deriving equation (6.4):

$$\begin{cases} \dot{x}_j = \dot{x}_r + s \dot{e}_\gamma \\ \ddot{x}_j = \ddot{x}_r + s \ddot{e}_\gamma \end{cases} \tag{6.5}$$

Where $e_\gamma, \dot{e}_\gamma, \ddot{e}_\gamma$ are calculated using equations (5.15), (5.21) and (5.23).

97

In Figure 6.3, the rod-end model implementation into the Simulink environment of the EHSA complete model is shown. Since the control structure has not been modified by the rod-end implementation, this part is not displayed in the following figure.
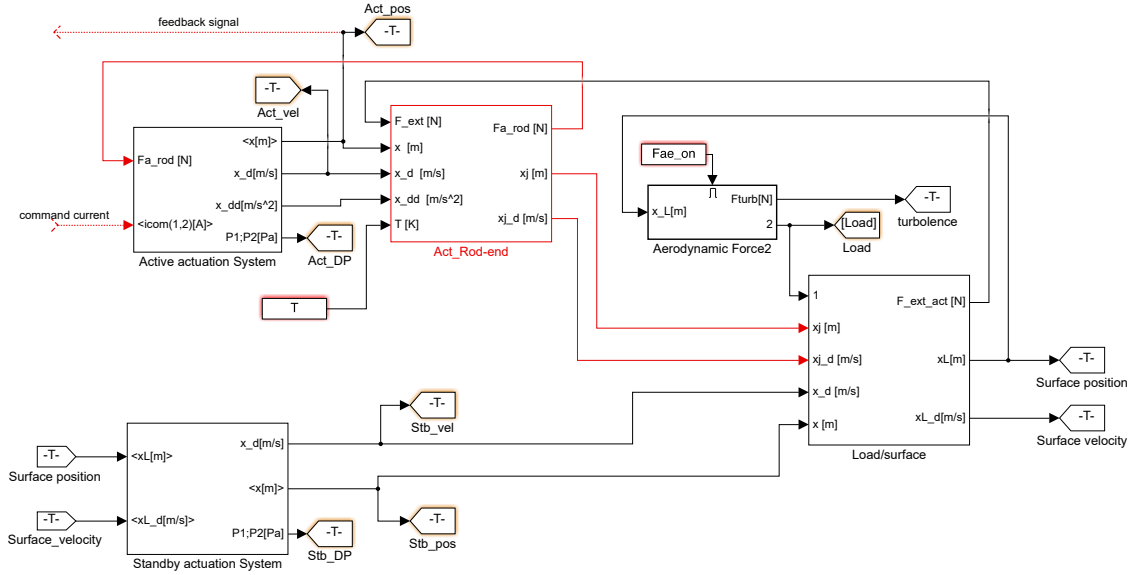

Figure 6.3:   Simulink implementation of the rod-end model.

Focusing on the active line, the actuation system gives the position of the actuator output rod, and its derivatives (equations (6.1), (6.2)), to the rod-end block which generates as output the position and speed of the journal reported on the mono-dimensional configuration and the axial force acting on the rod. The axial force is reported backwards as input for the actuation system, while the journal position and speed are given to the surface block along with the aerodynamic force and the position and speed of the standby actuator rod. The surface block solve equation (6.3) and gives the position and speed of the surface and the external force acting on the rod-end which is reported backwards to this block.

6.1 Numerical verification

The rod-end model numerical verification is carried out using the EHSA complete model and giving, as input, a square wave command. But first the geometric characteristics of the rod-end need to be defined. The rod-end choice was mainly made considering the EHSA rod diameter, which is equal to 0.0476 m.
The SI70ES female series rod-end from AST bearing has been chosen as reference rod-end. The values of interest are summarized in Table 6.1:

Data	Symbol, unit of measurement	Value
Width	L, [m]	0.049
Sphere/Journal radius	R_j, [m]	0.046
Clearance range	C, [μm]	65 - 165
Thread size	-	M56x4
Rod-end mass	m, [Kg]	8.3
Sphere/Journal mass	m_j, [Kg]	2

Table 6.1: Reference rod-end data (adapted from [42]).

In Figure 6.4 the response of the mathematical system to a square wave command with amplitude equal to 50% of the actuator stroke is displayed. The surface position is obtained for two values of clearance between the journal and the bearing in order to show the accuracy error generated by the rod-end.
The red line shows the surface position for a null value of the clearance, which represents the situation where the rod-end is replaced with an ideal joint. Meanwhile, the green line shows the surface position with a degraded rod end housing where, due to an anomalous wear, the clearance has reached 2 mm. Such a high value of internal free play, which is hardly obtainable in real rod-ends, has been chosen to clearly show the effects of the rod-end presence. As visible, the green line is clearly distanced from the red one leading to accuracy errors.
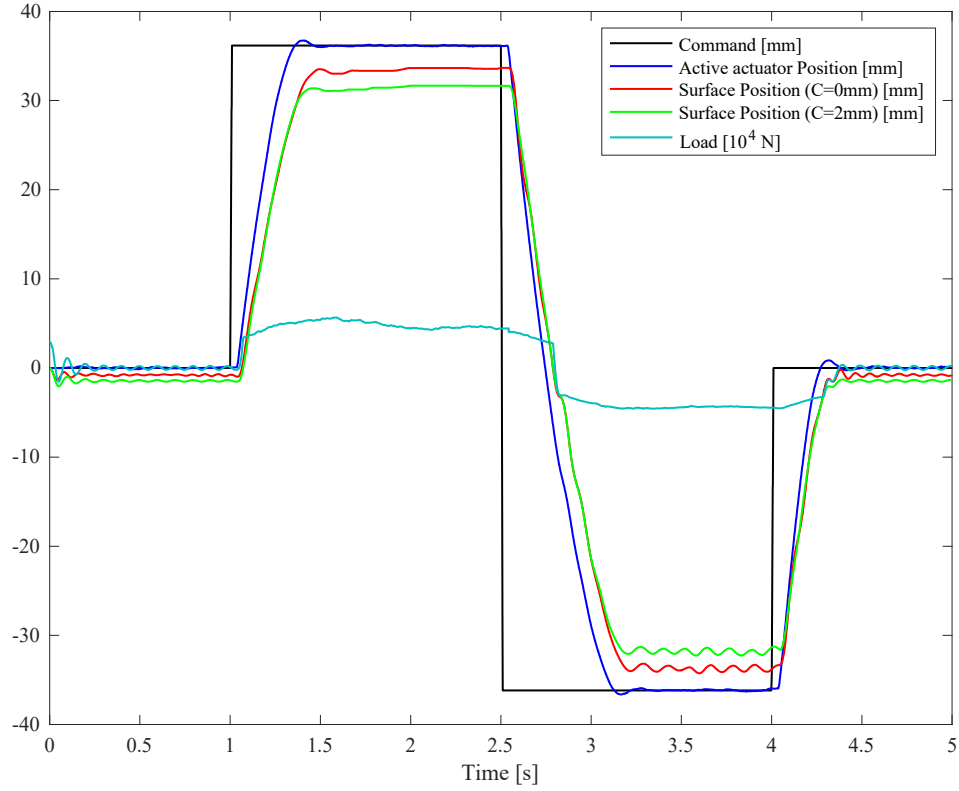
Figure 6.4:   System response to a square wave command.

The following figures express the degraded rod-end (clearance equal to 2 mm) behaviour. In Figure 6.5 the rod-end model inputs are displayed. Moving from the upper graph to the bottom one, we have the external force (F_{ext}) and its direction (φ) followed by the journal angular velocity (ω) and the temperature (T, which was kept equal to 20°C during the simulation). In Figure 6.6 and Figure 6.7 the journal centre trajectory is shown. To be more specific, in the first figure the cylindrical coordinates, radial position e and angular position χ, are shown separately, meanwhile, in the second, the coordinates are combined into a polar plot to better understand the journal trajectory with respect to the bearing centre. Moreover, the first graph of Figure 6.6 indicates the condition in which the rod-end model is working: 0 for hydrodynamic lubrication, 1 for mixed and 2 for contact.

Let's try to give an explanation to the trajectory displayed in Figure 6.7. Imagine to divide this figure in four quadrants: the first one in the upper right side, the second in the upper left side, the third in the lower left side and the fourth in the lower right side.

The simulation starts with the following set of initial values: e=0.001m and χ=30°.

When the command is zero the aerodynamic load generates an oscillation of the controlled surface (Figure 6.4) which leads to an oscillation of the rod-end external force, even if it is not noticeable in Figure 6.5 because of the scale of the graph. The external force direction φ, which was defined starting from the vertical line (Figure 2.8 and equation (5.25)), remains constant (around 110°) because the piston rod doesn't move.

In this phase, the journal centre moves from the fourth to the third quadrant due to a variation of the angular position χ, which is also defined starting from the vertical line and positive if counter clockwise (Figure 2.8). Maintaining an angular position equal to -70°, the journal centre oscillates along the radial direction due to the external force. This oscillation, of amplitude approximately equal to 1 mm, has an impact on the initial surface vibration (green line in Figure 6.4).

When the positive command signal arrives, the external force becomes negative meaning that piston rod will be forced inside the actuator sleeve by the journal. The force direction increases up to 130° because of the mechanics configuration variation (Figure 5.1 and equation (5.25)). The journal is pressed against the bearing surface in the third quadrant. The system switches from a hydrodynamic lubrication to a mixed work condition. Due to the external force direction variation, the journal angular position has a slight increase up to -50°. The system reaches and maintains a stationary condition, where $e \approx 0.002$ m and $\chi \approx$ -50°, till 2.5 s.

At 2.5 seconds the command switches instantaneously from +50% to -50% of the actuator stroke. The external force has a strong increase becoming positive, which means that piston rod tends to be pulled out from the actuator sleeve by the journal. The mechanism configuration changes again causing an external force direction reduction (till 90°). The journal centre moves from the third to the first quadrant. As shown in Figure 6.6, the radial position e decreases, the journal passes close to the bearing centre, the angular position has a variation of 180° (reaching 130°) and then the journal moves away from the bearing centre. This transitory phase generates work condition variations: form mixed to hydrodynamic and then to mixed again. Thus, the system reaches another stationary condition, where $e \approx$ 0.002 m and $\chi \approx 95$°.

At 4 seconds the command returns to zero. When the piston rod starts moving, the external force becomes negative and its direction increases up to 110° (due to the mechanism configuration variation). Thus, the journal is pushed by these external conditions from the first to the third quadrant. The work condition passes form mixed to hydrodynamic and to mixed again. About the radial (e) and angular (χ) positions, the same consideration as above can be made. When the piston rod reaches the command value, the rod-end system returns in hydrodynamic lubrication condition. Like the first phase, the aerodynamic load

101

generates an oscillation on the journal radial position e, while the angular position χ is around -70°.

In Figure 6.5, the journal angular velocity around its centre (ω) is also displayed. As visible, this parameter is noticeably different from zero during the transitory phases, i.e. when the command changes and, thus, the mechanism configuration is varying. The short range of variation of the journal angular velocity makes the hydrodynamic lubrication effect mainly due to the squeezing action, which relates the radial journal motion with the generation of load carrying capacity in the lubricant film. The wedge action, which relates the relative surface velocity to the hydrodynamic pressure generation capacity, is secondary.

In Figure 6.8 the forces acting on the journal are shown. The radial, tangential and frictional forces reach the highest values during transitory phases and in mixed work condition. When the system works in hydrodynamic lubrication condition these forces are way lower, meaning that the hydrodynamic pressure distribution struggle to support the external load. The friction force in hydrodynamic lubrication condition is almost zero, while in mixed condition it increases up to 5000 N. The friction force is proportional to the tangential force (equation (3.6)), this explains why the two graphs have the same trend.

In Figure 6.9 the actions on the piston rod are displayed. $F_{a,rod}$ represents the force parallel to the piston rod axis, while $F_{n,rod}$ is the force acting in the perpendicular direction. M_{rod} is the concentrated torque at the end of the piston rod. Since this torque is mainly given by the friction effect, it has the same trend of F_{frict} in Figure 6.8.

In Figure 6.10 the pressure distribution acting on the journal at t=0.001 s is shown.
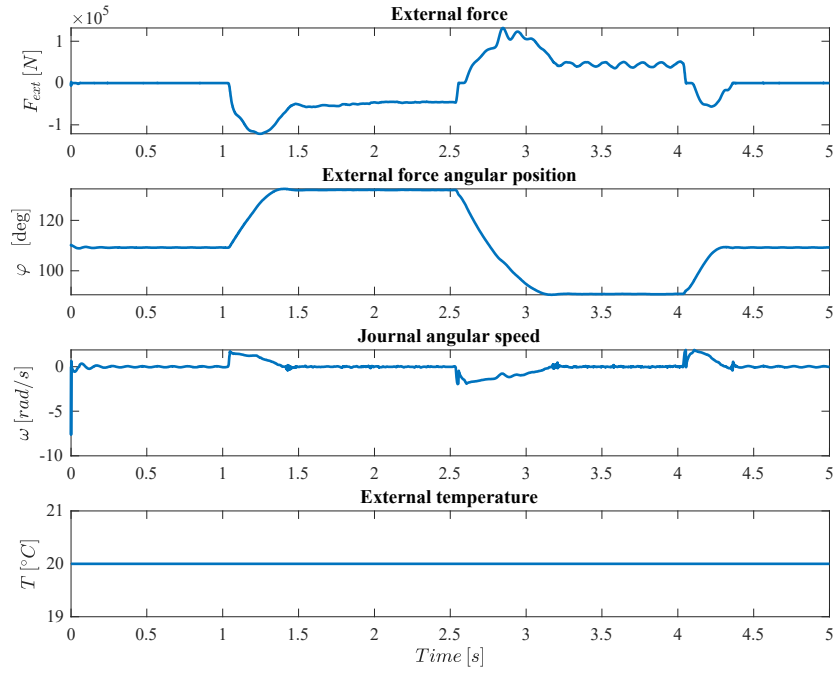
Figure 6.5:   Rod-end model inputs.
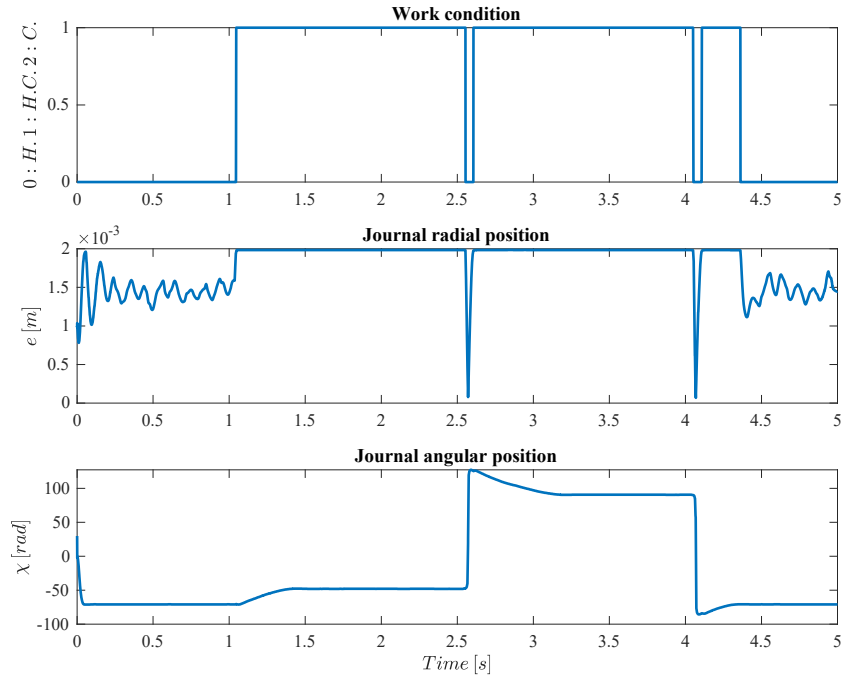
Figure 6.6:   Journal trajectory (separated variables).

103
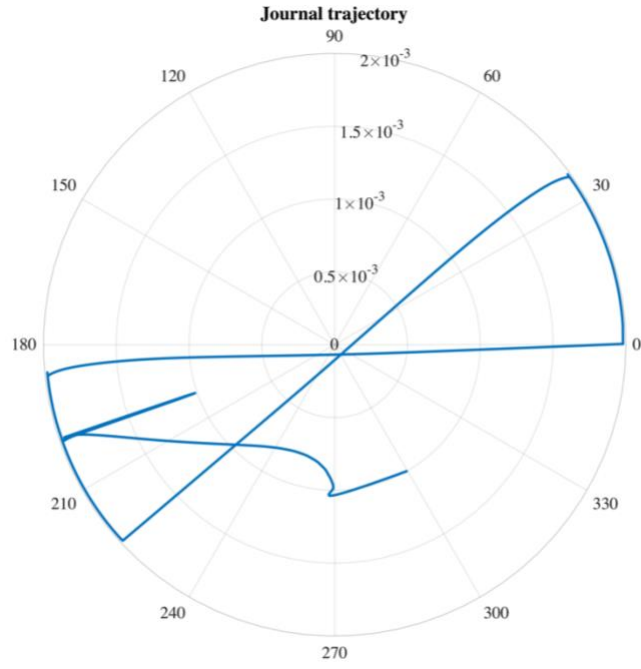
Figure 6.7: Journal trajectory (united variables).
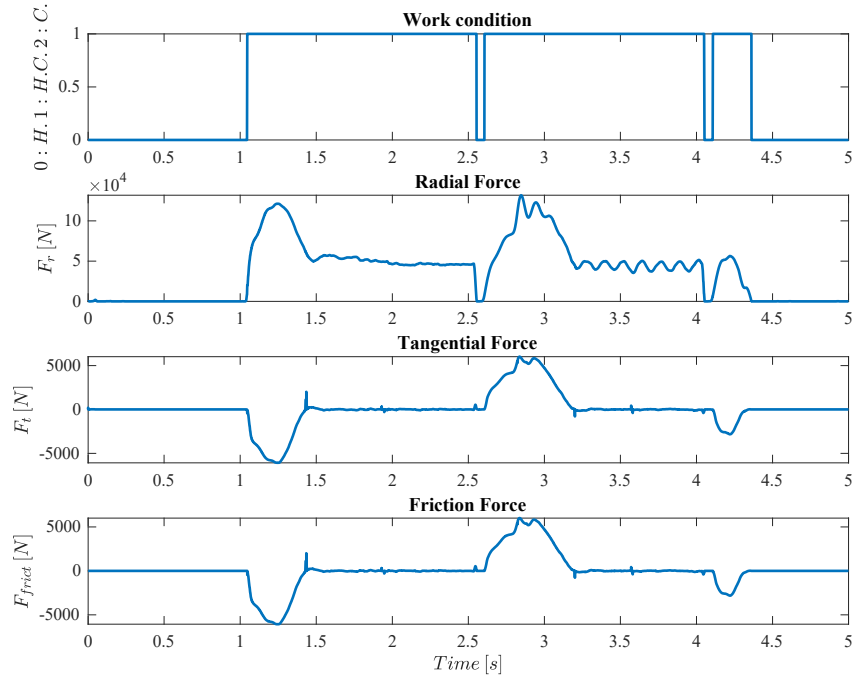

Figure 6.8: Forces acting on the journal.
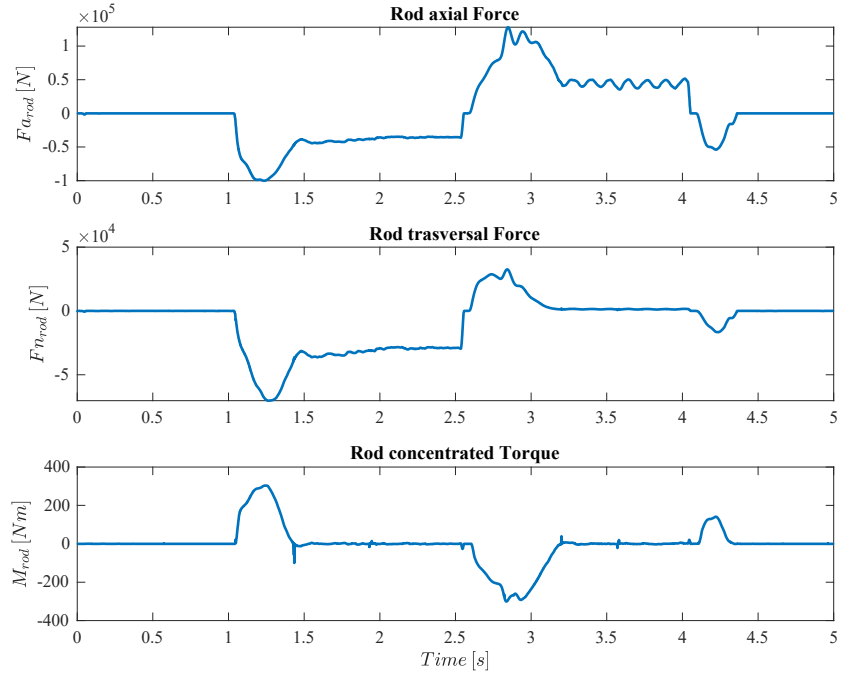
Figure 6.9:   Torque and forces acting on the piston rod.
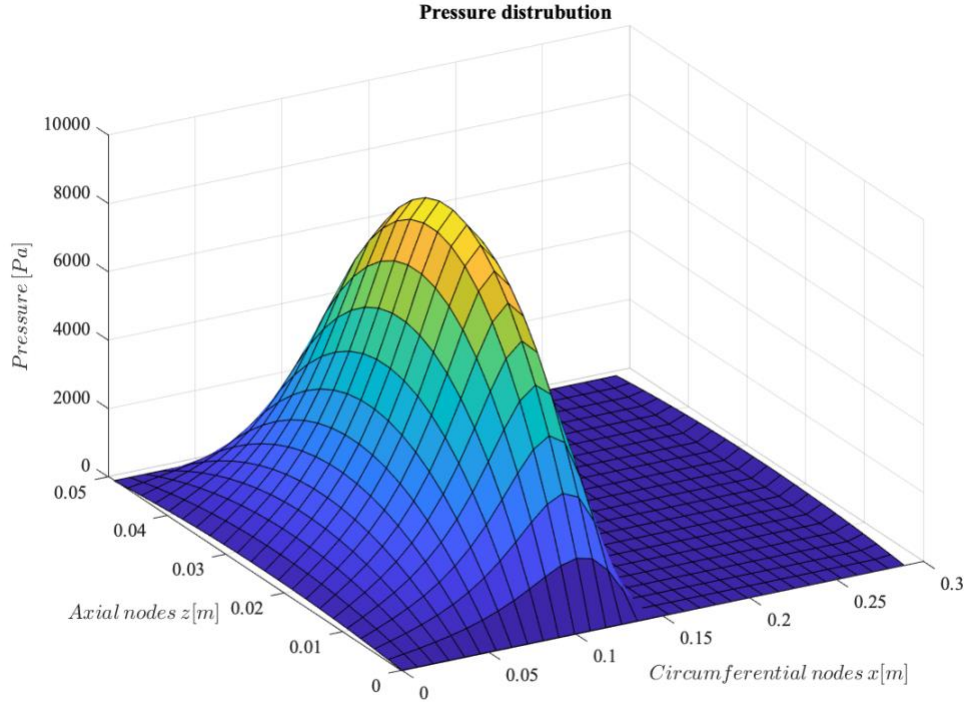
Figure 6.10:   Pressure distribution at t= 0.001 s.

6.2   Lubricant degradation effects

In this subchapter the effects of the lubricant degradation are analysed. The lubricant degradation, which is usually caused by the oil oxidation, leads to a reduction of viscosity. Therefore, a simple lubricant health coefficient has been introduced in the rod-end model. Three simulations have been carried out: the first one with lubricant health at 100% (blue line), the second at 80% (red line) and the third at 60% (yellow line). All tests are preformed considering a rod-end clearance of 0.002 m and giving to the EHSA mathematical model the exact square wave command previously exposed.

The lubricant degradation effects are visible on the radial, tangential and frictional forces acting on the journal (Figure 6.11) and, thus, on the actions developed at the end of the piston rod (Figure 6.12).

The lubricant degradation causes a reduction on the load carrying capacity given by the hydrodynamic effect. Thus, as the lubricant degradation increases, the mixed and contact work conditions will be more easily accessible by the system, as visible from the first graph in Figure 6.11.

Since the hydrodynamic support is reduced, more asperities of journal and bearing surfaces will enter in contact. This leads to a penetration increment and, thus, to a general increase of maximum values of radial, tangential and frictional forces (Figure 6.11).

The actions displayed in Figure 6.12 represent the journal forces reported on the bearing, along the parallel and perpendicular directions of the piston rod axis. Therefore, a general increment of these actions is expected too, as visible in Figure 6.12.
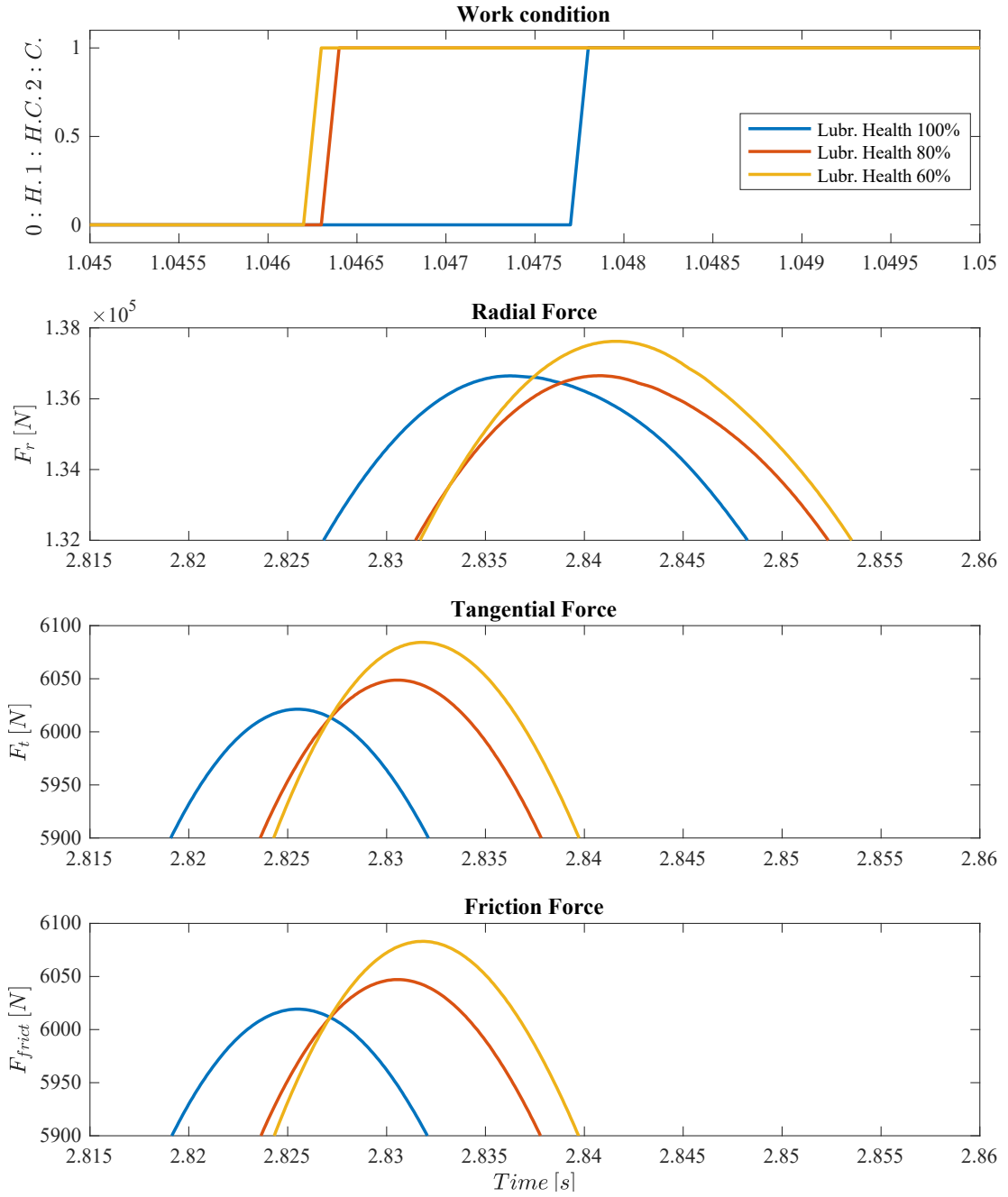
Figure 6.11: Lubricant degradation effects on the forces acting on the journal.
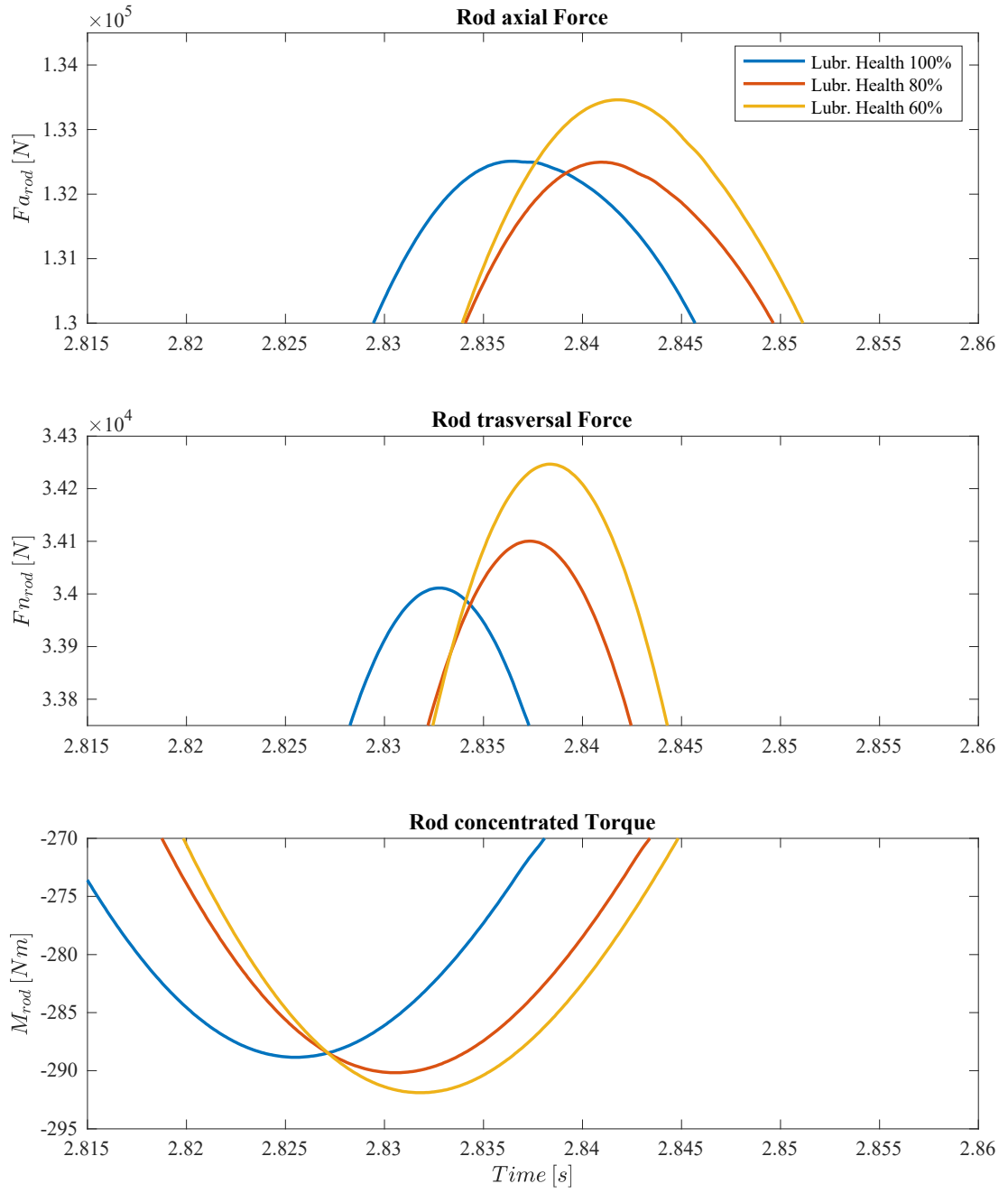
Figure 6.12: Lubricant degradation effects on the actions at the end of the piston rod.

Chapter 7

Conclusions and future works

The rod-end is a critical component of flight control servo-actuators. Its failure would compromise the aircraft stability forcing the pilot to an emergency landing or causing even worse scenarios. For these reasons, rod-ends are well-suited components for CBD/PHM applications. An essential tool, in such direction, is a high-fidelity mathematical model to perform simulations of the component behaviour. The goal of this work is the realization of that model.

   Three different work conditions, and, consequently, three different Simulink blocks, have been considered as main body of the model: hydrodynamic lubrication, contact and a mixed hydrodynamic-contact conditions. In order to provide the external force direction and the relative speed between the journal and bearing surfaces, the kinematic of a reference mechanism, that allows the connection between the actuator to the controlled surface, has been implemented.
The model requires as input the position of the piston rod and its derivatives, the temperature and the external force acting on the journal. The model, considering the journal position with respect to the bearing centre, realizes in which condition the system is working on and activates the correct block. As output, the model is able to give the position of the journal with respect to the bearing centre in cylindrical coordinates (and relative derivatives), the forces acting on the journal, the pressure distribution and the actions on the bearing along the piston rod parallel and perpendicular directions.
Then, the rod-end model has been adapted to make it suitable for the mono-dimensional EHSA complete model where it needed to be implemented.

The model numerical stability has been verified using a square wave command as input for the EHSA model. This simulation has also shown the accuracy error produced on the controlled surface by an anomalous value of the rod-end clearance.

The lubricant degradation simulation has allowed to see the increment of the friction force and, thus, an increase of those actions which tend to bend the piston rod.

The rod-end model has proved to be a valid tool to simulate the effects of a degraded rod-end, in terms of:

- excessive free play between the internal components due to an anomalous wear;

- undesired forces increase due to lubricant degradation;

- crack propagation on the rod-end body, where the pressure distribution can be used as input for this purpose.

Since the rod-end configuration is independent from the actuator type, the model can be implemented not only on Electro-Hydraulic Servo-Actuator (EHSA) models, but also on other families like electromechanical actuators (EMA), which are also used in airspace field. Therefore, the model can be used for future CBD/PHM applications. Next steps consist in:

1. execution of detailed analysis of rod-ends degradation and development of models which relate each fault to the variation of physical system parameters, thus:

   - wear – clearance increment model;
   - crack – body stiffness reduction model;
   - lubricant degradation – friction force increment model.

   As proven previously, the rod-end model is already able to show the last relation with the introduction of a simple lubricant health coefficient. The rod-end model cloud also be interfaced with a second approximation model of the actuator in order to evaluate the effects of friction force increment on the rod deformation and, thus, on the piston rod seals;

2. execution of *feature(s)* selection for each of the fault modes addresses. *Features* represents those characteristic parameters, detectable by the system sensors, which express whether the system is healthy or not;

3. execution of *Fault Detection and Identification (FDI)* by comparing the current faulty feature distribution with the reference healthy conditions. According to the origin of these conditions two main approaches can be followed: *data-driven* or *model based.* Respectively, the reference conditions are obtained through a predefined baseline or as outputs of a physical model. When the two distributions differ from each other by a threshold confidence level the fault is "detected";

4. execution of failure prognosis through two sequential steps, prediction and filtering. The prediction uses a fault/degradation model to estimate the failure probability, or *probability density function (pdf),* for the next instant of time. Particle filtering is then used for the estimation of the *Residual Useful Life (RUL);*

5. execution of a prognostics performance algorithm to obtain the prognostic routine level of confidence.

Another goal of this CBD/PHM study for rod-end, in addition to those referred in the introduction chapter, is to point out those extra sensors, which are not usually installed on flight control actuators, that allow the determination those *features* (point 2) which are not detectable through the standard onboard sensors. The information would be very useful for those companies that intend to actually implement a prognostic system on their aircraft.

Considering the rod-end model, a further improvement could be realized in order to get closer to the real system. Instead of modeling the component as a journal bearing, the curvature of the internal elements, respect to a plane which contains the sphere boring axis, can be implemented. However, this improvement would make the Reynolds equation numerical integration quite harder.
This model would lead to an enhanced CBD/PHM system and could be used to predict the effect of potential misalignments between the sphere boring and housing axis on the piston rod - rodend threaded connection.

Appendix A: Newtonian lubricant assumption

The Newtonian lubricant assumption deals with the correlation between the stress and the deformation. A given constitutive formula may be good for a large group of fluids, but one general formula cannot describe all fluids. The simplest relation is a linear equation: the stress is proportional to the rate of strain (Newton's viscosity law).
At ordinary pressures and temperatures all gases obey these relations, as do many simple liquids. Liquids made up of complex molecules, liquid mixtures, and slurries of fine particles in a liquid do not obey linear relations and are said to be non-Newtonian [6].
The idea of a linear relation between stress and rate of strain was first put forward by Newton, and for this reason the viscosity law bears his name. Much later, George S. Stokes (English mathematician, 1819–1903) and C. L. M. H. Navier (French engineer, 1785–1836) produced the exact equations that govern the flow of Newtonian fluids [6].

Consider two flat surfaces separated by a layer of fluid of thickness 'h', as shown in Figure A.1.
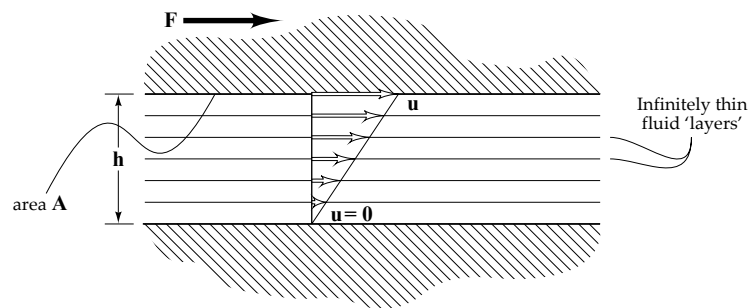
Figure A.1:   Schematic representation of the fluid separating two surfaces [3].

The force required to move the upper surface is proportional to the wetted area 'A' and the velocity 'u':

$$F \propto A * u \tag{A.1}$$

Assume that the fluid film separating the surfaces is made up of a number of infinitely thin layers. Compare now two fluid films of different thickness made up of equispaced layers. If the surface velocity remains unchanged in these two cases, then a single layer in the thicker film will undergo less relative sliding than in the thinner film. The velocity gradients for these two layers will be different. Since the thicker film contains more single layers, less force will be needed to shear a single layer so the viscous resistance will vary as the reciprocal of the film thickness '1/h' [3].
The force needed to move the upper surface is thus proportional to:

$$F \propto A * u/\text{h} \tag{A.2}$$

The proportionally constant is different for different fluids and it is called "dynamic viscosity μ". The SI unit for dynamic viscosity is Pascal-second (Pas).

$$F = \mu * A * u/\text{h} \tag{A.3}$$

Rearranging gives:

$$\tau = \mu \frac{u}{h} = \mu \frac{\partial u}{\partial z} \tag{A.4}$$

where:

μ is the dynamic viscosity (Pas);
τ is the shear stress acting on the fluid (Pa);
u/h is the shear rate, i.e. velocity gradient normal to the shear stress (s^{-1}).

By considering a 'z' axis vertically directed in Figure A.1, equation (A.4) can be rewritten as in (2.7):

$$\tau = \mu \frac{\partial u}{\partial z} \tag{A.5}$$

Appendix B: MATLAB scripts

Reynolds equation integration

The Reynolds equation is solved using a function which needs as input the lubricant conditions, the discretization parameters, the geometrical characteristics and dynamic data of the rod-end and gives as output the pressure distribution matrix.

```matlab
xa = 0; xb = pi*2*Rj;      % initial and final coordinate long x-axis
za = 0; zb = L;            % initial and final coordinate long z-axis
n = 8;                     % internal nodes number long z-axis
m = 11;                    % internal nodes number long x-axis (it MUST be an odd number)


x = linspace(xa,xb,m+2).';              % column vector of  x-nodes
delta_x = (xb-xa)/(m+1);                % x-range
xI = (x(2:end)+x(1:(end-1)))/2;         % column vector x/2-nodes


z = linspace(za,zb,n+2).';              % column vector of  z-nodes
delta_ = (zb-z)/(n+1);                  % z-range
zI = (z(2:end)+z(1:(end-1)))/2;         % column vector x/2-nodes


function [P_distr, p_Vogel_in] =...
Reynolds(omega,T,Rj,C,a,b,c,m,x,delta_x,xI,n,z,delta_z,zI,e,e_d,chi_d, ...
C_health_lub,p_Vogel_in)

%%%%%%% parameters %%%%%%%
epsilon = e/C;           % eccentricity ratio [/]
epsilon_d = e_d/C;       % eccentricity ratio derivative [1/s]
mu0 =  a*exp(b/(T-c));   % pressure independent viscosity [Pa*s]
alpha = (0.6+0.965*log10(mu0*(10^3)))*10^(-8);    % pressure-viscosity coefficient
(Wooster) [m^2/N]
mu = C_health_lub *mu0*exp(alpha*p_Vogel_in);     % dynamic viscosity [Pa*s]


%%%%%%% coefficient matrix and known term calculation if epsilon_d >= 0 %%%%%%%
if (epsilon_d >= 0)
lambda_FH = @(z,x) 1/mu*(C*(1+epsilon*cos(x/Rj)))^3;     % lambda=h^3/mu
[m^3/(Pa*s)](equations (2.26) (2.36))
f_FH = @(z,x) 6*((2*chi_d-omega)*(C*epsilon*sin(x/Rj))+2*C*epsilon_d*cos(x/Rj));     %
known term [m/s](equation (2.36))
```

```matlab
%%%%%%%% vectors a_q-1 and a_q+1 %%%%%%%%
A_q_1 = zeros(length(z)-2,length(xI));                   % matrix initialization
for k = [2:length(z)-1]                                  % moving on z-nodes
    for i = [1:length(xI)]                               % moving on xI-nodes
        A_q_1(k-1,i) = lambda_FH(z(k),xI(i))/(delta_x)^2;    % second or fourth equation
        of (2.48)
    end
end
% vectors composition considering boundaries conditions (Table 2.4) using the previous
matrix
a_q_m1 = zeros(1,n*m).';                                  % vector a_q+1 initialization
a_q_p1 = zeros(1,n*m).';                                  % vector a_q-1 initialization
qm=1;                                                     % counter
qp=1;                                                     % counter
for k = [1:length(z)-2]                                   % moving on z-nodes
    for i = [1:length(xI)]                                % moving on xI-nodes
        if ((k==1 && i==1) || (k~=(length(z)-2) && i==length(xI)))        % for those weak
        nodes where a_q+1 component needs to be set to zero
        qm=qm;
        a_q_p1(qp) = 0;
        qp=qp+1;
        else if ((k==(length(z)-2) && i==length(xI)) || (k~=1 && i==1))  % for those weak
        nodes where a_q-1 component needs to be set to zero
        a_q_m1(qm) = 0;
        qm=qm+1;
        qp=qp;
        else           % for strong nodes
        a_q_m1(qm) = A_q_1(k,i);
        qm=qm+1;
        a_q_p1(qp) = A_q_1(k,i);
        qp=qp+1;
        end
        end
    end
end


%%%%%%%% a_q-m and a_q+m coefficients %%%%%%%%
A_q_m = zeros(length(zI),length(x)-2) ;                  % matrix initialization
for k = [1:length(zI)]                                   % moving on zI-nodes
    for i = [2:length(x)-1]                              % moving on x-nodes
        A_q_m(k,i-1) = lambda_FH(zI(k),x(i))/(delta_z)^2;   % first or fifth equation of
        (2.48)
    end
end
% vectors composition considering boundaries conditions (Table 2.4) using the previous
matrix
a_q_mm = zeros(1,n*m).';                                  % vector a_q+m initialization
a_q_pm = zeros(1,n*m).';                                  % vector a_q-m initialization
qm=1;                                                     % counter
qp=1;                                                     % counter
for k = [1:length(zI)]                                    % moving on zI-nodes
    for i = [1:length(x)-2]                               % moving on x-nodes
        if (k==1)                                                  % for those weak
        nodes where a_q+m component needs to be set to zero
        qm=qm;
        a_q_pm(qp) = 0;
        qp=qp+1;
        else if (k==(length(zI)))                                  % for those weak
        nodes where a_q-m component needs to be set to zero
        a_q_mm(qm) = 0;
        qm=qm+1;
        qp=qp;
        else              % for strong nodes
        a_q_mm(qm) = A_q_m(k,i);
```

```matlab
            qm=qm+1;
            a_q_pm(qp) = A_q_m(k,i);
            qp=qp+1;
        end
        end
    end
end

%%%%%%%% a_q coefficients %%%%%%%%
A_q = zeros(length(z)-2,length(x)-2);                     % matrix initialization
for k = [2:length(z)-1]                                   % moving on z-nodes
    for i = [2:length(x)-1]                               % moving on x-nodes
        A_q(k-1,i-1) = -(lambda_FH(z(k),xI(i-1))/(delta_x)^2+ ...   % third equation of
                        lambda_FH(z(k),xI(i))/(delta_x)^2+ ...      % (2.48)
                        lambda_FH(zI(k-1),x(i))/(delta_z)^2+ ...
                        lambda_FH(zI(k),x(i))/(delta_z)^2);
    end
end
a_q =reshape(A_q.',1,(length(z)-2)*(length(x)-2)).';      % the previous
matrix in reshaped as a vector

%%%%%%%% coefficient matrix A %%%%%%%%
B = [a_q,a_q_m1,a_q_p1,a_q_mm,a_q_pm];
A = spdiags(B,[0,-1,+1,-m,+m],n*m,n*m);

%%%%%%%% known term f %%%%%%%%
F_i = zeros(length(z)-2,length(x)-2);                     % matrix initialization
for k = [2:length(z)-1]                                   % moving on z-nodes
    for i = [2:length(x)-1]                               % moving on x-nodes
        F_i(k-1,i-1) = f_FH(z(k),x(i)) ;
    end
end
f = reshape(F_i.',1,(length(z)-2)*(length(x)-2)).';       % the previous matrix in
reshaped as a vector

%--------------------------------------------------------------------------------------%
%%%%%%%% coefficient matrix and known term calculation if epsilon_d < 0 %%%%%%%%
else
lambda_FH = @(z,x) 1/mu*(C*(1-epsilon*cos(x/Rj)))^3; % lambda (equation (2.58))
f_FH = @(z,x) 6*((omega-2*chi_d)*(C*epsilon*sin(x/Rj))-2*C*epsilon_d*cos(x/Rj)); % known
term (equation (2.60))

%%%%%%%% a_q-1 and a_q+1 coefficients %%%%%%%%
A_q_1 = zeros(length(z)-2,length(xI));
for k = [2:length(z)-1]
    for i = [1:length(xI)]
        A_q_1(k-1,i) = lambda_FH(z(k),xI(i))/(delta_x)^2;
    end
end
a_q_m1 = zeros(1,n*m).';
a_q_p1 = zeros(1,n*m).';
qm=1
for i = [1:length(xI)]
    if ((k==1 && i==1) || (k~=(length(z)-2) && i==length(xI)))
            qm=qm;
        a_q_p1(qp) = 0;
        qp=qp+1;
        else if ((k==(length(z)-2) && i==length(xI)) || (k~=1 && i==1))
        a_q_m1(qm) = 0;
        qm=qm+1;
        qp=qp;
        else
```

116

```matlab
            a_q_m1(qm) = A_q_1(k,i);
            qm=qm+1;
            a_q_p1(qp) = A_q_1(k,i);
            qp=qp+1;
            end
            end
    end
end
%%%%%%% a_q-m and a_q+m coefficients %%%%%%%
A_q_m = zeros(length(zI),length(x)-2);
for k = [1:length(zI)]
    for i = [2:length(x)-1]
        A_q_m(k,i-1) = lambda_FH(zI(k),x(i))/(delta_z)^2;
    end
end
a_q_mm = zeros(1,n*m).';
a_q_pm = zeros(1,n*m).';
qm=1;
qp=1;
for k = [1:length(zI)]
    for i = [1:length(x)-2]
        if (k==1)
        qm=qm;
        a_q_pm(qp) = 0;
        qp=qp+1;
        else if (k==(length(zI)))
        a_q_mm(qm) = 0;
        qm=qm+1;
        qp=qp;
        else
        a_q_mm(qm) = A_q_m(k,i);
        qm=qm+1;
        a_q_pm(qp) = A_q_m(k,i);
        qp=qp+1;
        end
        end
    end
end


%%%%%%% a_q coefficients %%%%%%%
A_q = zeros(length(z)-2,length(x)-2);
for k = [2:length(z)-1]
    for i = [2:length(x)-1]
        A_q(k-1,i-1) = -(lambda_FH(z(k),xI(i-1))/(delta_x)^2+ ...
        lambda_FH(z(k),xI(i))/(delta_x)^2+ ...
        lambda_FH(zI(k-1),x(i))/(delta_z)^2+ ...
        lambda_FH(zI(k),x(i))/(delta_z)^2);
    end
end
a_q =reshape(A_q.',1,(length(z)-2)*(length(x)-2)).';

%%%%%%% coefficient matrix A %%%%%%%
B = [a_q,a_q_m1,a_q_p1,a_q_mm,a_q_pm];
A = spdiags(B,[0,-1,+1,-m,+m],n*m,n*m);

%%%%%%% inown term f%%%%%%%
F_i = zeros(length(z)-2,length(x)-2);
for k = [2:length(z)-1]
    for i = [2:length(x)-1]
        F_i(k-1,i-1) = f_FH(z(k),x(i));
    end
end
f = reshape(F_i.',1,(length(z)-2)*(length(x)-2)).';
end
```

117

```matlab
%%%%%%% resolution  %%%%%%%
p_i = A\f;                                              % solution of equation system
P = zeros(length(z),length(x));                         % matrix initialization
qP=1;                                                   % counter
for k = [1:length(z)]                                   % moving on z-nodes
    for i = [1:length(x)]                               % moving on x-nodes
        if (k==1 | i==1 | k==length(z) | i==length(x))  % nodes lying on boundaries
        qP=qP;
        else
        P(k,i)=p_i(qP);                                 % internal nodes
        qP=qP+1;
        end
    end
end


%%%%%%% half-Sommerfeld boundary condition %%%%%%%
for k = [1:length(z)]
    for i = [1:length(x)]
        if P(k,i)<0                                     % if the pressure is negative,
        P(k,i)=0;                                       % its value set to zero
        end
    end
end


%%%%%%% matrix reshape if epsilon_d < 0 figure 2.18 %%%%%%%
P_distr = zeros(length(z),length(x));                   % pressure distribution
if(epsilon_d >= 0)
   P_distr = P;
   else
     for i = [length(x)/2+0.5:length(x)]
     P_distr(:,i-(length(x)/2-0.5)) = P(:,i);
     end
     for i = [2:length(x)/2+0.5]
     P_distr(:,i+(length(x)/2-0.5)) = P(:,i);
     end
end


%%%%%%% pressure value for Vogel Barus viscosity equation %%%%%%%
p_max=max(max(P_distr));  % maximum pressure
p_min=min(min(P_distr));  % minimum pressure
p_mean=(p_max+p_min)/2;   % mean pressure
if p_mean<=1e7            % the pressure value is limited to avoid numerical instability
   p_Vogel_out = p_mean;
   else
   p_Vogel_out = 1e7;
end
```

Hydrodynamic pressure integration

The numerical integration trapezoidal rule is applied in a Matlab function to obtain the radial, the tangential and frictional forces.

```matlab
function [Fr,Ft,Ff,Freac,PHi_Freac] = P_integration(x,z,Rj,P_distr)

%%%%%%% Hydrodynamic Fluid force and attitude angle using the trapezoidal rule %%%%%%%
DpDx= zeros(length(z),length(x));                 % matrix initialization
for k = [1:length(z)]                             % moving on z-nodes
    for i = [2:length(x)]                         % moving on x-nodes
        DpDx(k,i)= (P_distr(k,i)-P_distr(k,i-1))/2;    % pressure derivative along x-axis
    end
end
h_FH = @(z,x) C*(1+epsilon*cos(x/Rj));       % film thickness
cos_FH = @(z,x) cos(x/Rj);                   % cos(x/RJ)
sin_FH = @(z,x) sin(x/Rj);                   % sin(x/RJ)


sum_z_cos = zeros(1,length(x));              % vector for Fr
sum_z_sin = zeros(1,length(x));              % vector for Fr
sum_z_Ff = zeros(1,length(x));               % vector for Ff

% equations (2.77) and (2.78)
for i = [1:length(x)]                        % moving on x-nodes
    sum_z_cos(i)=0;
    sum_z_sin(i)=0;
    sum_z_Ff(i)=0;
    for k = [2:length(z)]                    % moving on z-nodes
        sum_z_cos(i) = sum_z_cos(i)+(P_distr(k-1,i)* ...
        (-cos_FH(z(k-1),x(i))))+(P_distr(k,i)*(-cos_FH(z(k),x(i))));
        sum_z_sin(i) = sum_z_sin(i)+(P_distr(k-1,i)* ...
        sin_FH(z(k-1),x(i)))+(P_distr(k,i)*sin_FH(z(k),x(i)));
        sum_z_Ff(i) = sum_z_Ff(i)+(h_FH(z(k),x(i))/2*DpDx(k,i)+ ...
        (omega*Rj+e_d*sin_FH(z(k),x(i))-e*chi_d*cos_FH(z(k),x(i)))*mu/h_FH(z(k),x(i)));
    end

    sum_z_cos(i) = sum_z_cos(i)*0.5*delta_z;
    sum_z_sin(i) = sum_z_sin(i)*0.5*delta_z;
    sum_z_Ff(i) = sum_z_Ff(i)*0.5*delta_z;
end


Fr = 0;
Ft = 0;
Ff = 0;
for i = [2:length(x)]
    Fr = Fr+sum_z_cos(i-1)+sum_z_cos(i);
    Ft = Ft+sum_z_sin(i-1)+sum_z_sin(i);
    Ff = Ff+sum_z_Ff(i-1)+sum_z_Ff(i);
    end


Fr = Fr*0.5*delta_x;                         % radial force
Ft = Ft*0.5*delta_x;                         % tangential force
Ff = Ff*0.5*delta_x;                         % friction force


Freac = sqrt(Fr^2+Ft^2);                     % reaction fluid force
PHi_Freac = abs(atan(Ft/Fr));                % fluid attitude angle
```

119

Contact pressure field

The following Matlab function contains the Hertz theory equations for the pressure distribution in contact conditions.

```matlab
function P = Contact_pressure_distribution(F_cont,x,z,L,Rb,Rj,nu_b,nu_j,E_b,E_j)


h_wid = sqrt((F_cont*(((1-nu_j^2)/(E_j))+((1-nu_b^2)/(E_b))))/(pi*L*((1/Rj)-(1/Rb)))); %
half width contact area (equation (3.16))


P_FH = @(z,x_r) 2*F_cont/(pi*L*h_wid)*sqrt(1-(x_r/h_wid)^2); %  pressure distribution
function handle (equation (3.17))
P = zeros(length(z),length(x));                     % Pressure matrix initialization


% double for loop to fill the pressure matrix
for i = [1:length(z)]                               % moving on z-nodes
    for j = [1:length(x)]                           % moving on x-nodes
        if (abs(pi*Rj-x(j))) <= h_wid
        P(i,j) = P_FH(z(i),abs((pi*Rj)-x(j)));
        else
        P(i,j) = 0;
        end
    end
end
```

Bibliograpy

[1] Beauchamp Tower (1883) "First Report on Friction Experiments", *Proc. Inst. Mech. Engrs.*, London, pp. 632-659.

[2] O. Reynolds (1886) "On the Theory of Lubrication and its Application to Mr Beauchamp Tower's Experiments Including an Experimental Determination of the Viscosity of Olive Oil", *Phil. Trans., Roy. Soc. London*, Vol. 177 (i), pp. 157-234.

[3] Gwidon W. Stachowiak, Andrew W. Batchelor (1993) *Engineering tribology*, Elsevier-Health Sciences Division, Waltham USA.

[4] A. Cameron (1966) *Principles of Lubrication*, Longmans Green and Co. Ltd., London.

[5] O. Pinkus and B. Sternlicht (1961) *Theory of Hydrodynamic Lubrication*, McGraw-Hill, New York.

[6] Ronald L. Panton (2013) *Incompressibe Flow*, fourth ed., Hoboken: John Wiley & Sons, New Jersey, USA.

[7] R.W. Wilson (1975) "Cavitation Damage in Plain Bearings", Proc. 1st Leeds-Lyon Symp. on *Tribology, Cavitation and Related Phenomena in Lubrication*, editors, D. Dowson, C.M. Taylor and M. Godet, Inst. Mech. Engrs., London, pp. 177-184.

[8] Paulo Flores, J.C. Pimenta Claro, Jorge Ambrósio (2006) "Journal bearings subjected to dynamic loads: the analytical mobility method", on *Mecânica Experimental*, Vol 13, pp 115-127.

[9] P. Flores, H.M. Lankarani, J. Ambrósio, J.C.P. Claro (2004) "Modelling lubricated revolute joints in multibody mechanical systems" *Proceedings of the Institution of Mechanical Engineers, Part K: Journal of Multi-body Dynamics*, Vol 218(4), pp. 183-190.

[10] C. Canuto (2020) *Notes of the lecture course: numerical models and methods (mechanical engineering)*, Politecnico di Torino, Torino.

[11] A. Sommerfeld (1904) "Zur hydrodynamischen Theorie der Schmiermittelreibung", *Zeitschrift der Mathematik und Physik*, Vol. 40, pp. 97-155.

[12] A. Cameron (1981) *Basic Lubrication Theory*, Ellis Horwood Ltd., London, 1981.

[13] A.T. Prata, R.T.S.S. Ferriera, D.E.B. Mile, M.G.D. Bortoli (1988) "Dynamically Loaded Journal Bearings: Finite Volume Method Analysis". *International Compressor Engineering Conference*. Paper 599.

[14] R.F. Crouch, A. Cameron (1961) "Viscosity-Temperature Equations for Lubricants", *Journal of the Institute of Petroleum*, Vol. 47, pp. 307-313.

[15] C. Barus (1893) "Isotherms, Isopiestics and Isometrics Relative to Viscosity", *American Journal of Science*, Vol. 45, pp. 87-96.

[16] J.-P. Emond, F. Mercier, M.C.N. Nunes (1999) "In-flight temperature conditions in the holds of an widebody aircraft " *Conference: 20th International Congress of Refrigeration*, Sidney, Australia

[17] Olof Runborg (2013) *Numerical integration*, KTH, Sweden.

[18] P. Flores (2004) "Dynamic Analysis of Mechanical Systems with Imperfect Kinematic Joints", Universiade Do Minho.

[19] H. Hertz (1881) "On the contact of solids — on the contact of rigid elastic solids and on hardness (translated by D. E. Jones and G.A. Schott)", *miscellaneous papers, Macmillan and Co. Ltd.*, London, England, pp. 146–183.

[20] Jia Ma, Linfang Qian, Guangsong Chen, Miao Li (2015) "Dynamic analysis of mechanical systems with planar revolute joints with clearance" *Mechanism and Machine Theory*, Jiangsu, China.

[21] H.M. Lankarani, P.E. Nikravesh (1990) "A contact force model with hysteresis damping for impact analysis of multibody systems", *Journal of Mechanical Design*, Vol 112, pp. 369–376.

[22] Pereira C., Ramalho A., Ambrósio J. (2014) "Applicability domain of internal cylindrical contact force models", Mech. *Mach. Theory 78*, pp. 141–157.

[23] C. Pereira, A. Ramalho, J. Ambrósio (2015) "An enhanced cylindrical contact force model", *Multibody System Dynamics*, Vol 35, pp. 277-298.

[24] Carlo Ferraresi, Terenziano Raparelli (2007), *Meccanica applicata*, CLUT, Torino.

[25] D.T. Greenwood (1965) *Principles of Dynamics*, Prentice-Hall, Englewood Cliffs, New Jersey, 1965.

[26] P. Flores, J. Ambrósio, J.C.P. Claro, H.M. Lankarani, C.S. Koshy (2006) "A study on dynamics of mechanical systems including joints with clearance and lubrication", *Mechanism and Machine Theory* 4, pp. 247-261.

[27] J. Ambrósio (2002) "Impact of rigid and flexible multibody systems: deformation description and contact models", *W. Schiehlen, M.Valásek (Eds.), Proceedings of the NATO-ASI on Virtual Non-linear Multibody Systems,* vol. II, Prague, Czech Republic, pp. 15–33.

[28] T.E. Tallian (1967) "On Competing Failure Modes in Rolling Contact", *ASLE Transactions*, Vol. 10, pp. 418-439.

[29] Stefan Frischemeier (1997) "Electrohydrostatic actuators for aircraft primary flight control - types, modelling and evaluation", *5th Scandinavian International Conference on Fluid Power*, Linköping, Sweden

[30] Sylvain Autin, Jérôme Socheleau, Andrea Dellacasa, Andrea De Martin, Giovanni Jacazio, and George Vachtsevanos (2018) "Feasibility Study of a PHM System for Electro-hydraulic Servo-actuators for Primary Flight Controls", *Annual conference of the prognostics and health management society*, Philadelphia, PA, USA.

[31] Elattar Hatem M., Elminir Hamdy K.,Riad A. M. (2016) *Prognostics: a literature review*, Complex & Intelligent Systems, June, Vol. 2, Issue 2, pp. 125–154, Springer, Heidelberg, Germany

[32] Vachtsevanos George, Lewis Frank, Roemer Michael, Hess Andrew, Wu Biqing (2006) *Intelligent Fault Diagnosis and Prognosis for Engineering Systems*, John Wiley & Sons, Inc., Hoboken, New Jersey, U.S.A.

[33] Uckun S., Goebel K., Lucas P. (2008) "Standardizing research methods for prognostics", *International conference on prognostics and health management, IEEE,* Marriott Tech Center Denver, CO, pp 1–10.

[34] Stark D. (2010) *Prognostics and health management (PHM)*, Tutorial material, International Sematech Manufacturing Initiative (ISMI), July 14, Austin, T.X., U.S.A.

[35] Yan J., Koc M., Lee J. (2004) "A prognostic algorithm for machine performance assessment and its application*", Production Planning & Control*, Vol. 15, London, U.K, pp. 796-801.

[36] Voisin A., Levrat E., Cocheteux P., Iung B. (2010) "Generic prognosis model for proactive maintenance decision support: application to pre-industrial emaintenance test bed." *J Intell Manuf 21,* pp. 177–193 .

[37] Wayne Scraba (2016) "Critical components: what you need to know about rod-ends & spherical bearing ", *Grassroots motorsports.*

[38] Xuejin Shen, Pandong Gao, Zhaolei Liu, Xiaoyang Chen (2014) "Elastic Properties of the Fabric Liner and Their Influence on the Wear Depth of the Spherical Plain Bearing", *Journal of Nanomaterials.*

[39] Dominique van den Bossche (2016), "Flight control actuation system: consideration on architecture design and system installation", Presentation at Politecnico di Torino, Torino, Italy.

[40] Andrea De Martin (2014) "Fault-to-failure process of actuators mechanical components", Politecnico di Torino, Italy.

[41] Dominique van den Bossche "Servo Actuator Attachments: Roller Bearings vs PTFE lined Spherical Bearings", Presentation.

[42] AST Bearings, *Bearings Catalog: technical information*, New Jersey, USA

Ringraziamenti

In primo luogo voglio ringraziare quelle presone che garantendo una profonda esperienza professionale e completa disponibilità hanno reso possibile lo svolgimento di questa tesi in maniera autonoma, ma allo stesso tempo in totale serenità. Ringrazio quindi il Dott. Andrea De Martin e il Prof. Massimo Sorli per i loro fondamentale contributo.

Un sentito ringraziamento va ai miei genitori, Laura e Maurizio, che mi avete supportato non solo economicamente ed affettivamente, ma che avete anche partecipato in maniera attiva a superare le prime difficoltà trovate durante il mio percorso universitario e che fra tutti siete le presone che maggiormente hanno contribuito al raggiungimento di questo mio risultato.

Infine, voglio ringraziare tutti i miei amici, sia quelli conosciuti tra i banchi del Politecnico che quelli di vecchia data. In particolare, voglio fare i nomi di Federico, Andrea e Stefano con cui ho passato prima i cinque anni di superiori e successivamente tutto il periodo universitario come coinquilini. Grazie di cuore ragazzi, con voi ho condiviso esperienze che non dimenticherò mai e, indubbiamente, gli ultimi anni non sarebbero stati gli stessi se non gli avessimo passati assieme.